**Spectroscopic Studies of Physical and Electronic Structure in Transition Metal Oxide Photocatalysts**

by

Stephanie Noelle Choing

A dissertation submitted in partial satisfaction of the

requirements for the degree of

Doctor of Philosophy

in

Chemistry

in the

Graduate Division

of the

University of California, Berkeley

Committee in charge:

Professor Tanja Cuk, Chair
Professor Richard Saykally
Professor Feng Wang

Spring 2016

**Spectroscopic Studies of Physical and Electronic Structure in Transition Metal Oxide Photocatalysts**

## Abstract

Spectroscopic Studies of Physical and Electronic Structure in Transition Metal Oxide Photocatalysts

by

Stephanie Noelle Choing

Doctor of Philosophy in Chemistry

University of California, Berkeley

Professor Tanja Cuk, Chair

The complex relationship between electronic structure and physical structure in both molecular and solid state photocatalytic systems is examined. Ultrafast transient optical absorption spectroscopy and x-ray photoelectron spectroscopy are the main techniques used to investigate the underlying properties that affect the reactivity of various photocatalysts. The two respective spectroscopies are exceptionally suited to observing the ultrafast kinetics and interfacial behavior of these systems. In this dissertation, two systems are investigated—one a vanadium-based organometallic complex and the other strontium titanate, a wide band gap metal oxide semiconductor. The relaxation dynamics of a chelated oxovanadium (V) ligand-to-metal charge transfer complex are measured by ultrafast transient absorption. A combination of theoretical and experimental work indicate that the observed excited state lifetime in this molecular complex, which is an order of magnitude longer than those of metal-to-ligand charge transfer iron compounds, is derived uniquely from geometric constraints on its radiative and nonradiative relaxation pathways. Transient optical reflectance measurements are also carried out on niobium-doped strontium titanate at the solid-liquid interface to identify midgap radical states that could be implicated in the water oxidation mechanism. The creation of localized radical hole species is determined to be a surface-site limited process, which is highly dependent on the *in situ* reaction conditions. The application of voltage is shown to induce a significant redistribution of holes to the surface from valence band hole species, highlighting the capacity of the surface to accommodate localized charge under different conditions. Additional x-ray photoelectron spectroscopic measurements are taken under ambient pressure conditions to investigate water adsorption on the strontium titanate (001) surface. The effects of different variables—surface termination, dopants, and photoelectrochemical surface treatment—on the surface wetting behavior are considered. Further quantitative analysis of the x-ray photoemission data is currently underway; details of the data processing and analysis procedures as well as a description of how these sample variables might manifest in our x-ray spectra are discussed.

I would like to dedicate this dissertation to my sisters, Allison and Kelsey, from whom I am constantly learning and whom I continue to lean on for emotional and moral support.

# Contents

# List of Figures

# List of Tables

## Acknowledgments

Throughout my graduate career, I have become acutely aware of the many trials and tribulations that comprise the daily life of a scientist. I am glad not only to have made the journey through but to now call myself one who has made an honest attempt to add to the body of knowledge that we call science. Attending graduate school has been a very humbling experience, to say the least, and I could not have completed this journey without the help of many others.

I would first like to acknowledge my advisor, Professor Tanja Cuk, for granting me the opportunity to enter the world of scientific research and, in the process, to learn much more about myself as a person—in my motivation, creativity and resilience. Reflecting on the many years I have spent here, I leave graduate school with a very concrete idea of what I would like to pursue in life and the contribution I would like to make in the world. None of this would have been possible without the guidance of my advisor.

It is a rare thing to find a scientist that works without the assistance of other generous people who devote their time, resources, and efforts to that person's success. That being said, I would like to express my gratitude to all those with whom I have had the pleasure to collaborate and who have enabled me to finish my doctoral studies. I would like to thank all of my research coworkers in the Cuk Laboratory: Dr. Hoang Q. Doan, Dr. Matthias M. Waegele, Mr. Kevin L. Pollock, Dr. Amber M. Hibberd, Mr. David M. Herlihy, Mr. Xihan Chen, Mr. Jonathan H. Raberg, Dr. Daniel J. Aschaffenburg, Mr. Aayush Singh, Ms. Nhu Tran, Mr. Axel A. Ramos, and Mr. Joe Mosley. Thank you for being a wonderful family.

I would like to thank Prof. Isaac Tamblyn and Mr. Graham Clendenning at the University of Ontario Institute of Technology, Prof. Walter W. Weare and Dr. Aaron J. Francis at North Carolina State University, and Dr. Ian Sharp and Dr. Jason K. Cooper at the Joint Center for Artificial Photosynthesis (LBNL) for their input and assistance on the oxovanadium project. To Dr. David Prendergast and Dr. Chaitanya Sri Das Pemmaraju at the Molecular Foundry, thank you for your theoretical calculations and guidance regarding the strontium titanate studies. I would like to thank Dr. Hendrik Bluhm at the Advanced Light Source for all his assistance with the x-ray photoemission measurements. Broadly, I would also like to acknowledge several beamline scientists and x-ray researchers at the Advanced Light Source at Lawrence Berkeley National Laboratory, including Dr. Oliver Gessner, Dr. Stefan Neppl, Mr. Johannes Mahl, Dr. Per-Anders Glans, Dr. Jinghua Guo, Dr. Matthew Strader, Dr. Amy Cordones-Hahn, and Dr. Andreas Scholl, for providing continuous opportunities for me to work alongside them over the last six years.

I could not have completed my degree without the help of the extremely supportive community of graduate students of UC Berkeley. The truly collegiate atmosphere was, in no small part, the primary reason I chose Berkeley as my home for the better half of a decade. It was, however, certainly serendipitous that I chose to attend the University of California, Berkeley, with the particular cohort of 2010. To all my friends of the class of 2010, thank you for making the last six years an unforgettable experience. I would especially like to express my gratitude to my colleague Dr. Hoang Q. Doan, with whom I have shared many fond

memories from the beginning of our collective time here. I could not have chosen a better friend or surrogate sister than you.

To my partner Mr. Benjamin L. Cotts, whom I admire for his constant determination, integrity, curiosity and optimism: I am so indescribably grateful to have met you during graduate school. Your persistence in all aspects of life motivates me to strive towards a higher standard and, frankly, keeps me on my toes. Thank you for being my constant companion throughout this odyssey. I would also like to thank my family for all of their assistance in my pursuit of higher education. Without the love and support of my family, I would not be here today.

Of all the aspects of my graduate career, I am most grateful to have crossed paths with so many warm and generous people. Although I have not explicitly acknowledged each and every single person who has made an impact on my experience at Cal, I will not forget any of you. I only hope that, in whatever way I could, I helped to enrich your experiences here as well. Thank you.

So long, and thanks for all the fish. —*Douglas Adams*

# Chapter 1

# Introduction

Given the growth of the human population, their increasing annual consumption of energy per capita, and the obvious environmental and geopolitical costs of using traditional power sources largely derived from fossil fuels, solar energy conversion represents a major solution to the search for renewable energy sources. The sun serves as a 120,000 terawatt source of energy, substantially greater the projected global energy consumption at 15 TW for the next century. [1] However, the diffusivity and intermittence of sunlight prevent its use as a reliable energy source as delivered directly by photovoltaics. The implementation of artificial photosynthetic systems to drive the capture and conversion of solar energy into a long-term storage medium—such as batteries or chemical fuels—will be a necessary step to harnessing the full potential of the sun. Photocatalytic water splitting offers one approach to obtaining a clean source of energy, utilizing an abundant feedstock and producing non-pollutive hydrogen and oxygen gases for fuel storage, which can subsequently be combusted or recombined to release energy. [2–4]

$$2\mathrm{H_2O} \rightarrow \mathrm{O_2} + 2\mathrm{H_2} \tag{1.1}$$

$$2\mathrm{H^+} + 2e^- \rightarrow \mathrm{H_2} \tag{1.2}$$

$$2\mathrm{H_2O} \rightarrow \mathrm{O_2} + 4\mathrm{H^+} + 4e^- \tag{1.3}$$

The production of hydrogen gas from water requires two protons and the transfer of two electrons to form a single bond. The evolution of oxygen from water is kinetically a much more intensive half-reaction, necessitating two liberated oxygen atoms, four protons and a multi-step charge transfer involving four electrons. The oxidation reaction is commonly perceived as the bottleneck for water splitting, serving as the rate-limiting half-reaction. Many promising molecular and solid state materials are currently under investigation as oxygen-evolution catalysts for the oxidation half-reaction in a complete water splitting artificial photosynthetic system. For reviews of current research efforts in both hydrogen and oxygen evolution photocatalysts, the reader is referred elsewhere. [5–8]

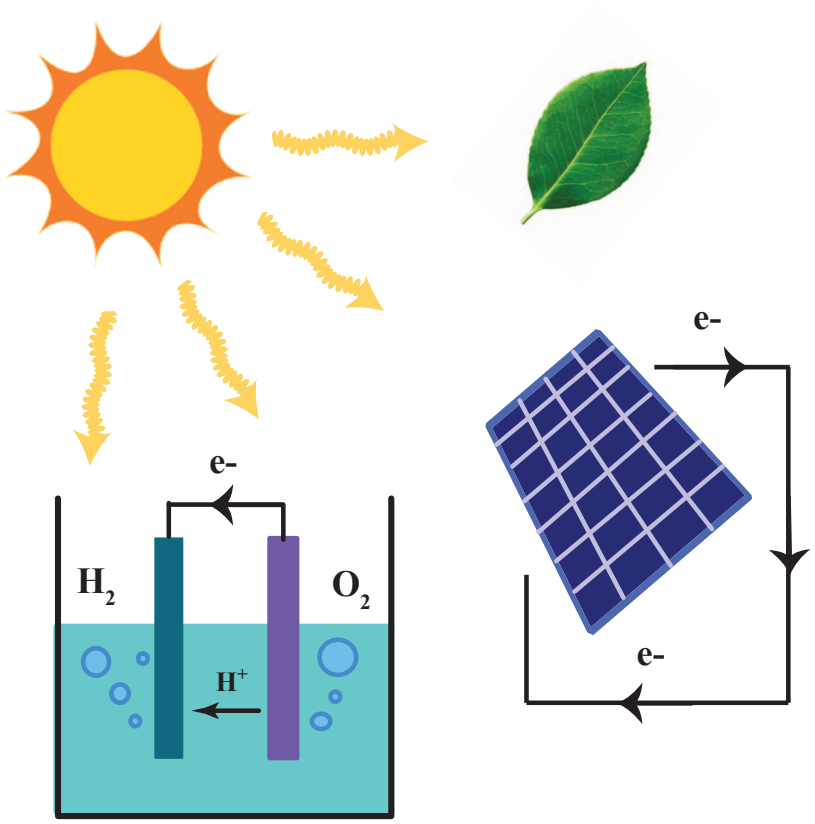


Figure 1.1: Schematic of a water splitting artificial photosynthetic system, which drives the conversion of sunlight into chemical fuels. In contrast, photovoltaics generate electricity directly from the sun.

## 1.1 Natural Photosynthesis Versus Artificial Photosynthesis

Natural photosynthesis occurring in bacteria and plants is a complex process and has been the subject of much scrutiny over the last century. In more recent decades, researchers have examined biological systems to develop a deeper understanding of the natural photosynthetic mechanism as well as a paradigm on which to model artificial scaffolds. In brief, the two major proteins involved—Light Harvesting Complex (LHC) and Oxygen-Evolving Complex (OEC)—serve the critical functions of an oxygenic photosystem. These primary functions are to (1) absorb energy as light and channel it to the appropriate active sites where it can (2) induce charge transfer and drive the catalytic production of oxygen. [9]

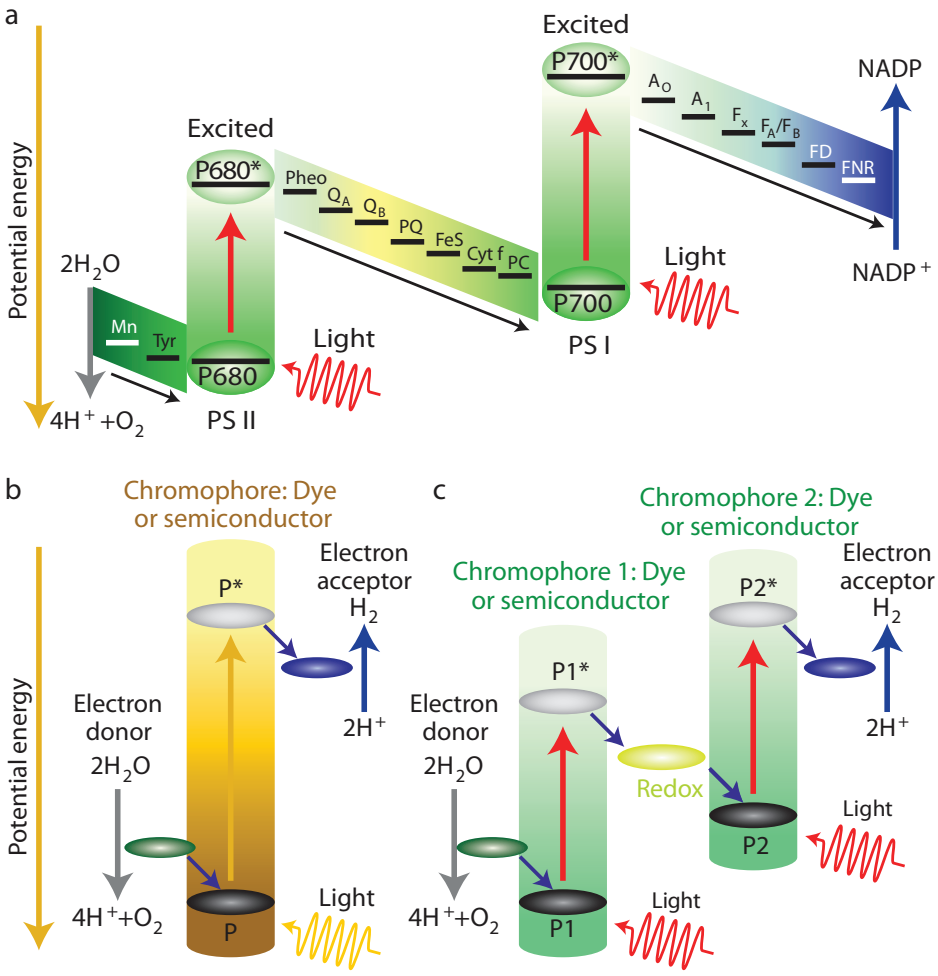


Figure 1.2: (a) The Z-scheme of electron transfer in natural photosynthetic systems with a series of redox couples is contrasted by (b) a self-contained single-component artificial system and (c) a two-component artificial photosynthetic system coupled by a single redox mediator. Reprinted by permission of Macmillan Publishers Ltd: *Nature Photonics* Tachibana, Y.; Vayssieres, L.; Durrant, J.R. "Artificial Photosynthesis for Solar Water-Splitting" Vol. 6, pp.511-518, copyright 2012.

The separation of these functions into two distinct subsets of proteins hints at the incredible importance of cooperative dynamics occurring in the electronic and structural manifolds to achieve these processes at such high quantum efficiency. For example, several studies have examined the nature of coherence and spatiotemporal correlation across the light-harvesting complex in relation to its ability to guide charge towards the reaction center. [10–13] Notably, light-harvesting complexes also mediate photoprotection in over- or under-saturating light conditions and regulate the distribution of excitation energy among photosystems. [14, 15] Given the important functions of LHC proteins, it is not surprising that the bulk of these proteins show significant homology across different biological systems. [15] Similarly, the electronic structure and local environment of the active site in the oxygen-evolution complex have been extensively probed in order to examine the mechanism by which its manganese cluster undergoes sequential charge transfers to generate oxygen gas. [16–18]

Nature has clearly evolved intricate systems to produce energy from sunlight. Conversely, the complexity of designing transition metal-based artificial photosynthetic systems lies in their structural simplicity (Fig. 1.2). In artificial systems, these functions are not so cleanly separated in space or time. The artificial system must simultaneously achieve the properties of the two individual proteins in yielding an optimal reactive center and moving the charge effectively to that site. Enzymes possess highly specialized active site cavities with secondary residues to hold substrates in highly reactive configurations. Because the size of proteins relative to a substrate such as water is massive, proteins such as PSII and LHC are more analogous to heterogeneous catalysts as a scaffold on which catalysis takes place. However, the uniquely tailored active site and its coordination to substrates are much more similar to the controlled ligand environment and interactions one would expect in a homogeneous catalytic system with molecular transition metal complexes.

Heterogeneous and homogeneous photocatalysts have neither the structural nor functional flexibility that allow biological systems to respond dynamically to their environments. [14] From this perspective, the comparison between the biological machinery of PSI and PSII—encompassing the concerted structural and electronic changes that result in highly efficient light absorption, charge transfer, and catalytic transformation—and artificial photosynthetic systems may be an inappropriate one. While there are clear analogies between natural and artificial photosynthesis, the optimization of water oxidation by both homogeneous and heterogeneous photocatalysts should be approached with a better idea of the limitations intrinsic to these photocatalysts and the structure-activity relationships that arise.

## 1.2 Physical and Electronic Structure

One major complication inhibiting our ability to devise artificial scaffolds for water splitting is our lack of knowledge regarding the exact mechanism of water oxidation in photocatalytic systems. Both the localization and relaxation dynamics of carriers within the system on an ultrafast timescale dictate the eventual formation of intermediates and preferred kinetics

on the nanosecond timescale. Therefore, it is imperative to identify the multiple pathways in which excited electrons and holes can flow following photoexcitation. The intervening period following femtosecond photoexcitation spans six orders of magnitude during which any number of electronic and vibrational processes—even electron transfer and bond formation—can occur (Fig. 1.3). Although much effort has been devoted to the development of materials that are able to harness solar energy and, thus, drive chemical reactions, very little is understood fundamentally about the structural and electronic changes that occur on the timescales between initial photon absorption and the last step of catalysis.

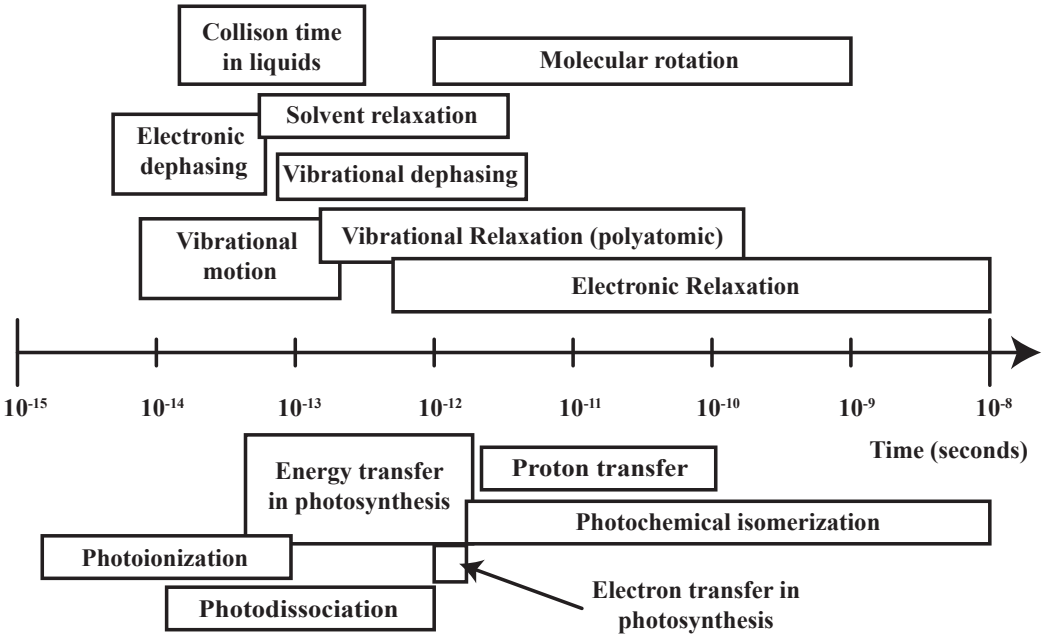


Figure 1.3: Typical timescales in chemistry and biology. Adapted from G.R. Fleming and P.G. Wolynes, *Physics Today*, 1990. [19]

A second impediment to the development of efficient solid-state oxygen evolution systems is our limited understanding of the interactions between water and the surfaces of heterogeneous catalysts. The heterogeneous catalyst surface may support several different types of adsorption interactions and, consequently, different mechanisms of water oxidation may be possible. From an energetic perspective, some wetting interactions may be more favorable than others, leading to different reactivities.

To address these issues, both ultrafast transient optical and x-ray spectroscopies are very useful techniques to investigate the behavior of these systems. With the precise resolution of early timescales and sensitivity to the interface that these measurements provide, the relationship between physical structure and electronic structure in water splitting photocatalysts can be examined. For this reason, these two techniques are employed as the principal

methods within this dissertation to study the properties of both molecular and solid-state systems.

## 1.3 Transition Metal Organometallic Complexes

Ever since the late 1800's, transition metal complexes have formed the basis of a large subset of chemistry from a theoretical and experimental standpoint regarding orbital interaction (crystal field, ligand field, molecular orbital, etc.). The utility of these complexes to drive chemical reactions catalytically has landed them a vaulted place in synthetic research laboratories as well as industrial-scale manufacturing facilities. The principal difficulty in utilizing these molecular compounds for photo-driven water oxidation lies within creating the appropriate ligand coordination environments to obtain the desired reactivity and balancing their catalytic properties with robustness and durability.

Ruthenium trisbypyridyl dichloride has been the prototypical transition metal complex for artificial photosynthetic systems since its discovery. [20] Used primarily as a sensitizer, its final photoexcited triplet state is both sufficiently long-lived and energetically high to engage in useful transformations on the nanosecond or longer timescale. However, the cost of the ruthenium and alternative precious metal centers has been a prohibitive factor in the realization of large-scale photocatalytic systems. For a feasible implementation of artificial photosynthesis, it is generally acknowledged that the systems in question must be composed of earth abundant elements, be amenable to large-scale manufacture, and provide durable, robust catalytic performance. [21, 22] Transition metal complexes are attractive candidates for use in such systems because they offer two handles with which to tune these characteristics—the ligand coordination environment and the metal center.

Unfortunately, attempts to exchange precious metals with 3d transition metals, such as iron for ruthenium, have been less than successful. Rapid relaxation down to low-lying metal-centered states seems to be a ubiquitous deactivation pathway for most first-row transition metals that plagues their catalytic performance. This behavior is exemplified by the first-row analog of ruthenium, iron, whose polypyridyl derivatives fall into the class of spin crossover complexes. [23, 24] These compounds undergo a similar spin state conversion following photoexcitation but relax to an electronic state that is very energetically similar to the ground state within hundreds of femtoseconds. [25] Consequently, these compounds are thermodynamically useless for photo-driven catalysis. Understanding the timescales for this ultrafast relaxation, the mechanisms to inhibit these deactivation pathways, and the synthetic methods to improve localization of photogenerated charges in catalytically active orbitals are currently the major impediments to progress in this the field.

## 1.4 Solid State Transition Metal Oxides

As with organometallic complexes, solid state transition metal oxides employing first-row metals are being increasingly studied as alternatives to their precious metal counterparts. Titania, $TiO_2$, and hematite, $\alpha$-$Fe_2O_3$, are two of the most common oxide materials under study for solid state photoelectrochemical systems. As a wide band gap material, with a minimum absorption energy of 3.0 eV, titanium dioxide ineffectively utilizes the solar spectrum, neglecting the most intense visible light region. Consequently, titania is often sensitized to absorb light between 400-700 nm with dyes, including ruthenium trisbipyridyls. [26, 27] However, following the discovery of its photocatalytic behavior by Fujishima and Honda in 1972, [28] the body of research on this system has become rather large and continues to grow, making it an excellent prototype for studying fundamental charge transfer processes. [29–32] In contrast, hematite has poor light harvesting properties and high working overpotential, but is still under investigation as a viable catalyst due to its abundance, chemical stability, and visible light absorption. [33–35] Silicon has also been used extensively in photovoltaic systems, [36] and now has extended to photoelectrochemical systems. Recent research efforts have focused on engineering silicon in more reactive geometries, such as nanowires, and in complete photocatalytic systems for water splitting. [37, 38]

A few of the basic issues confounding the use of molecular transition metal photocatalysts reappear in solid state systems, including rapid deactivation of excited states, sensitivity of materials to degradation, etc. However, with heterogeneous catalytic conditions, additional uncertainties arise regarding the nature of the active photocatalytic intermediates at the interface. For example, when photocatalysis occurs, it is unclear which electronic states are responsible. These active species may have different densities of states, may populate with charge carriers at different rates, and may interact with one another. Particular intermediates may exhibit higher turnover rates under different electrolytic conditions, or may operate in multiple mechanisms at the same time. The number of variables to be considered for a heterogeneous system can grow exponentially if one is not careful to limit his or her study to a subset of conditions. Conversely, the dearth of information regarding the many possible combinations of solid-liquid interfaces acts as a large barrier to improving these transition metal oxide catalysts and devising novel photocatalytic systems. Resolving the existing ambiguity of these issues in each solid state material under the appropriate time scales and reactive conditions is a critical direction for the success of solar energy fuel conversion.

## 1.5 Conclusion

In this dissertation, the complex relationship between electronic structure and physical structure in both homogeneous and heterogeneous photocatalytic systems are examined. Following this introduction, Chapter 2 describes the principles of ultrafast transient optical absorption and x-ray photoelectron spectroscopies, which are the main experimental methods used to investigate the chemical systems studied here. These two techniques are well-suited

to investigate changes in electronic structure at early timescales and identify dependencies of energetics and reactivity on local structure. Chapter 3 delves into the investigation of an oxovanadium (V) molecular complex that is strikingly different from typical transition metal complexes considered for photo-driven systems in its strong ligand-to-metal charge transfer transition and long-lived excited state. Chapter 4 explores the formation of multiple radical hole species in strontium titanate at the solid-liquid interface and their respective responses to different *in situ* conditions. Employing ambient pressure x-ray photoelectron spectroscopy, Chapter 5 investigates the wetting behavior of the (001) surface of strontium titanate and how the behavior may be affected by alterations in surface termination and the presence of dopants.

# References


(1) Lewis, N. S. Powering the Planet. *MRS Bulletin* **2007**, *32*, 808–820.

(2) Bard, A. J.; Fox, M. A. Artificial Photosynthesis: Solar Splitting of Water to Hydrogen and Oxygen. *Accounts of Chemical Research* **1995**, *28*, 141–145.

(3) Gust, D.; Moore, T. A.; Moore, A. L. Solar Fuels via Artificial Photosynthesis. *Accounts of Chemical Research* **2009**, *42*, 1890–1898.

(4) Walter, M. G.; Warren, E. L.; McKone, J. R.; Boettcher, S. W.; Mi, Q.; Santori, E. A.; Lewis, N. S. Solar Water Splitting Cells. *Chemical Reviews* **2010**, *110*, 6446–6473.

(5) Kudo, A.; Miseki, Y. Heterogeneous Photocatalyst Materials for Water Splitting. *Chemical Society Reviews* **2009**, *38*, 253–278.

(6) Maeda, K.; Domen, K. Photocatalytic Water Splitting: Recent Progress and Future Challenges. *Journal of Physical Chemistry Letters* **2010**, *1*, 2655–2661.

(7) Osterloh, F. E. Inorganic Materials as Catalysts for Photochemical Splitting of Water. *Chemistry of Materials* **2007**, *20*, 35–54.

(8) Abe, R. Recent Progress on Photocatalytic and Photoelectrochemical Water Splitting Under Visible Light Irradiation. *Journal of Photochemistry and Photobiology C: Photochemistry Reviews* **2010**, *11*, 179–209.

(9) Golbeck, J.; Est, A., *The Biophysics of Photosynthesis*; Springer: 2014; Vol. 11.

(10) Scholes, G. D. Quantum-Coherent Electronic Energy Transfer: Did Nature Think of It First? *Journal of Physical Chemistry Letters* **2010**, *1*, 2–8.

(11) Sarovar, M.; Ishizaki, A.; Fleming, G. R.; Whaley, K. B. Quantum Entanglement in Photosynthetic Light-Harvesting Complexes. *Nature Physics* **2010**, *6*, 462–467.

(12) König, C.; Neugebauer, J. Quantum Chemical Description of Absorption Properties and Excited-State Processes in Photosynthetic Systems. *ChemPhysChem* **2012**, *13*, 386–425.

(13) Iwai, M.; Yokono, M.; Nakano, A. Toward Understanding the Multiple Spatiotemporal Dynamics of Chlorophyll Fluorescence. *Plant Signaling & Behavior* **2015**, *10*, e1022014.

(14) Horton, P.; Ruban, A. Molecular Design of the Photosystem II Light-Harvesting Antenna: Photosynthesis and Photoprotection. *Journal of Experimental Botany* **2005**, *56*, 365–373.

(15) Büchel, C. Evolution and Function of Light Harvesting Proteins. *Journal of Plant Physiology* **2015**, *172*, 62–75.

(16) McEvoy, J. P.; Brudvig, G. W. Water-Splitting Chemistry of Photosystem II. *Chemical Reviews* **2006**, *106*, 4455–4483.

(17) Renger, G.; Renger, T. Photosystem II: The Machinery of Photosynthetic Water Splitting. *Photosynthesis Research* **2008**, *98*, 53–80.

(18) Vinyard, D. J.; Ananyev, G. M.; Charles Dismukes, G. Photosystem II: The Reaction Center of Oxygenic Photosynthesis. *Annual Review of Biochemistry* **2013**, *82*, 577–606.

(19) Fleming, G. R.; Wolynes, P. G. Chemical Dynamics in Solution. *Physics Today* **1990**, *43*, 36–43.

(20) McCusker, J. K. Femtosecond Absorption Spectroscopy of Transition Metal Charge-Transfer Complexes. *Accounts of Chemical Research* **2003**, *36*, 876–887.

(21) Tachibana, Y.; Vayssieres, L.; Durrant, J. R. Artificial Photosynthesis for Solar Water-Splitting. *Nature Photonics* **2012**, *6*, 511–518.

(22) Barber, J.; Tran, P. D. From Natural to Artificial Photosynthesis. *Journal of the Royal Society Interface* **2013**, *10*, 20120984.

(23) Bressler, C.; Milne, C.; Pham, V.-T.; ElNahhas, A.; Van der Veen, R.; Gawelda, W.; Johnson, S.; Beaud, P.; Grolimund, D.; Kaiser, M., et al. Femtosecond XANES Study of the Light-Induced Spin Crossover Dynamics in an Iron (II) Complex. *Science* **2009**, *323*, 489–492.

(24) Gütlich, P.; Hauser, A. Thermal and Light-Induced Spin Crossover in Iron (II) Complexes. *Coordination Chemistry Reviews* **1990**, *97*, 1–22.

(25) Monat, J. E.; McCusker, J. K. Femtosecond Excited-State Dynamics of an Iron (II) Polypyridyl Solar Cell Sensitizer Model. *Journal of the American Chemical Society* **2000**, *122*, 4092–4097.

(26) Grätzel, M. Solar Energy Conversion by Dye-Sensitized Photovoltaic Cells. *Inorganic Chemistry* **2005**, *44*, 6841–6851.

(27) Youngblood, W. J.; Lee, S.-H. A.; Maeda, K.; Mallouk, T. E. Visible Light Water Splitting Using Dye-Sensitized Oxide Semiconductors. *Accounts of Chemical Research* **2009**, *42*, 1966–1973.

(28) Fujishima, A.; Honda, K. Photolysis-Decomposition of Water at the Surface of an Irradiated Semiconductor. *Nature* **1972**, *238*, 37–38.

(29) Fujishima, A.; Rao, T. N.; Tryk, D. A. Titanium Dioxide Photocatalysis. *Journal of Photochemistry and Photobiology C: Photochemistry Reviews* **2000**, *1*, 1–21.

(30) Ni, M.; Leung, M. K.; Leung, D. Y.; Sumathy, K. A Review and Recent Developments in Photocatalytic Water-Splitting Using $TiO_2$ for Hydrogen Production. *Renewable and Sustainable Energy Reviews* **2007**, *11*, 401–425.

(31) Gaya, U. I.; Abdullah, A. H. Heterogeneous Photocatalytic Degradation of Organic Contaminants over Titanium Dioxide: A Review of Fundamentals, Progress and Problems. *Journal of Photochemistry and Photobiology C: Photochemistry Reviews* **2008**, *9*, 1–12.

(32) Pelaez, M.; Nolan, N. T.; Pillai, S. C.; Seery, M. K.; Falaras, P.; Kontos, A. G.; Dunlop, P. S.; Hamilton, J. W.; Byrne, J. A.; O'shea, K., et al. A Review on the Visible Light Active Titanium Dioxide Photocatalysts for Environmental Applications. *Applied Catalysis B: Environmental* **2012**, *125*, 331–349.

(33) Sivula, K.; Le Formal, F.; Grätzel, M. Solar Water Splitting: Progress Using Hematite ($\alpha$-$Fe_2O_3$) Photoelectrodes. *ChemSusChem* **2011**, *4*, 432–449.

(34) Tilley, S. D.; Cornuz, M.; Sivula, K.; Grätzel, M. Light-Induced Water Splitting with Hematite: Improved Nanostructure and Iridium Oxide Catalysis. *Angewandte Chemie* **2010**, *122*, 6549–6552.

(35) Bora, D. K.; Braun, A.; Constable, E. C. "In Rust We Trust". Hematite–The Prospective Inorganic Backbone for Artificial Photosynthesis. *Energy & Environmental Science* **2013**, *6*, 407–425.

(36) Shockley, W.; Queisser, H. J. Detailed Balance Limit of Efficiency of p-n Junction Solar Cells. *Journal of Applied Physics* **1961**, *32*, 510–519.

(37) Liu, D.; Li, L.; Gao, Y.; Wang, C.; Jiang, J.; Xiong, Y. The Nature of Photocatalytic "Water Splitting" on Silicon Nanowires. *Angewandte Chemie International Edition* **2015**, *54*, 2980–2985.

(38) Nocera, D. G. The Artificial Leaf. *Accounts of Chemical Research* **2012**, *45*, 767–776.

# Chapter 2

# Experimental Methods & Techniques

The electronic structure and physical nature of molecular and solid state metal oxide systems are examined using two principal techniques—ultrafast transient optical absorption and ambient pressure x-ray photoelectron spectroscopy. These spectroscopies are ideal for investigating the very early time dynamics of both homogeneous and heterogeneous photocatalysts and the interfacial structure-activity relationships of solid-state systems, respectively. In this chapter, the basic principles—theoretical background and practical aspects—of transient absorption spectroscopy and x-ray photoelectron spectroscopy are discussed. Specific information regarding each chemical system under investigation will be included in the relevant chapters.

## 2.1 Transient Absorption Measurements

### 2.1.1 Basic Principles

Once limited to home-built setups, ultrafast transient absorption spectroscopy has established itself as an invaluable technique over the last three decades. As transient absorption systems have become commercially available and relatively straightforward to operate, they have continued to provide insight into a wide variety of chemical systems. [1–3] In transient absorption, or pump-probe, spectroscopy, a sample of interest is subjected to two sequential light pulses with a variable time delay between them, as shown in Figs. 2.1 and 2.2a. The first light pulse resonantly excites the molecule or solid state material at a chosen transition. The second weaker monochromatic or broadband probe pulse interrogates the evolution of the excited state by monitoring changes in probe transmission or reflection as a function of the time delay between the two pulses. The differential absorption or reflection of the probe pulse with respect to the ground state response (i.e., laser-on vs. laser-off) provides a snapshot of the excited state as it evolves in time.

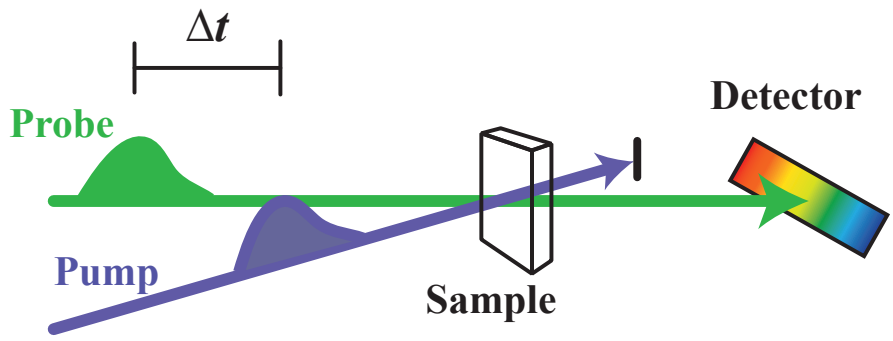


Figure 2.1: Schematic of a typical transient absorption experiment in transmission mode.

### 2.1.2 Interpreting Transient Absorption Measurements

Transient absorption measurements are typically recorded in transmission mode, with both pump and probe pulses directed through a sample of millimeter thickness. For any given time delay, the transmitted probe light is recorded with and without the pump pulse present, corresponding to the laser-on ($I_{on}$) and laser-off ($I_{off}$) signals. The differential absorption signal is recorded as a change in absorbance $\Delta A(t)$ in units of optical density (OD).

$$\Delta A = -log(\frac{I_{on}}{I_{off}}) \tag{2.1}$$

The static absorbance is described by the Beer-Lambert equation:

$$A(\lambda) = \epsilon(\lambda)cl, \tag{2.2}$$

where $\epsilon$ represents the molar absorptivity (extinction coefficient) of a molecule or material at a given wavelength $\lambda$, $c$ is the concentration of the absorbing species within the probe volume and $l$ is the sample pathlength through which the probe light travels. In a time-resolved set-up, the differential absorption examines changes in the excited state absorption spectrum relative to the ground state absorption. The differential absorption will depend not only on the wavelength probed, as with the static absorption, but also on the time delay $t$ with respect to the excitation (pump) pulse. Data can be collected as a function of wavelength—resulting in a transient spectrum at time $t$—or as a function of time—producing one or more kinetic traces that track the dynamics at particular wavelengths.

$$\Delta A(\lambda, t) = \sum_k \Delta\big(\epsilon_k(\lambda)c_k(t)l\big) \tag{2.3}$$

The change in the absorption due to the excitation pulse may manifest as a difference in the absorptivity, $\Delta\epsilon$, of the species in question and/or its time-dependent concentration, $\Delta c$. Multiple species or electronic states may coexist within a sample at a given time, therefore,

the transient response of a system is characterized by the sum of the transient responses of all its components. When several components have overlapping contributions to the transient response, the interpretation of the transient response can become incredibly complex. The reader is referred to Appendix A in which the analysis of multiwavelength data is addressed. [2–4]

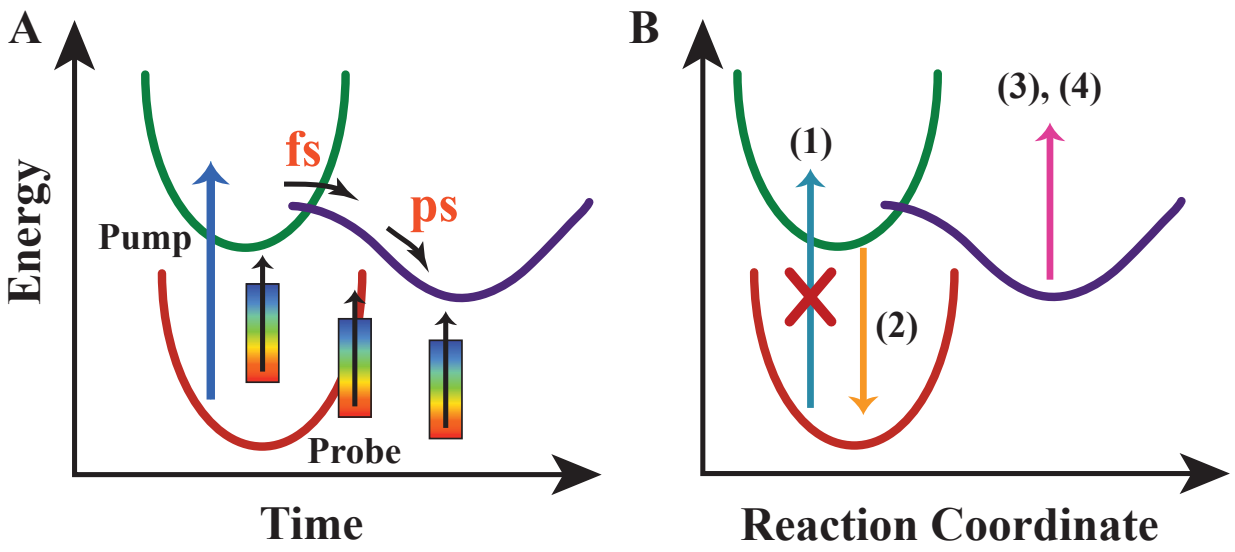


Figure 2.2: (a) Following excitation of the ground state system by the pump pulse, probe pulses at variable time delay track the evolution of the excited state(s) by changes in their absorption spectrum. (b) The four major transitions in pump-probe spectroscopy are illustrated: (1) ground-state bleach, (2) stimulated emission, (3) excited state and (4) product absorption.

Changes in the excited state absorption spectrum are usually classified into four main types of transitions, as shown in Fig. 2.2b. In a transient absorption experiment, a small fraction of molecules (or charge carriers) is excited by the pump pulse. The probe is kept at a significantly lower fluence than the pump pulse (typically less than 10 %) so as to minimize the perturbation of the excited state population. Because there are fewer molecules (carriers) in the ground state, the overall ground-state absorption of light will be reduced. This will result in a negative change in absorption (-$\Delta$A), i.e. greater transmission of probe light to the detector, known as a ground-state bleach (GSB). Molecules (carriers) in the excited state may also undergo stimulated emission (SE) in the presence of the probe pulse. In such a case, the presence of the probe photon induces the excited molecule or carrier to transition back to its ground state and release a photon of the same wavelength and in the same direction as the probe. Stimulated emission—which will only occur for an optically allowed transition and whose spectral profile will match the fluorescence spectrum of the excited

molecule (carrier), including its Stokes shift—also appears as an increase in transmission and is characterized by a negative absorption change (-$\Delta$A). Alternatively, the excited state produced by the pump pulse may have its own allowed transition dipole moments that couple to higher-lying states at certain wavelengths. Thus, when the excited state is illuminated by the probe, the excited state absorbs photons at those wavelengths. The overall intensity of light reaching the detector will decrease and present as a positive change in absorbance (+$\Delta$A). In very complex systems, the excited state may undergo charge transfer or even bond rearrangement that alter it to the point where it is distinct from the original excited state. This distinctive species can be considered a photogenerated product, with its own transition dipole moments to higher-lying states. The resulting response is similar to an excited state absorption—appearing as an decrease in probe intensity and a positive change in absorption (+$\Delta$A)—but is occasionally cited in the literature as a product absorption. The distinction between the excited state absorption and the product absorption is poorly delineated in practice unless the excited state system has been well-characterized by other means.

### 2.1.3 Equipment and Experimental Setup

As transient absorption spectroscopy has become a widespread technique, an overwhelming variety of ultrafast transient experimental setups have been devised to conduct such measurements. For the sake of brevity, only the experimental set-up employed for the experiments conducted in this dissertation (Fig. 2.3) is discussed.

A single laser pulse is derived initially from a Ti:sapphire regenerative amplifier laser with a fundamental wavelength of 800 nm (1.55 eV), 10 nm full-width half-maximum, and a pulse length of 150 fs, generated at a repetition rate of 1 kHz. The original pulse is separated into two beams—the pump and the probe—through the use of a beamsplitter. As mentioned earlier, the probe pulse is maintained at a substantially weaker intensity (mJ/cm$^2$) than the pump pulse for data acquisition; the ratio of the split is chosen to reflect this requirement. In certain cases, the fundamental laser pulse may not be at the appropriate photon energy for use as either the pump or probe, or both. To achieve the desired wavelength(s), the two light pulses may be sent to separate wavelength conversion stages. As shown in Fig. 2.3, the pump pulse is converted to the appropriate excitation wavelengths through nonlinear processes in an optical parametric amplifier (OPA) (OPerA Solo, Coherent, Inc., Santa Clara, CA) or through a third harmonic generation stage. For further detail on nonlinear conversion methods, the reader is referred to a number of other comprehensive sources. [5–7] Although the probe pulse can also be converted to the appropriate wavelengths through similar nonlinear processes, the high peak power (GW/cm$^2$) requirements for nonlinear processes often (but do not always) preclude their use with lower power probe pulses. Here, a typical configuration is employed in which a white light continuum is generated by focusing a small fraction of the fundamental pulse into a sapphire or calcium fluoride plate. [8]

Following conversion to the desired wavelengths, both beams are routed to the sample. Through careful control of the distances traveled by the light pulses, the pump and probe

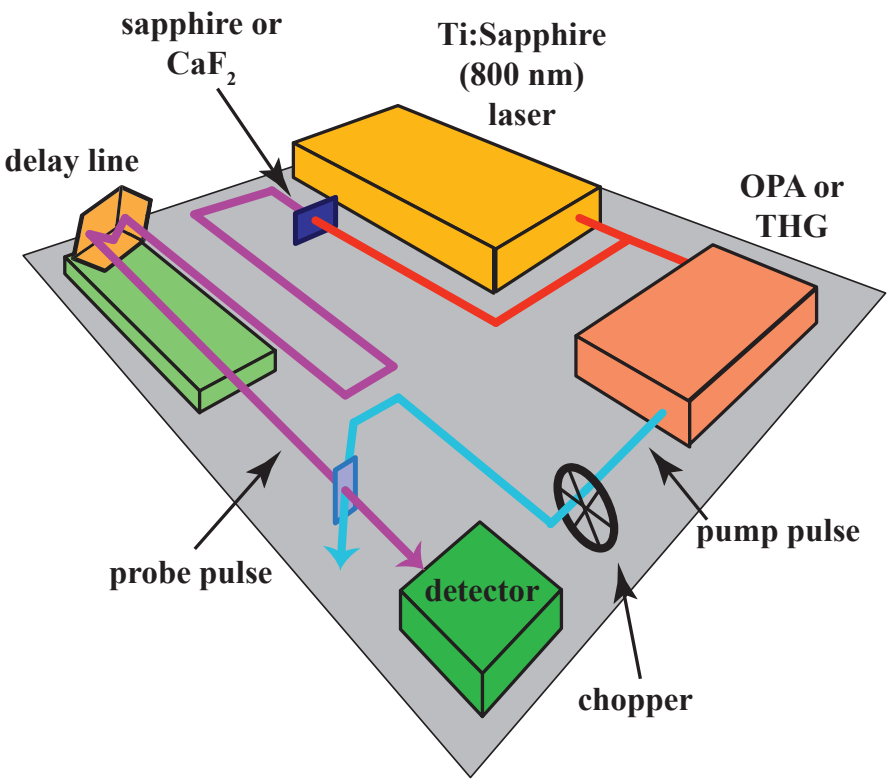


Figure 2.3: Generalized laser table set-up for a transient absorption experiment in transmission mode. Mirrors and lenses are omitted for clarity.

will reach the sample at nearly the same time. Gross temporal overlap is necessary to ensure that the probe pulse will reach the sample close enough in time to the initial excitation by the pump such that the subsequent dynamics of the excited state can be monitored. Fine control of the relative arrival times between the pump and probe pulses is achieved with a mechanical delay stage. The precise position of the delay stage and, consequently, the distance traveled by the probe are monitored during data acquisition to determine the time delay $\Delta t$ between the two pulses. When both light pulses reach the sample, their spot sizes are adjusted with focusing lenses or curved mirrors to control the concentration of excited species within the sample and to ensure spatial overlap of the pump with the probe. Spatial overlap is a necessary constraint of the experiment that ensures the probe pulse tracks the excited state population rather than a region of the sample that was not illuminated by the pump. Generally, the spot sizes are maintained at a 2:1 ratio, with the pump the larger of the two. After both pulses have traveled through the sample, the probe pulse is spatially separated from the pump and detected on a light sensitive diode or CCD array. The probe signal collected on the detector is synchronized with a mechanical chopper wheel, which

modulates the pump pulse to determine the differential laser-on/laser-off signal.

The device employed for detection will invariably depend on the wavelength(s) chosen as the probe. The detector is usually comprised of a single photodiode into which monochromatized light is focused for individual wavelength measurements or, alternatively, composed of several light-sensitive elements in an array for simultaneous broadband spectral acquisition in which each pixel corresponds to a certain wavelength. Impinging light usually generates photocurrent or -voltage that is sent to and read by a computer. The sensitivity and responsiveness of the detector can vary widely across the probe spectrum and so the photosensitive material is chosen with great care to accommodate the desired probe wavelength(s). The signal is recorded in relation to a number of factors, primarily the location of the delay stage—that is, probe pulse arrival with respect to the pump pulse arrival. Additional variables include the probe wavelength as well as the phase of the signal with respect to the laser-off measurement—indicating either a positive or negative change in absorption in the presence of the pump.

Although the time delay is regulated by the incremental steps taken by the mechanical delay stage, the absolute temporal resolution conferred by this technique depends intimately on the duration of the interrogating pump and probe pulses. The convolution of these two pulses provides the instrument response function (IRF), which limits our ability to measure transient lifetimes at very short timescales. The length of the probe pulse is also relevant in relation to the time delay increments selected for data acquisition. In the setup described above, the pump and probe pulses are estimated to be on the order of 150 fs in duration, with some additional dispersion to account for material traversed in the wavelength conversion stages. As a result, changes in the transient response on the order of 100 fs or less cannot accurately be recorded. It is important to note that the limitation of the resolution is often dictated by the monochromatic pump pulse, which in turn is usually limited by the original bandwidth of the fundamental 800 nm pulse. However, advances in optical laser spectroscopy have afforded increasingly short duration pump pulses with broadband spectral windows that have been essential in elucidating chemical dynamics at the ultrafast timescale. [6, 9, 10] In such cases, the selectivity of monochromatic light used to excite the system is traded for the ability to resolve subpicosecond behavior (on the order of 10 fs). Chemical reactions typically occur on a nanosecond timescale, though relaxation of photoexcited carriers and the generation of principal intermediates have been shown to take place at much earlier timescales. Thus, the time resolution conferred by ultrafast transient absorption spectroscopy can provide critical insight into the initial subpicosecond preparation of photoexcited states and their subsequent relaxation into active water oxidation species.

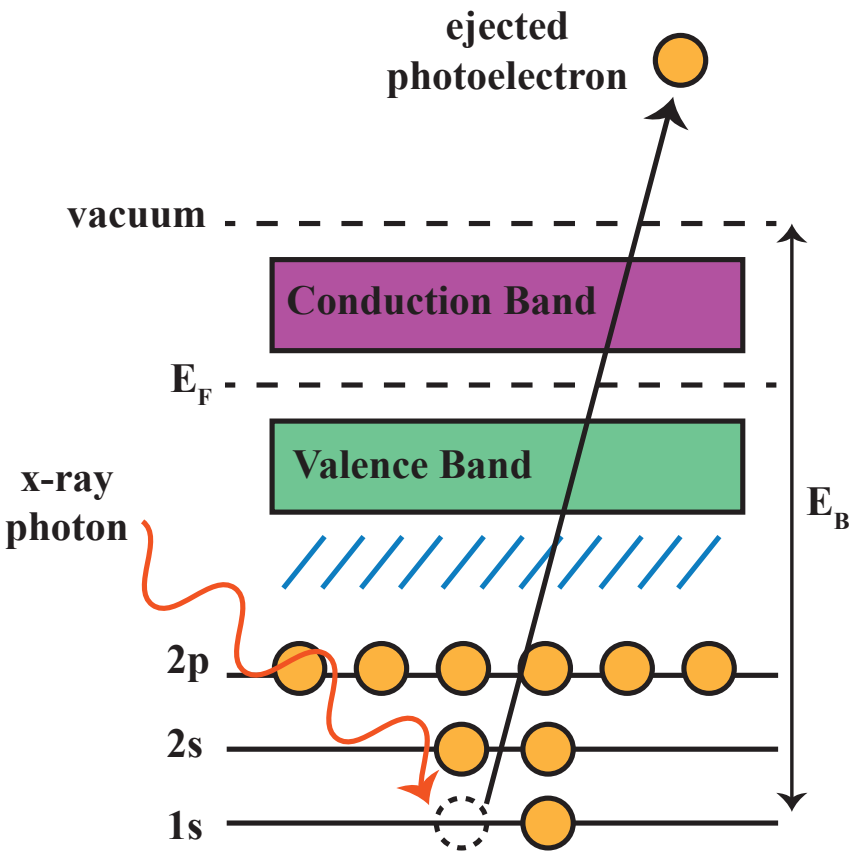


Figure 2.4: X-ray photoelectron spectroscopy tracks the excitation of a core-level electron into the vacuum continuum. The energy required to remove an electron can be modeled as the sum of the binding energy, the work function of the sample, work function of the detector, and the excess kinetic energy of the expelled electron.

## 2.2 Ambient Pressure X-Ray Photoelectron Spectroscopy (APXPS)

### 2.2.1 Basic Principles

X-ray photoemission, or photoelectron, spectroscopy is an element-specific characterization method that provides surface-sensitive information regarding the electronic structure of a sample. The principle behind this technique is the photoelectric effect, with an extension to higher-energy incident photons. [11] Electrons in a material are ejected from a material when excited with light above a threshold photon energy. The required photon energy is dictated by the tendency of the material to hold onto those electrons. In a discrete atom, the

minimum photon energy is dictated by the ionization energy for the occupied atomic orbital. The corresponding energy in a solid state system is the binding energy; when valence band electrons are the photoelectrons of interest, the binding energy is the work function $\Phi$ of the material. Once the energetic threshold is achieved or surpassed, excess energy from the photon will be converted into the kinetic energy of the ejected photoelectron. Through the law of the conservation of energy, the relationship between the incident photon energy, the binding energy and the resultant photoelectron kinetic energy is described by the following equation:

$$E_B = h\nu - E_{KE} \tag{2.4}$$

Photoelectron spectroscopy is intrinsically a surface-sensitive technique. Within a material, the inelastic mean free path (escape depth) of an electron is on the order of 5-10 Å, [12] which encompasses only a few unit cells. Therefore, electrons that escape the material to reach the detector will only come from the topmost layers of the material. Additional surface sensitivity can be obtained through adjusting the x-ray angle of incidence in order to change its penetration depth. [13] While x-ray photoelectron spectroscopy provides valuable information on material surface properties under ultrahigh vacuum conditions, the need to observe the electronic structure of interfaces in working systems or under near *in situ* conditions has resulted in an increase in ambient pressure x-ray photoemission measurements over the last two decades. [14–17]

### 2.2.2 Chemical Shifts in Binding Energy

Measurements are taken by recording the quantity of photoelectrons emitted by a material as a function of their kinetic energy. For a fixed photon energy, the binding energy of each electron can be calculated from its corresponding kinetic energy. (In practice, additional energy is lost upon absorption by the detector ($\Phi_{\text{det}}$), reducing the apparent kinetic energy.) The binding energy of an electron can then provide information regarding the local chemical environment from which it was removed. [18] Although ultraviolet light may be used for photoemission experiments to probe valence band electrons in solid state materials, the use of x-ray light to excite electrons confers elemental specificity to this technique. The energies of x-ray photons are such that core-level electrons may be excited into the continuum of vacuum states. The energy required to remove a core-level electron is strongly influenced by the effective nuclear charge of the source atom, the orbital involved ($n$ = 1, 2, 3, ...; $\ell$ = 0, 1, 2, ...), and the surrounding chemical environment through its valence electrons—listed here in decreasing order of importance. While the effective nuclear charge largely dictates the energetic region in which this emission threshold falls, the exact binding energy is controlled by several other factors including atomic oxidation state, electronegativity of neighboring atoms, bond order, and covalency. [19, 20] Any alteration in electron density around the target atom will result in a shift in binding energy. Therefore, a photoelectron spectrum and its chemical shifts can be used to identify both the electronic interactions and the structural

aspects of the material. [18, 21] The advantage of elemental specificity provided by x-rays enables the measurement of local characteristics of atoms that may be relatively dilute for a given sample. Whereas ultraviolet light can be used to eject valence band photoelectrons that are collectively shared across a number of atoms, x-ray light can narrow the focus to electrons ejected at a well-defined, discrete transition and examine the atoms of a single element type.

### 2.2.3 X-Ray Light Source

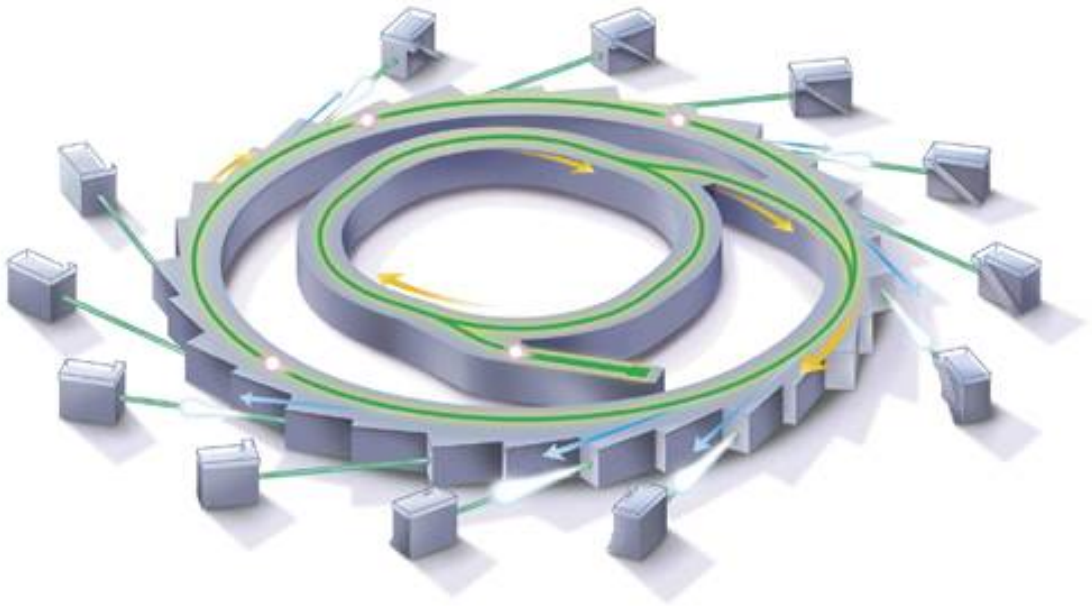

Figure 2.5: Layout of a third-generation synchrotron light source, specifically an illustration of the Australian synchrotron.

Since the 1970s, ambient pressure x-ray photoelectron measurements have been conducted at synchrotron facilities. [11, 18, 19, 22] Only recently have laboratory-scale instruments been able to provide focused x-ray beams with sufficient light intensity to enable APXPS measurements. [16] While laboratory-scale x-ray sources offer greater accessibility and lower operational costs to using a synchrotron facility, synchrotron radiation provides more flexibility in x-ray photon energies produced—comprising the full range of both soft (<1 keV) and hard x-ray (>1 keV) regimes, higher photon fluxes for better signal, and fine control of x-ray light characteristics, such as polarization.

In commercial x-ray systems used for x-ray diffraction or x-ray photoelectron measurements, x-ray light is obtained by focusing high-energy electrons onto a metal target. The incident electrons displace and eject inner-shell electrons into the vacuum. Higher-lying

electrons subsequently relax into the core orbitals to replace the ejected electrons and emit x-ray photons during the downward transition. The energy of the emitted x-ray photons is dictated by the orbital energies of the target element, often aluminum or copper, and as a result the generated light is fairly monochromatic. This is known as the characteristic emission of the material—for example, Al $K_\alpha$ and Cu $K_\alpha$. [23]

Synchrotron radiation is produced when electrons are accelerated at relativistic speeds in a curved trajectory, as seen in Fig. 2.5. Electrons are accelerated in a ring through the use of magnets. As these electrons are accelerated, they will emit energy in the form of electromagnetic radiation. The frequency of light is dictated by the angle of acceleration, which in turn is controlled by the strength of the magnet. [23] At relativistic speeds, the emitted radiation will fall within the regime of x-rays. Electrons are brought up to relativistic speeds through several stages of acceleration. Electrons are initially generated through a cathode ray tube in large quantities. These electrons are passed through a preliminary stage of acceleration, through what is known as a booster ring, shown as the inner stage in Fig. 2.5. The accelerated electrons are then trickled into the (outer) accelerator ring, in which they can achieve currents up to 500 mA. When electrons are accelerated along the curve, radiation is emitted along the tangent of the curve. This radiation continues to propagate in a straight direction, where for the purposes of experimentation, the light will be focused, monochromatized, and redirected onto a beamline endstation.

### 2.2.4 Detection Methods and Ambient Pressure Measurements

X-ray photoelectron spectroscopic measurements require direct detection of the ejected photoelectron from the core orbital. The kinetic energies of ejected electrons can be resolved by a number of analyzer types, [21] only one of which—the hemispherical electron analyzer (Fig. 2.6)—is described here. The hemispherical analyzer is comprised of two concentric half circle plates. As electrons travel between these two plates, a retarding potential is applied to both plates to allow electrons only of certain kinetic energies to reach the electron detector. The electron detector used is typically a generic electron multiplier. Alternatively, multichannel electron multipliers may be used to collect electrons with a broad range of kinetic energies simultaneously. [21]

At a minimum, the vacuum requirement for the electron analyzer has an upper limit of $10^{-5}$ Torr and for the target chamber $10^{-2}$. [21] Typical x-ray photoemission measurements are conducted under vacuum—ultrahigh vacuum ($10^{-7}$-$10^{-10}$ Torr) in synchrotron-based measurements. Both the sample chamber and analyzer are maintained at vacuum in order to reduce surface contamination as well as to ensure that ejected electrons will not scatter off residual gas molecules prior to reaching the electron detector. A standard ultrahigh vacuum XPS chamber may have a single pump to enable the transition from the sample chamber to the high vacuum environment of the analyzer. In contrast, a series of differential pumping chambers leading to the hemispherical analyzer are required for ambient pressure measurements. These pumping stages are needed to limit the scattering of photoelectrons by gas molecules. Because the chamber environment is filled with vapor in ambient pressure

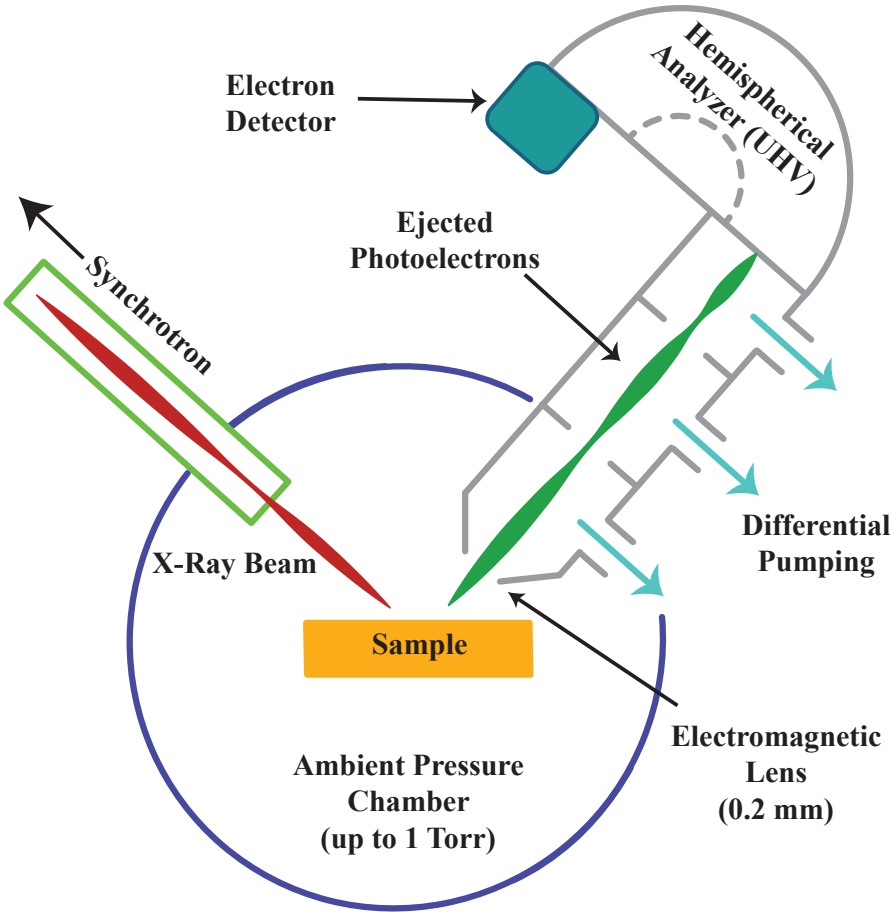


Figure 2.6: Depiction of experimental set-up for the detection of ejected photoelectrons in ambient pressure XPS. The setup for UHV XPS measurements is identical.

experiments, the different stages allow electrons to travel from a relatively high pressure environment (up to 1 Torr) to an ultrahigh vacuum environment ($10^{-10}$ Torr) through an open detector arm over a very short distance. [14, 17] For ambient pressure measurements, the experimental chamber is isolated from the x-ray source—i.e., the synchrotron—by a silicon nitride window that will transmit x-ray light but can also withstand the large pressure differential of the synchrotron and the sample chamber.

Additional efforts to minimize the diffusion of gas molecules into the detector arm involve using a very small aperture through which the electrons must travel and maintaining a very short distance between the emitting sample and this aperture—approximately 4× the aperture diameter (Fig. 2.6). When photoelectrons are emitted by a sample, the angle of their trajectory is not always along the axis of the detector arm. This behavior is used to great effect in angle-resolved photoemission measurements [24]—an instance where a multichannel

electron multiplier is utilized. Resolution of the emission angle requires a large aperture to collect electrons with different trajectories. However, in cases where the information provided by angle resolution is not needed, photoelectrons are simply focused into the hemispherical analyzer using an electromagnetic lens at the tip of the collection arm in order to provide larger signal intensity.

# References


(1) Zewail, A. H. Laser Femtochemistry. *Science* **1988**, *242*, 1645–1653.

(2) Berera, R.; van Grondelle, R.; Kennis, J. T. Ultrafast Transient Absorption Spectroscopy: Principles and Application to Photosynthetic Systems. *Photosynthesis Research* **2009**, *101*, 105–118.

(3) Ruckebusch, C.; Sliwa, M.; Pernot, P.; De Juan, A.; Tauler, R. Comprehensive Data Analysis of Femtosecond Transient Absorption Spectra: A Review. *Journal of Photochemistry and Photobiology C: Photochemistry Reviews* **2012**, *13*, 1–27.

(4) Van Stokkum, I. H.; Larsen, D. S.; van Grondelle, R. Global and Target Analysis of Time-Resolved Spectra. *Biochimica Biophysica Acta* **2004**, *1657*, 82–104.

(5) Boyd, R. W., *Nonlinear Optics*; Academic Press: 2003.

(6) Cerullo, G.; De Silvestri, S. Ultrafast Optical Parametric Amplifiers. *Review of Scientific Instruments* **2003**, *74*, 1–18.

(7) Riedle, E.; Beutter, M.; Lochbrunner, S.; Piel, J.; Schenkl, S.; Spörlein, S.; Zinth, W. Generation of 10 to 50 fs Pulses Tunable Through All of the Visible and the NIR. *Applied Physics B* **2000**, *71*, 457–465.

(8) Johnson, P. J.; Prokhorenko, V. I.; Miller, R. D. Stable UV to IR Supercontinuum Generation in Calcium Fluoride with Conserved Circular Polarization States. *Optics Express* **2009**, *17*, 21488–21496.

(9) Lochbrunner, S.; Wilhelm, T.; Piel, J.; Spörlein, S.; Riedle, E. In *Advanced Solid State Lasers*, 1999, pp 366–371.

(10) Huber, R.; Satzger, H.; Zinth, W.; Wachtveitl, J. Noncollinear Optical Parametric Amplifiers with Output Parameters Improved by the Application of a White Light Continuum Generated in $CaF_2$. *Optics Communications* **2001**, *194*, 443–448.

(11) Hollander, J. M.; Jolly, W. L. X-ray Photoelectron Spectroscopy. *Accounts of Chemical Research* **1970**, *3*, 193–200.

(12) Seah, M. P.; Dench, W. A. Quantitative Electron Spectroscopy of Surfaces: A Standard Data Base for Electron Inelastic Mean Free Paths in Solids. *Surface and Interface Analysis* **1979**, *1*, 2–11.

(13) Chester, M.; Jach, T. GRazing-Incidence X-Ray Photoelectron Spectroscopy from Multilayer Media: Oxidized GaAs (100) as a Case Study. *Physical Review B* **1993**, *48*, 17262.

(14) Salmeron, M.; Schlögl, R. Ambient Pressure Photoelectron Spectroscopy: A New Tool for Surface Science and Nanotechnology. *Surface Science Reports* **2008**, *63*, 169–199.

(15) Zhang, C.; Grass, M. E.; McDaniel, A. H.; DeCaluwe, S. C.; El Gabaly, F.; Liu, Z.; McCarty, K. F.; Farrow, R. L.; Linne, M. A.; Hussain, Z., et al. Measuring Fundamental Properties in Operating Solid Oxide Electrochemical Cells by Using in situ X-Ray Photoelectron Spectroscopy. *Nature Materials* **2010**, *9*, 944–949.

(16) Starr, D.; Liu, Z.; Hävecker, M.; Knop-Gericke, A.; Bluhm, H. Investigation of Solid-Vapor Interfaces Using Ambient Pressure X-Ray Photoelectron Spectroscopy. *Chemical Society Reviews* **2013**, *42*, 5833–5857.

(17) Stoerzinger, K. A.; Hong, W. T.; Crumlin, E. J.; Bluhm, H.; Shao-Horn, Y. Insights into Electrochemical Reactions from Ambient Pressure Photoelectron Spectroscopy. *Accounts of Chemical Research* **2015**, *48*, 2976–2983.

(18) Siegbahn, H. Electron Spectroscopy for Chemical Analysis of Liquids and Solutions. *Journal of Physical Chemistry* **1985**, *89*, 897–909.

(19) Swartz Jr, W. E. X-ray Photoelectron Spectroscopy. *Analytical Chemistry* **1973**, *45*, 788A–800a.

(20) Gelius, U. Binding Energies and Chemical Shifts in ESCA. *Physica Scripta* **1974**, *9*, 133.

(21) Hollas, J. M., *Modern Spectroscopy*; John Wiley & Sons: 2004.

(22) Fadley, C. S. Angle-resolved X-ray Photoelectron Spectroscopy. *Progress in Surface Science* **1984**, *16*, 275–388.

(23) Thompson, A.; Vaughan, D.; Center for X-ray Optics; Advanced Light Source, *X-Ray Data Booklet*; Lawrence Berkeley National Laboratory: 2009.

(24) Damascelli, A. Probing the electronic structure of complex systems by ARPES. *Physica Scripta* **2004**, *T109*, 61–74.

# Chapter 3

# Distortionally Inhibited Excited State of an Oxovanadium (V) Complex $VOL^F$

*Adapted with permission from Choing et al., "Long-lived LMCT in a $d^0$ Vanadium (V) Complex by Internal Conversion to a State of $3d_{xy}$ Character", J. Phys. Chem. C* ***2015****, 119 (30), 17029-17038.* 

## 3.1 Abstract

The excited state dynamics of a vanadium oxo chelate complex are investigated using a combination of density functional theory, second-order perturbation theory, static UV-visible absorption spectroscopy, static x-ray absorption spectroscopy and time-resolved optical absorption spectroscopy. The vanadyl (V) compound has a broad visible absorption due to a ligand-to-metal charge transfer (LMCT) transition, whose character has been mapped out by density functional theory (DFT). In contrast to most first-row transition metal complexes under study having metal-to-ligand charge transfer excitations as the principal transition, $VOL^F$ displays a long-lived photoexcited state of 321 ps upon excitation of the charge transfer band in anhydrous tetrahydrofuran; a near two-fold decrease in lifetime is observed for the compound in a nonpolar solvent, anhydrous benzene. Theoretical calculations suggest that the extended lifetime is not due to triplet formation but rather may be attributed to a minimal optical dipole transition moment and poor Franck-Condon overlap. To complement the DFT analysis of the UV-visible absorption spectrum, pump dependence measurements are conducted on $VOL^F$ at three of the four major transitions within the broadband LMCT peak and are utilized in an attempt to create a global kinetic model of the chelate complex relaxation pathways. This compound represents one of the few examples of a long-lived first-row transition metal complex with an energetically useful excited state and, to the authors' knowledge, derived from a ligand-to-metal charge transfer transition. Understanding

of the early time components of the data is rendered somewhat difficult due to the many possible processes occurring within the early femtosecond to picosecond timescales. Further femtosecond fluorescence upconversion measurements are proposed as future means to verify our model.

## 3.2 Introduction

Organometallic complexes are of great interest for their various applications in pharmaceutical development [1], medical imaging [2], materials synthesis and catalysis [3, 4] as well as their photophysical properties [5]. In particular, the flexible choice of ligands and metal center(s) confers unique properties of solubility, reactivity and absorptivity that are major criteria for homogeneous photocatalytic materials. Over the last few decades, a variety of ligand families such as pi-acceptor ligated, low-valent metal oxido [6], nitrido [7], alkylidyne [8], peroxo [9], cyclopentadienyl, benzene, cycloheptatrienyl, pyridyl, and phosphine, have been investigated for photocatalytic systems. Polypyridyl groups have been the most prominent subject of research, with several derivatives containing Os, Fe, Co, Rh, Pt, and Ir centers [10–13] serving as photosensitizers and single electron reductants. Most notably, photoexcitation of ruthenium trisbipyridyl dichloride produces a long-lived (800 nanoseconds [14]), high energy triplet MLCT state that can be used for photosensitization as well as catalysis. [15, 16] Motivated in large part by the goal of scalable, earth abundant solar energy conversion materials, a shift towards the development of first-row transition metal complexes oxides has been observed over the last thirty years, with copper [17–20] and iron congeners [21–24] being most widely examined. However, very few molecular complexes containing first-row transition metal centers have displayed the long lifetimes necessary to drive chemical reactions at the nanosecond timescale.

To date, the greatest impediment to using these compounds is the rapid femtosecond relaxation of (metal-to-ligand) charge transfer excitations to the d-d manifold of the originating metal species. Many of these d-d states are, in fact, long-lived due to spin forbidden relaxation to the ground state [25–27] but also very low in energy—often approaching the ground state in energy—such that these excited states are energetically useless and catalytically inactive. [27, 28] This behavior is in stark contrast to corresponding precious metal complexes, where metal-centered states are significantly less strongly coupled with charge transfer states. [15] Recently, Sundström and Wärnmark synthesized a N-heterocyclic carbene iron complex with an extended lifetime of 9 ps in a highly excited state [29, 30]; derivatization with carboxylic acid moieties for adsorption onto $TiO_2$ nanoparticles revealed an even longer lifetime of the charge separated $^3$MLCT state (37 ps), with an electron injection efficiency of 92 %. [22] This complex is currently an anomaly, given that the typical relaxation of iron-based polypyridyl complexes is on the order of 100 femtoseconds. [22, 24]

Here, we explore the viability of a vanadium-based ligand-to-metal charge transfer complex to drive photocatalysis. Vanadium complexes are renowned for their diversity of valent states as well as their effectiveness in driving catalysis. The complex under study is

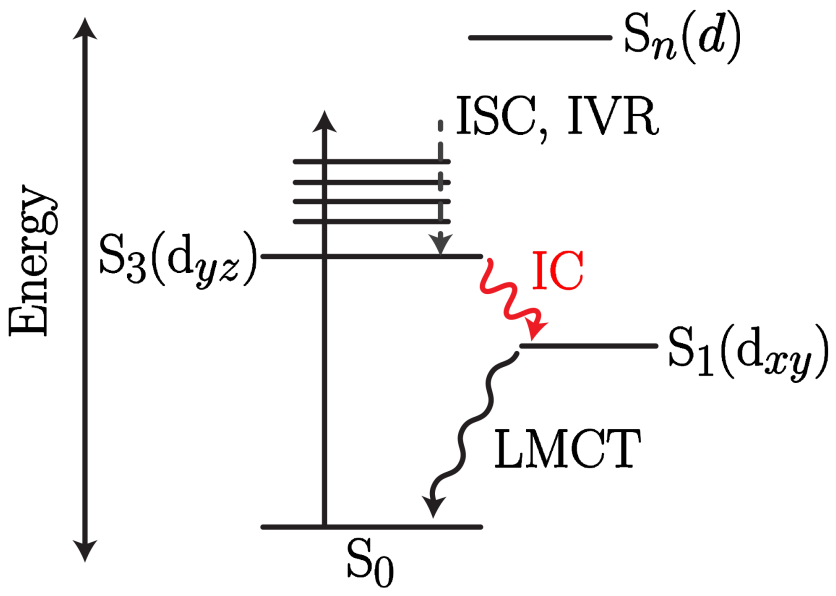


Figure 3.1: Proposed relaxation scheme for VOL$^F$.

an equatorially distorted $C_{3v}$ vanadium (V) oxido chelate, VOL$^F$, bound by a tetradentate aminophenol ligand. The excited state dynamics of VOL$^F$ are investigated with static optical and X-ray absorption, transient optical spectroscopy, as well as multiple levels of electronic structure theory. Ligand-to-metal charge transfer (LMCT) in a ground state $d^0$ metal complex, unlike metal-to-ligand charge transfer transitions, opens up the possibility of tracking the excited state evolution by following both the bleach of the initial LMCT transition as well as new ligand field absorptions from the $d^1$ center. By following the evolution of these two discrete signals, transient absorption measurements reveal a long-lived $3d_{xy}$ state following internal conversion from a photoexcited $3d_{yz}$ orbital. Density functional theory is employed to characterize the major components of the LMCT absorption band of the ground state, revealing four principal single particle transitions. Time-dependent DFT calculations are used to describe the geometries and electron-hole localization in the Franck-Condon and geometry-relaxed excited states. Neither static nor transient photoluminescence measurements can confirm the extended lifetime of VOL$^F$ as a consequence of triplet formation. However, calculations of transition matrix probabilities in the excited state indicate a near-zero transition dipole moment and minimal Franck-Condon overlap between the long-lived species and the ground state, due to a geometric distortion induced during thermalization of the initial excited state. Furthermore, the high oxidation state of the complex results in energetically high-lying metal 3d orbitals, as shown by electronic structure calculations. The only notable first-row complexes with high energy, long-lived $^3$MLCT states are $3d^{10}$

copper complexes, for which the d-block is completely filled in the ground state. [19, 31] A kinetic model is developed based on the observed lifetimes from our transient data. Additional pump wavelength dependence measurements are conducted in order to examine the relation of the four major transitions from TD-DFT to the proposed kinetic pathway but prove inconclusive in verifying the model.

## 3.3 Experimental Methods

### 3.3.1 Structure and Electrochemical Characterization

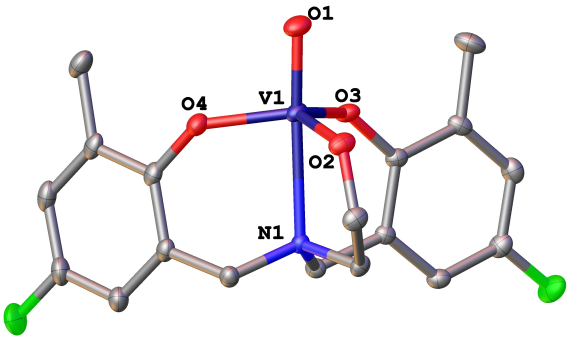


Figure 3.2: X-ray crystal structure of VOL$^F$, CCDC 1027781. Selected bond distances (Å): **V1-O1**: 1.5991(11), **V1-O2**: 1.7966(11), **V1-O3**: 1.8047(10), **V1-O4**: 1.8167(11), **V1-N1**: 2.3922(12). Selected interatomic angles (°): **O1-V1-O2**: 97.09(5), **O2-V1-O3**: 118.47(5), **O1-V1-N1**: 174.20(5). Hydrogen atoms have been omitted for clarity with thermal ellipsoids drawn at 50% probability.

Fig. 3.2 shows the X-ray crystal structure of the vanadium (V) oxido chelate VOL$^F$ under study, supported by the fluorinated tetradentate aminophenol ligand (L$^F$). Full synthetic details for $H_3L^F$ and VOL$^F$ are described in the original manuscript. [32]

By definition, LMCT results in metal-centered excited states where reduction photochemistry can be controlled by shifting the redox properties of the metal through either ligand modification and/or metal substitution. As a result, tuning of LMCT excited state energetics should be possible over a wide range. Electrochemistry of VOL$^F$ shows an irreversible V(IV/V) redox couple at -1.01 V vs. Fc/Fc$^+$, which suggests that this class of compounds has metal-centered excited states that are relatively strong reductants. VOL$^F$ therefore has the thermodynamic potential to photochemically drive the reduction of protons [33] to form dihydrogen in solar energy-to-fuels applications or to mediate organic transformations such as quinone reduction [34].

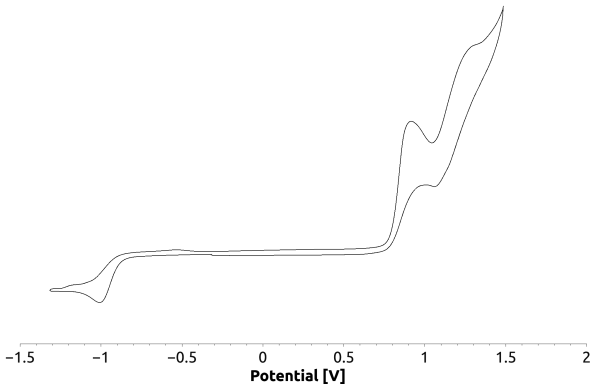


Figure 3.3: Electrochemistry of VOL$^F$ shows that an irreversible V(IV/V) redox couple at -1.01 V vs. Fc/Fc$^+$.

### 3.3.2 Theory

DFT calculations were completed using the Gaussian09 [35] and Q-Chem [36] codes. The molecule was relaxed using the HSE06 functional [37]. Consistency checks with B3LYP [38, 39] produced a consistent geometry. For the O, H, N, and F atoms we used the 6-31+G* basis set while we treated V orbitals with LANL2DZ [40] and its corresponding pseudopotential. All calculations were done with polarizable continuum models (based on benzene and tetrahydrofuran). Linear response TD-DFT was used to compute the static UV-vis spectra.

The spectra shown in Fig. 3.4 has an applied Gaussian blur with a FWHM of 6000 cm$^{-1}$ (which results in similar resolution to what can be seen experimentally) and is based on a configurational average of temperature perturbed structures. These structures were generated using *ab initio* molecular dynamics. Molecular dynamics calculations were done using the Q-Chem software package. Population analysis is based on the Mulliken formalism. Since MPA provides a non-unique description of electron localization, we also performed population analysis using the Modified Mulliken [41] and c$^2$ [42] methods. The two give the same qualitative picture.

Employing an 4 electron, 6 orbital complete active space (denoted CAS(4,6)), electronic energies were computed using multi-state multi-reference second-order perturbation theory (MS-CASPT2) at each of the reported geometries.

### 3.3.3 X-ray Absorption

X-ray absorption measurements were carried out at the Advanced Light Source (Lawrence Berkeley National Laboratory) at beamline 6.3.1.2. Beamline 6.3.1.2 is sourced by a bend magnet, capable of producing x-ray light at energies between 250-2000 eV which are mono-

chromatized with a VLS-PGM monochromator with a fixed exit slit and refocusing mirror. The resolving power is 5000 (E/$\Delta$E). Powder samples of VOL$^F$ were pressed onto a sliver of carbon tape that had been adhered to a copper metal puck. The sample puck was inserted into the main chamber at a vacuum of $10^{-7}$ torr, at room temperature, and oriented at a 45 degree angle with respect to both the incident x-rays and the detector. The samples were illuminated over the vanadium $L_{3,2}$- (510-530 eV) and oxygen K-edges (530-570 eV). All data were detected in fluorescence yield with a silicon drift detector, resulting in energy-resolved spectra over the region of interest (500-600 eV). Spectra were calibrated with respect to the oxygen K-edge in rutile titanium dioxide. [43]

X-ray absorption data were also collected for VOL$^F$ in tetrahydrofuran solution. The solution was contained in a static liquid cell sealed with a silicon nitride window for transmission of x-rays; absorption spectra were collected in fluorescence mode. The limited solubility of the oxovanadium compound in both polar and nonpolar solvents (maximum 3 mM) revealed that our spectra from the solid powder samples showed some detector saturation at the oxygen edge.

### 3.3.4 Static and Time-Resolved Photoluminescence

Static photoluminescence was measured on an Edinburgh Photonics FLS920 spectrometer. Samples of 1 $\mu$M VOL$^F$ were prepared in nitrogen-sparged spectroscopic grade THF (Sigma-Aldrich). The spectrum of VOL$^F$ was recorded with excitation and emission bandwidths of 4.0 nm, 1 nm step, and a 1 s dwell time; for comparison, the reported sensitivity of 6000:1 at the Raman band of water was collected at 350 nm excitation, 5 nm spectral bandwidth, and 1 s integration time. Three spectra were averaged. Upon excitation with 405 nm light, no photoluminescence from the VOL$^F$ sample was detected between 415 and 750 nm. A more concentrated, 1 mM solution of VOL$^F$ in THF was also prepared. This sample (recorded with excitation/emission bandwidths of 5 nm, 1 nm step size, 0.1 s dwell time) also showed no photoluminescence between 415 and 750 nm, possibly due to self-absorption.

### 3.3.5 Transient Optical Absorption

For the experimental set-up, the pump and probe pulses were sourced from the 800 nm output of a Ti:Sapphire regenerative amplifier (100 fs, 1 kHz, Libra, Coherent, Inc.). The output of a Coherent OPerA Solo optical parametric amplifier was employed as the pump pulse at various excitation wavelengths (390 nm, 425 nm and 480/500/525/550 nm), whereas a white light continuum (350-700 nm) generated from a $CaF_2$ window was used as the probe. Both pulses were directed into a HELIOS Femtosecond Transient Absorption Spectrometer (Ultrafast Systems, LLC) where, in an all reflective-geometry, the pump pulse (600 nJ) was focused at the sample (300 $\mu$m diameter) with a 10° incidence with respect to the probe. The probe pulse was focused into a fiber optic cable to a spectrometer equipped with multi-channel CMOS sensor; a reference pulse was split off from the continuum prior to transmission through the sample and directed into an identical spectrometer.

Solutions of $VOL^F$ were prepared in anhydrous tetrahydrofuran or anhydrous benzene and transferred to a 1 mm glass cuvette (Starna Cells, Inc.) for pump-probe measurements. Signal levels were linear for the concentrations (415 $\mu$M-1.25 mM) and pump fluences (0.275-5 mJ/cm$^2$) used in this study as determined by comparison and reasonable agreement with calculated levels. Calculated levels of signal change were based on static measurements of extinction coefficients and estimates of excited state concentrations based on pump fluence, sample concentration and pump-probe overlap volume. The integrity of the sample solution was monitored by UV-visible absorption spectroscopy, showing only a two percent decrease in optical density at the maximum wavelength (422 nm) over six hours of uninterrupted excitation at 5 mJ/cm$^2$ (390 nm); the observed degradation was considered negligible within the course of data acquisition. The spectral data acquired for each pump wavelength were collected as three averaged scans, each lasting for no more than 15 minutes.

Data obtained for each sample were subjected to pre-analysis treatment wherein the chirp of the white light probe was corrected (see Appendix A, GVD) and time zero was readjusted to the half-maximum of the peak signal at 425 nm where possible. For irradiation experiments with the pump centered at 425 nm, time zero is assigned such that the corresponding time value for this experiment agree for the half-maximum time zero in the spectra excited at 390 and 480 nm. Extraneous light in our transient data due to pump scatter was removed either through scattered light correction, via subtraction of the average light signal present before time zero, or a complete removal of the wavelength elements, resulting in the reduction in the absolute data matrix size. This was found to be necessary at wavelengths for which the pump signal overwhelmed the sample response, as observed with the benzene samples for 425 nm and 480 nm excitation wavelengths.

A negative absorption artifact attributable to Raman scattering from the solvent (THF and benzene) was observed in the $VOL^F$ data at early times ($< 200$ fs) in the spectrum $\sim$3000 cm$^{-1}$ from the pump pulse; this contribution has been removed from the data. A second transient absorption artifact averaging $\sim$2600 cm$^{-1}$ higher in energy than the excitation pulse was present in neat solvent and $VOL^F$ samples; the absorption was attributed to anti-Stokes Raman scattering and was also eliminated from the spectra at early times. The early transient response due to solvent alone, extracted from neat solvent samples, was also removed from the data collected at all excitation wavelengths for both benzene and tetrahydrofuran samples. Corrections for the solvent response, Raman response, and cross-phase modulation signal were not originally conducted for the published data at a pump wavelength of 390 nm. [32] However, both the original data and new data are considered here. The removal of these coherent artifacts reduces the number of time constants required for fitting but does not alter the general kinetic model that was developed from the uncorrected data. This is discussed in greater detail below.

# 3.4 Results

## 3.4.1 UV-Visible Absorption and Theory

UV-visible absorption measurements of VOL$^F$ gives the LMCT absorption spectrum shown in Fig. 3.4a. Using TD-DFT, the spectrum is reproduced and decomposed into its component transitions. There are four bright transitions that make up the ligand-to-metal charge transfer absorption, labeled as $S_1$-$S_4$ in descending wavelength. These excited states are shown in Fig. 3.5, where yellow denotes an electron, and blue is the corresponding hole. Electron-hole distributions are shown both for the initially excited electronic state with ground state geometry (Franck-Condon state) and at the relaxed minima of each excited state potential energy surface (Fig. 3.5a and b, respectively). Each excited state clearly contains LMCT character, involving charge transfer from one or both of the ligands to the metal center (unoccupied V d orbitals). The two frontier (HOMO-1 and HOMO) donating orbitals involved in these excitations are labeled as $\pi_-$ and $\pi_+$ respectively (Fig. 3.4b).

In the ground state geometry (indicated with a *), $S_2^*$-$S_4^*$ are made up of contributions from V d orbitals and both phenyl rings ($\pi_+$ and $\pi_-$). $S_4^*$ is an even combination of $\pi_-$ and $\pi_+$, while $S_3^*$ and $S_2^*$ have slightly more weight on the $\pi_-$ side. For clarity, all excited states are labeled by their largest d component. Fig. 3.4b shows the largest d component of $S_3^*$ as $d_{yz}$ since the transition is 60% $\pi_+ \rightarrow 3d_{yz}$. The lowest energy excitation, $S_1^*(d_{x^2-y^2})$, has the hole localized to one ligand; this state has only $\pi_+$ character. In the transient optical spectroscopy discussed below, the LMCT is excited at 390 nm (Fig. 3.4a). Since $S_3^*(d_{yz})$ and $S_4^*(d_{x^2-y^2})$ are close in energy, both states are initially populated due to Franck-Condon broadening. After excitation, the wave packet will evolve along the potential energy surface of each of the electronic states. Electron-hole dynamics will differ along each excited state surface. As the wavepacket moves along the potential energy surface, $S_3(d_{yz})$ and $S_4(d_{yz})$ lose their $\pi_-$ character; the hole becomes localized on $\pi_+$. The largest d component of $S_4$ changes from $d_{x^2-y^2}$ to $d_{yz}$. As a consequence to these changes, $S_3(d_{yz})$ and $S_4(d_{yz})$ essentially have the same character in the relaxed geometry (Fig. 3.5). $S_2(d_{yz})$ exhibits the opposite trend; relaxation along the excited state potential causes the hole to localize on $\pi_-$. The mismatch in hole localization ($\pi_+$ vs $\pi_-$) between $S_3(d_{yz})$/$S_4(d_{yz})$ and $S_2(d_{yz})$ suggests that internal conversion (IC) between these states is symmetry forbidden and unlikely to occur.

Conversely, the character of $S_1(d_{xy})$ is unaffected by relaxation. The hole remains localized on $\pi_+$ and therefore, IC from either $S_4(d_{yz})$ or $S_3(d_{yz})$ to $S_1(d_{xy})$ is possible. $S_3(d_{yz})$ and $S_4(d_{yz})$ are very similar in character and we excite both $S_4$ and $S_3$ states with our 390 nm pump, though the initially excited $S_3^*(d_{yz})$ state is significantly brighter than the $S_4^*$ state. For the sake of simplicity, we adopt $S_3(d_{yz})$ as the higher energy state in a two-state model of the low energy, relaxed charge transfer states. $S_1(d_{xy})$, the lowest energy excited state and the only one that can couple to either $S_3$ or $S_4$, is the lower energy state.

The excited state absorption spectra explored through our supercontinuum probe was also computed. There is more coupling optically (through the dipole matrix element) between $S_3(d_{yz})$ and higher states ($S_n(d)$) than from $S_1(d_{xy})$ (Table 3.2). The majority of the higher-

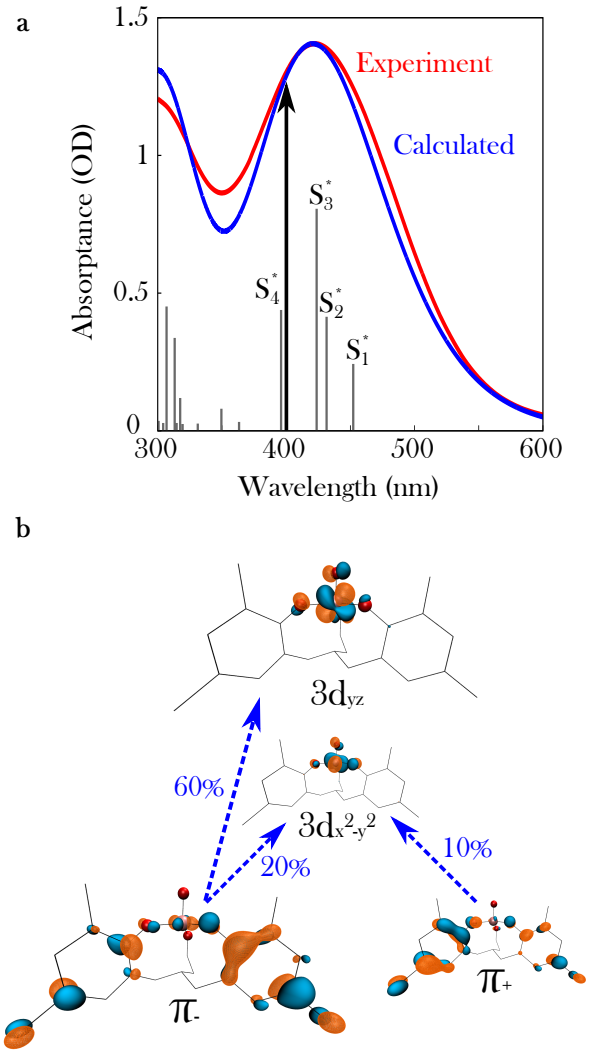


Figure 3.4: (a) Optical absorption of VOL$^F$. The broad absorption peak occurring for wavelengths longer than 400 nm is due to a charge transfer excitation from the ligand-to-metal center (LMCT). (b) Single particle orbitals contributing to the main transition (peak at 425 nm) into $S_3^*$. Vertical lines denote TD-DFT transition energies and oscillator strengths.

lying states within 3.0 eV are of LMCT character. From $S_3(d_{yz})$ up, ~60% of states are pure LMCT while the remaining 40% are mixed (not pure LMCT, MLCT or ligand-to-ligand charge transfer). Similarly, $S_4(d_{yz})$ has ~65% pure LMCT, and 35% mixed.

In order to calibrate where the nearest higher-lying LMCT states are, denoted by $S_n(d)$ in Fig. 3.1, x-ray absorption spectroscopic measurements of the O K-edge (1s absorption) were taken on VOL$^F$ (Fig. 3.6). Because LMCT states all have the electron primarily on vanadium, the energy differences between V LUMO orbitals, or the $d^1$ absorptions, are

indicative of the level splitting between LMCT states. The level alignment of the LUMO is informed by the pre-edge region of the O 1s spectrum that comprises three lower energy (529-535 eV) bands, each a mixture of oxygen 2p orbitals with vanadium 3d states. [44–47] Previous work has shown that for tetrahedral compounds of e and $t_2$ symmetries, [46, 47] the peak separation of these bands in the O K-edge reproduces observed d-d transitions fairly well. [44, 46] Therefore, the energy separation between the lower two peaks in the XAS

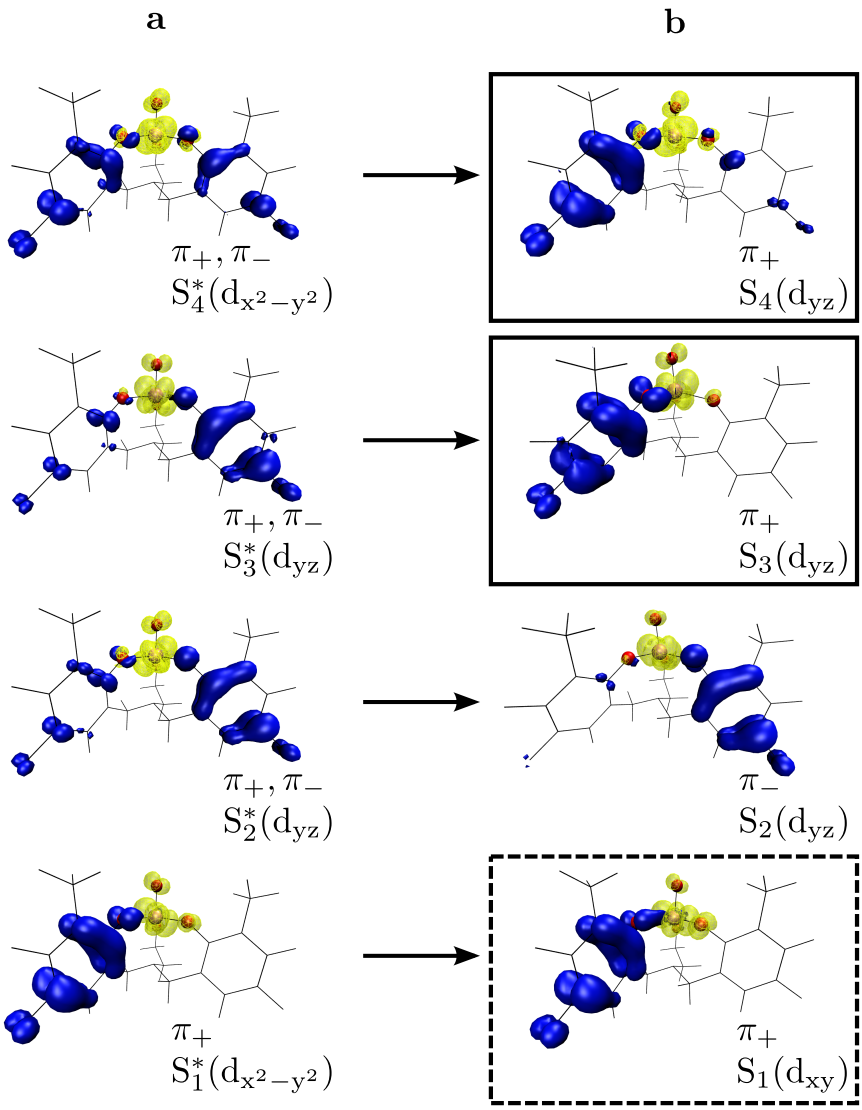


Figure 3.5: Electron-hole distribution for the first four excited states in the visible region. The hole is shown in blue and electron in yellow. This color scheme distinguishes the states from the single particle orbitals shown in Figs. 3.4 and 3.6.

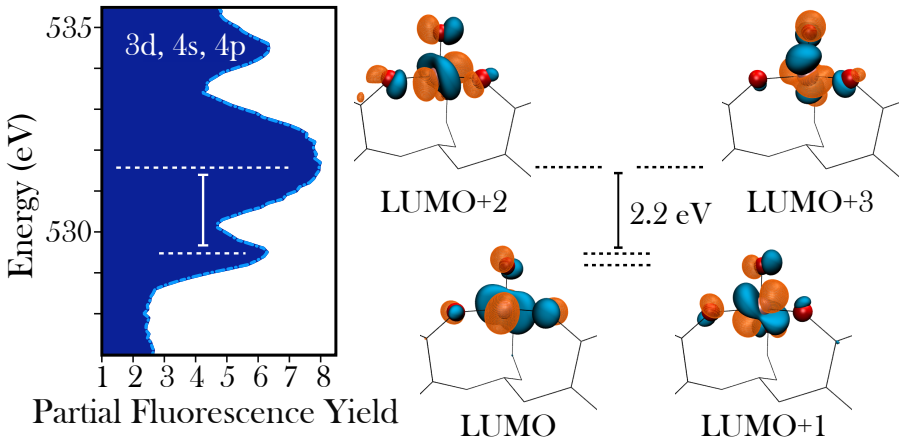


Figure 3.6: X-ray absorption spectrum of powder VOL$^F$ in PFY mode. Scheme shows the DFT d orbital (dashed lines) splitting based on observed transition energies from XAS.

spectrum, 2.2 eV, is assigned to the level splitting between the lowest LUMO orbitals (two degenerate pairs, LUMO/LUMO+1 and LUMO+2/LUMO+3), indicative of excited state absorption from the initial LMCT to the next higher LMCT state. [48–52]

### 3.4.2 Static and Time-Resolved Luminescence Measurements

Unlike the MLCT compounds discussed above, there is no observed static photoluminescence. The absence of photoluminescence suggests that the long-lived charge transfer state is not easily ascribed to triplet formation. An alternative method to identify triplet formation is to estimate the energy barrier for ground state recovery and compare it to previously measured singlet-triplet intersystem crossing (ISC) activation barriers that lead to long-lived states. In order to determine the upper limit for the energy barrier to ground state recovery, a simple Arrhenius model was applied to the measured decay rate at room temperature (321 ps) in the ultrafast optical experiments below and the rate at -80 °C. At -80 °C, we were unable to observe any transient absorption signal on the nanosecond timescale; the experimental details and results are described in the supporting information of the original manuscript. [32] The time resolution of the nanosecond transient absorption measurement, and therefore the upper bound for the lifetime of this transition at -80 °C, is $\sim$ 2 ns. Using these two data points we conclude that the energy barrier is less than 50 meV. This 50 meV maximum barrier is significantly lower than the precedent set for ISC by rubrene in sucrose octaacetate matrix, which is on the order of 160 meV. [53]

The negative results obtained here do not preclude the possibility of intersystem crossing to a triplet state within early timescales. Indeed, rapid ISC on the order of hundreds of

femtoseconds is expected for metal-to-ligand charge transfer first row transition metal complexes. [27] Given that no conclusive evidence towards the existence of a triplet state has been found for VOL$^F$, fluorescence upconversion measurements would be useful to confirm that the LMCT complex is a unique exception to the rule.

### 3.4.3 Broadband Transient Absorption Data

Initial measurements were conducted on a solution of VOL$^F$ in tetrahydrofuran, with pump excitation at 390 nm and probe range of 400-700 nm. Minimal depletion of the LMCT bleach was observed after several hours (six) of excitation at 390 nm at 5 mJ/cm$^2$.

Excitation of VOL$^F$ at 390 nm leads to the transient spectrum, probed from 400 nm-700 nm, shown in Fig. 3.7. This spectral region comprises the LMCT excitation into the initial charge transfer states ($\sim$ 400 nm - 525 nm) and excited state absorptions ($\sim$ 500 nm - 600 nm). Transient spectra were collected at both short time delays (100-500 fs, Fig. 3.7a) and longer time delays (1-500 ps, Fig. 3.7b). To aid assignment of the transient signals, the transient spectra are compared to the static UV-vis LMCT spectrum in each time window, at 100 fs and at 36 ps. In the region of 400-525 nm, the transient spectra exhibit a -$\Delta$mOD associated with a ground state bleach (GSB) and stimulated emission (SE). An excited state absorption dominates in the region beyond 525 nm for times faster than 36 ps. After 36 ps, the ESA has decayed substantially and the transient spectrum largely follows the UV-vis LMCT spectrum (Fig. 3.7b).

Notably, the transient spectrum contains an isosbestic point (475 nm) for the time window 1 ps to 36 ps, where the $\Delta$mOD is time-independent (Fig. 3.7b). For the isosbestic point to appear in a transient spectrum, there must be negligible back electron transfer to the ground state. This suggests that at these timescales there is a concentration of total *excited* carriers that is constant over the entire spectral region, but whose contribution exchanges between two different excited electronic populations that both contribute to the spectrum. [54–56] $S_3(d_{yz})$ and $S_1(3d_{xy})$ described in a two-state model for VOL$^F$ can account for these two populations. An isosbestic point would result from internal conversion (IC) between these two states. A detailed description of the isosbestic point will follow after a discussion of the kinetic components of these spectral signals.

For our kinetic analysis, we applied a sum of single exponential functions—each convolved with the Gaussian instrument response function (IRF) of our system (FWHM 100 fs)—as the fitting function for the kinetic traces in most spectral regions (Eq. 3.1). The excepted region (540-590 nm, centered about the peak of the ESA) was modeled with a slight variation on the general summation to account for a small rising component (Eq. 3.2). Time constants were extracted from global fits of multiple kinetic traces at 10 nm increments within a particular spectral region, as described in Appendix A.

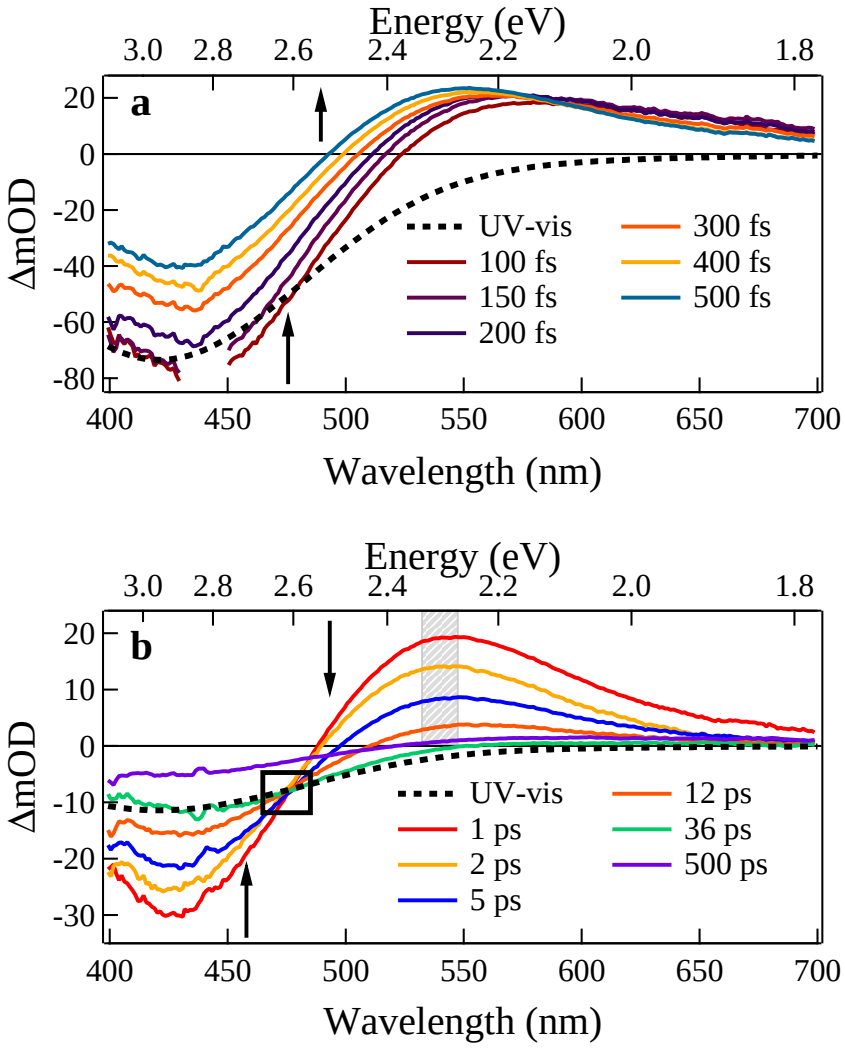


Figure 3.7: Transient spectra of VOL$^F$ following excitation at 390 nm at (a) very short and (b) long time delays. The included arrows indicate the direction in which the spectra evolve over time. At longer delay times, an isosbestic point is observed (box). The ligand field transition energy suggested by x-ray measurements is shaded for comparison with the transient spectrum (b). The dotted line in both panels represents the ground-state LMCT absorption.

$$\begin{aligned}\Delta\text{mOD} &= \sum_{i=0}^{n} \text{A}_i e^{-t/\tau_i} \bigotimes \text{IRF} \\ &= \sum_{i=0}^{n} \text{A}_i e^{(\frac{\sigma^2}{2\tau_i^2} - \frac{t}{\tau_i})} \Big[1 + \text{erf}\big(\frac{t}{\sigma\sqrt{2}} - \frac{\sigma}{\tau_i\sqrt{2}}\big)\Big]\end{aligned} \tag{3.1}$$

$$\Delta\text{mOD} = \Big[\text{A}_{rise} e^{-t/\tau_{\text{rise}}} + \sum_{i=0}^{n} \text{A}_i \big(e^{-t/\tau_i} - e^{-t/\tau_{rise}}\big)\Big] \bigotimes \text{IRF} \tag{3.2}$$

In Fig. 3.8a, the kinetics probed by the GSB/SE transition reveal rapid relaxation of the initial state followed by a much longer decay. The kinetics are well-represented by a triexponential function composed of fast 0.180 ps ± 0.005 ($\tau_{\text{ISC-IVR}}$), intermediate 7.27 ps ± 0.32 ($\tau_1$), and slow 455 ps ± 30 ($\tau_2$) time constants. The expected amplitude of the transient signal at time zero (-80 ΔmOD) agrees with the signal estimate (-100 ΔmOD), which is based on the concentration of VOL$^F$ in solution, the pump power, and an LMCT extinction coefficient derived from static UV-vis as related through the Beer-Lambert Law. There are at least two physical phenomena that could be attributed to the 0.18 ps time constant: singlet-to-triplet intersystem crossing (ISC) and intra-/ intervibrational relaxation (IVR). For the majority of the MLCT compounds studied previously, a fast 0.02-0.1 ps ISC is observed as a stimulated emission signal from the singlet state significantly red-shifted from the GSB and then a much weaker, further red-shifted emission signal of the triplet state. [57] Stimulated emission related to ISC may be less important in VOL$^F$ since no long-lived emission is observed, the 0.18 ps time constant is observed in the region of the GSB rather than in a red-shifted spectrum, and there is general agreement of the signal magnitude with expectations from a GSB. However, it may also be the case that the SE in VOL$^F$ is not significantly red-shifted from the GSB or that the ESA contribution masks the true SE signal. IVR of the initially excited Franck-Condon state to a relaxed state that is less well-coupled to the ground state geometry will certainly be present; this can also account for the 0.18 ps time constant. Given the TD-DFT description where the hole localizes to $\pi_+$ and the d-electron undergoes symmetry changes (Fig. 3.5), this IVR could be quite large; this is further indicated by the 90% reduction in the transition dipole back to $S_0$ for $S_3^*$ calculated by MS-CASPT2 (Table 3.1). The time constant of 0.18 ps is tentatively attributed to a combination of ISC and IVR ($\tau_{\text{ISC-IVR}}$). Resolution of the ISC and IVR contribution to $\tau_{\text{ISC-IVR}}$ through separate ultrafast fluorescence studies that would directly detect SE [57, 58] is proposed for future experiments.

Because IVR and ISC are expected to be on the order of hundreds of femtoseconds, the two later time constants (7.27 ps ($\tau_1$), 455 ps ($\tau_2$)) should originate from transitions involving vibrationally relaxed excited populations. The observation of two long time scale contributions to the GSB decay is unlike that seen in the canonical $Ru(bpy)_3^{2+}$ or recent $Fe(bpy)_3^{2+}$. In these cases, subpicosecond ISC, IVR, and IC are followed by a single long time constant identified by GSB traces and attributed to a fluorescent, charge transfer state

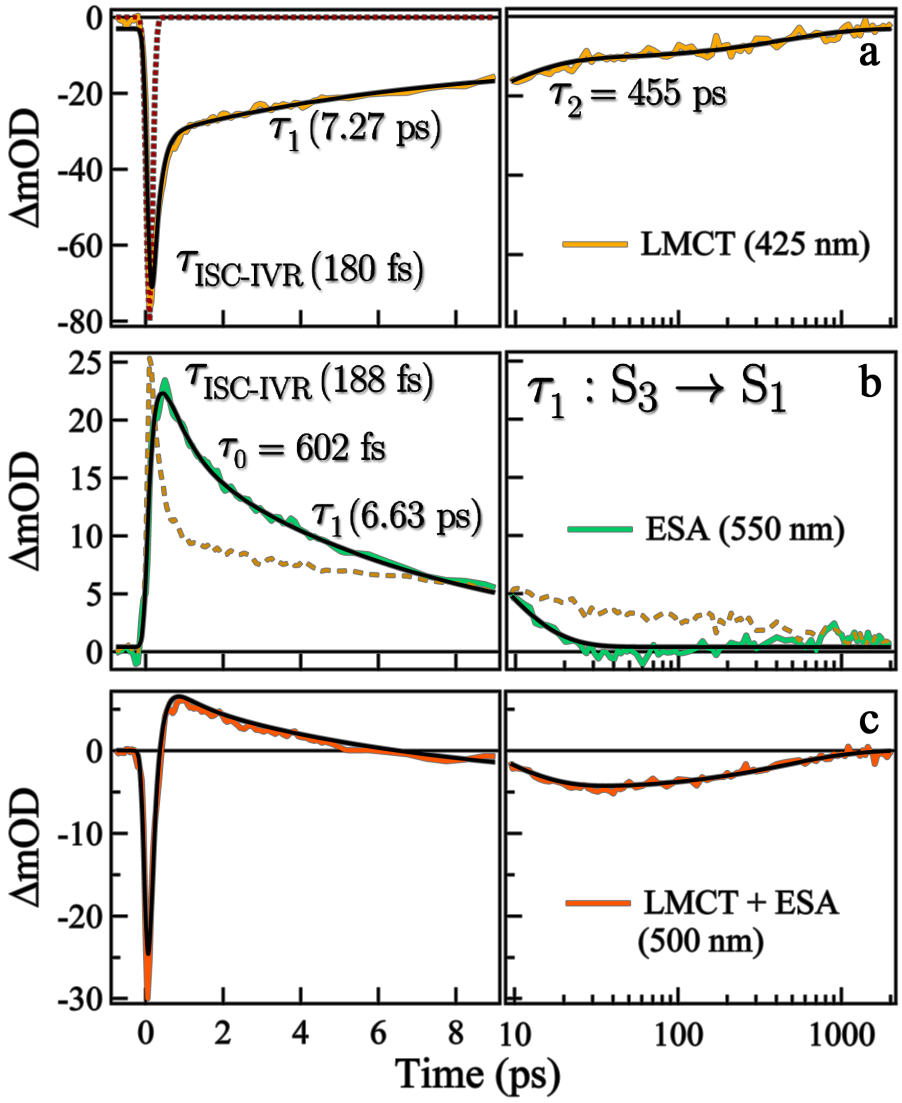


Figure 3.8: Kinetic traces of VOL$^F$ following excitation at 390 nm shown at (a) 425 nm, (b) 550 nm, and (c) 500 nm. The LMCT GSB/SE and ESA dominate in the first two kinetics, respectively. The 500 nm trace contains overlapping contributions from both signals. In panel (a) the instrument response function is shown (red, dotted line) to compare the rapid decay of the GSB signal. In (b), the LMCT GSB is reproduced (yellow, dotted) to compare early timescales with the ESA.

in $Ru(bpy)_3^{2+}$ and the high spin metal-centered state in $Fe(bpy)_3^{2+}$. [14, 59, 60] Indeed, VOL$^F$ has two closely spaced charge transfer states $S_3$ and $S_1$ that could both contribute significantly to the GSB spectral decay (Fig. 3.4a, Fig. 3.5). The clear resolution of the two time scales in the GSB traces in VOL$^F$ could be a result of a population exchange between

| Transition | Transition Dipole |
|---|---|
| $S_1^* \rightarrow S_0$ | 0.0324 |
| $S_3^* \rightarrow S_0$ | 0.1075 |
| $S_1 \rightarrow S_0$ | 0.0015 |
| $S_3 \rightarrow S_0$ | 0.0120 |

Table 3.1: Calculated transition dipole moments in the LMCT GSB region, from a single excited state to the ground state.

the initially excited $S_3$ population and the lower energy $S_1$ population, i.e. a series pathway that comes from internal conversion between the two CT states. On the other hand, the separation of the two time scales could also result from a parallel pathway, in which both $S_3$ and $S_1$ decay back to the ground state with different time constants. DFT calculations that reproduce the LMCT UV-vis spectrum indicate that the relaxed geometry of $S_3(d_{yz})$ has an appreciable transition dipole to the ground state ($S_3(d_{yz}) \rightarrow S_0$). In contrast, the calculated transition dipole moment for $S_1(d_{xy}) \rightarrow S_0$ is significantly smaller, by an order of magnitude (Table 3.1). This would affect how each transition contributes to the GSB and their decay, in either a series or parallel model.

The decay kinetics probed by the ESA spectrum, shown in Fig. 3.8b, can be fit with a tri-exponential function containing one rise component and two decaying components (Eq. 3.2) having time constants of 0.188 ps $\pm$ 0.024 ($\tau_{\text{ISC-IVR}}$), 0.602 ps $\pm$ 0.054 ($\tau_0$), and 6.63 ps $\pm$ 0.12 ($\tau_1$), respectively, in the region of the maximum of the ESA (2.3 eV, 540-590 nm). The similarity of $\tau_1$ with the intermediate time scale observed in the GSB traces (7 ps) relates the decay of the ESA to the same state involved in the GSB/SE kinetics. Two possibilities exist to explain the nearly identical intermediate lifetimes in the two spectral regions. If a series pathway/internal conversion between the two charge transfer states were involved, then the ESA decay would report uniquely on the decay of $S_3$. Alternatively, in a parallel scheme, the ESA would report on either $S_3$ or $S_1$, and $\tau_1$ would track the relaxation of both $S_3$ and $S_1$ to the ground state. The isosbestic point observed between 1 ps and 36 ps—in the same time frame that the IC would be expected by $\tau_1$ of the ESA—primarily points to internal conversion. It follows that the ESA signal arises from the $S_3$ state, and that the decay of the ESA signature $\tau_1$ describes the rate of internal conversion. In support of this assignment, our initial excitation is at 390 nm, $\sim$ 0.5 eV away from the poorly absorbing $S_1$ state. Therefore, $S_1$ is unlikely to be substantially populated following initial excitation such that it could account for the rather large +20 $\Delta$mOD ESA at early times. Internal conversion, on the other hand, could significantly populate the $S_1$ state. Because the time constant $\tau_0 \sim 0.602$ ps occurs exclusively with $\tau_1$ 6.63 ps in the ESA kinetics, it likely arises from IVR within $S_3$. The rise time of 0.188 ps is determined by the inclusion of a negative amplitude exponential to modulate the amplitude of subsequent decay (Eq. 3.2). Since it is similar to the fast 0.180 ps $\tau_0$ of the LMCT GSB, it is possible that it results from an overlapping -$\Delta$mOD and therefore could be related to IVR or ISC. Finally, we note that

the large ESA observed also invalidates attributing 6.63 ps $\tau_1$ or 0.6 ps $\tau_1$ to an ISC, since excited state absorptions will primarily be determined by the electronic structure, regardless of whether the initial state is a singlet or triplet with respect to the ground state.

| Transition | Transition Dipole |
|---|---|
| $S_1^* \rightarrow S_n$ | 0.017 |
| $S_3^* \rightarrow S_n$ | 0.017 |
| $S_1 \rightarrow S_n$ | 0.009 |
| $S_3 \rightarrow S_n$ | 0.038 |

Table 3.2: Transition dipole moments in the ESA d-d region, integrated over all unoccupied states 2.0-2.5 eV higher in energy than the originating excited state.

Given the evidence for internal conversion, the assignment of the excited state absorption to either $S_3$ or $S_1$ is considered. DFT calculations show that the majority of the higher lying excited states to which there could be an absorption are of LMCT character; consequently, the contributions to the ESA from $S_n(d)$ are likely (Table 3.2). A positive assignment of the ESA to higher lying LMCT states comes from the energy of $d^1$ transitions obtained by XAS of the O K-edge (Fig.3.6). The ESA, with a peak at 550 nm (2.3 eV) (Fig. 3.7b) comes very close to the splitting (2.2 eV) of the two lowest pre-edge peaks in the XAS spectrum. These were considered uniquely attributable to d-d transitions with significant oxygen 2p character as discussed above. A 2.2 eV absorption also agrees with $d^1$ absorptions in vanadium (IV) compounds in the literature. [48–52]

While a positive assignment to a ligand field transition can be made based on the agreement of the ESA and the XAS data, there are three other possible transitions that could account for the ESA. These include MLCT, di-cation LMCT, and intraligand transitions. An di-cation LMCT transition is the least likely candidate as removal of a second electron from the ligand to create a dication is highly unfavorable; such a transition is expected to appear significantly blue-shifted from the LMCT. An excited state MLCT transition could come from excitation of the electron in vanadium d LUMO orbitals to a higher lying ligand LUMO orbital. However, in our TD-DFT calculations we do not see any pure MLCT transitions up to 3.0 eV away from the relaxed states. The intraligand hole excitation to lower-lying occupied molecular orbitals is the only real alternative to a higher-lying LMCT state as an assignment of the ESA. Ideally, one would perform spectroelectrochemical measurements of the ligand to determine the UV-VIS spectrum of the ligand cation. Unfortunately, electron or hole transfer by electrochemistry decomposes the ligand. In the measurements done, both oxidative and reductive spectroelectrochemistry of VOL$^F$ demonstrate complex decomposition without discernible formation of redox products by optical absorption spectroscopy.

In order to clarify the roles of the ligand hole and $S_n(d)$ to the ESA, singular value decomposition (SVD) transformation of our transient data was carried out and a global analysis subsequently applied as detailed in Appendix A. For our global analysis, the general model (Eq. 3.1) used in our earlier fits was applied to the resultant SVD kinetic eigenvectors.

Through global analysis, time constants associated with the excited state were extracted without regard to particular spectral regions. The best fit for the global analysis was obtained from a tetraexponential function, producing decays of 141 fs, 777 fs, 6.85 ps and 423 ps, in good agreement with the parameters obtained from our prior fits. The corresponding normalized decay-associated spectra (DAS), reflective of the relative spectral contributions for each time constant, are shown in Fig. 3.9.

At early times following excitation, the creation of the initial charge transfer excited state is illustrated by DAS1, consisting of both an LMCT GSB and the ESA (141 fs, Fig. 3.9). Importantly, the 423 ps spectrum, DAS4 is nearly identical to DAS1 in both the LMCT GSB and the ESA. The fact that an ESA persists at longer time scales and is so similar to the initially excited charge transfer state points to the fact that the long-lived state is indeed of charge transfer character. However, the similarity of the ESA at the two time scales might not at first seem consistent with the involvement of two different charge transfer states, $S_3$ and $S_1$. This could be reconciled by an ESA of common origin for the two states agnostic of the excited state electron character, with the most likely candidate being a ligand hole absorption. The similarity in DAS1 and DAS4 likely comes from the fact that, in both, the GSB reports on the unexcited population through the $S_3^*$ transition, while the ESA reports on the total excited state population through the ligand hole transition. Furthermore, the

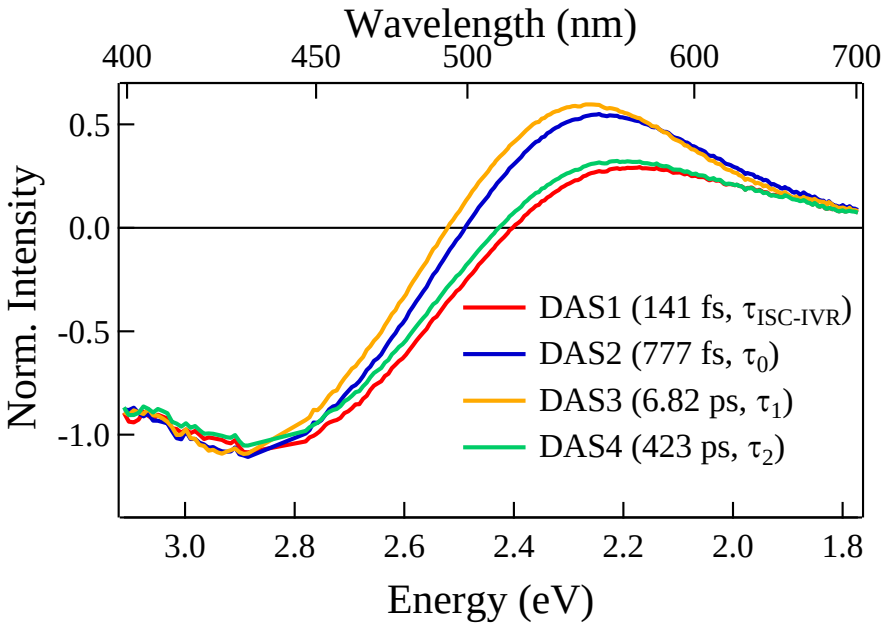


Figure 3.9: Normalized decay associated spectra (DAS) for the associated time constants (141 fs, 777 fs, 6.82 ps, and 423 ps) determined by our global analysis. As with Fig. 3.7a, Raman scattering from the tetrahydrofuran solvent has been removed from the DAS at 2.8 eV.

ESA of DAS1 and DAS4 also occurs in DAS2 and DAS3, and is therefore present throughout the ground state recovery, again indicating an ESA of common origin.

On the other hand, a comparison of the decay-associated spectra at intermediate times (DAS2, 777 fs and DAS3, 6.85 ps) with the early/late DAS reveals an additional ESA. The ESA is slightly blue-shifted from the ESA assigned to the ligand hole and has a significantly greater intensity with respect to the GSB. This blue-shifted ESA is peaked at 2.3 eV, the energy of a d-d transition roughly indicated by our XAS oxygen pre-edge (2.2 eV). The presence of this $d^1$ absorption at intermediate times and its disappearance at longer times despite a long-lived CT state can be explained by internal conversion from $S_3$ to $S_1$ over 1-36 ps, where the absorption from $S_3$ far exceeds that of $S_1$. This explanation is corroborated by theory with our calculation of significantly reduced optical coupling to higher-lying d states from $S_1$ ($S_1(d_{xy})\rightarrow S_n(d)$) as compared to $S_3$ ($S_3(d_{yz})\rightarrow S_n(d)$) (Table 3.2). The analysis of the kinetic traces of the ESA above, the similarity in the DAS2 and DAS3 spectra, and the rationale given by the TD-DFT calculations, assigns these two intermediate time constants to the $S_3(d_{xy})$ state. Further, the unique ESA of this state, regardless of the exact assignment, means that its disappearance at later times is related to changes in the electronic nature of the excited state rather than relaxations within a similar state, either due to IVR or solvent dynamics. This suggests that the isosbestic point is electronic in nature and supports an internal conversion occurring with a 6.8 ps time constant.

Contributions of the isosbestic point to the transient spectrum, as demonstrated by Han *et al.* [54], can be written as:

$$\Delta mOD = (-\epsilon^3_{LMCT} + \epsilon^3_{d-d})[S_3(d_{yz})(t)] + (-\epsilon^1_{LMCT} + \epsilon^1_{d-d})[S_1(d_{xy})(t)] \tag{3.3}$$

where $\epsilon^3_{LMCT}$, $\epsilon^1_{LMCT}$ are the $S_3(d_{yz})\rightarrow S_0$, $S_1(d_{xy})\rightarrow S_0$ transitions and $\epsilon^3_{d-d}$, $\epsilon^1_{d-d}$ are the $S_3(d_{yz})\rightarrow S_n(d)$, $S_1(d_{xy})\rightarrow S_n(d)$ transitions. The ligand hole contribution to each state is not included because the normalized DAS suggest that the absorptions, relative to the LMCT GSB, are similar in magnitude and would negate one another in the calculation of the isosbestic point below. Further, the ligand hole contribution at the wavelength of the isosbestic point, 475 nm, if any, is strongly overshadowed by the LMCT GSB and the ESA of $S_n(d)$ origin. The analysis of isosbestic points in transient absorption spectra at the many picoseconds time scale is precedented. [61–63]

The isosbestic point requires a population exchange, such that $[S_3(t)] = c_0 - [S_1(t)]$, where $c_0$ represents the excited state population after IVR and ISC in the initial picosecond. For the $\Delta$mOD to be time independent at 475 nm from 1 ps to 36 ps, the extinction coefficients must be, at 475 nm, related in the following way: $-\epsilon^3_{LMCT} + \epsilon^3_{d-d} = -\epsilon^1_{LMCT} + \epsilon^1_{d-d}$. In order to see if this is viable, we can utilize extinction coefficients for the LMCT back to $S_0$ and for the ESA transitions to $S_n(d)$ (summed over 2.0 to 2.5 eV) calculated by TD-DFT for both states. Since the extinction coefficients reported in the tables indicate an average magnitude, these are taken to represent the maximum wavelength extinction coefficient (425 nm) and are subsequently scaled to reflect a Gaussian absorption profile to determine the relative absorptivity at 475 nm. For the LMCT transition, the scaling is 50 % from the UV-vis

absorption. The ESA transition to $S_n(d)$ is harder to estimate, but DAS2 and DAS3 suggest that 10% as a higher bound is reasonable. With these considerations, the equation roughly holds, where it is imbalanced by $\sim 4$ % of the transition dipole for the initial $S_3^*$ transition. A final note on these extinction coefficients is that the deconvolved spectra (DAS2 and DAS3) and the TD-DFT calculations suggest that $\epsilon^3_{LMCT} \sim \epsilon^3_{d-d}$. While extinction coefficients are generally much weaker for d-d than LMCT transitions, these d-d transitions involve two LMCT states, which can significantly enhance optical d-d transitions from what one would normally expect in the ground state. [28, 64, 65]

#### 3.4.3.1 Addendum to Published Work: Cross-Phase Modulation

While the original published work detailed the use of four time constants to describe the relaxation of VOL$^F$, it was determined that the early rising component was extraneous. The unnecessary addition was noted after significant contributions of cross-phase modulation at longer wavelength excitation were found to interfere with global analysis and had to be removed (Fig. A.1c). After removal of cross-phase modulation from the original data with illumination at 390 nm, the 777 fs lifetime component was not extracted from singular value decomposition analysis. Instead, global analysis of the VOL$^F$ eigenkinetic traces under 390 nm excitation yielded time constants of 142 fs, 5.76 ps and 321 ps in THF, in Table 3.3 and Fig. 3.11a.

The prior analysis of the decay-associated spectra that assigns the DAS2/DAS3 absorptive component to a transient d-d transition remains valid under the new time constants. In Fig. 3.10, the decay-associated spectra for 142 fs (DAS1.1) and 321 ps (DAS3.1) are identical and attributed to the ground-state bleach; unusually no ligand hole excited state absorption was observed. The signature that was previously ascribed to the ligand hole ESA appears to have been, in fact, a result of the cross-phase modulation signal at early times. DAS2.1 for the 5.76 ps component shows an additional, larger excited state absorption which is assigned to the transient d-d transition. The assignment of the ESA to the ligand field transition is still valid; a ligand hole absorption is expected to appear constant for the entire duration of the LMCT GSB, which contradicts the observation of a very short ESA lifetime (5.76 ps) relative to the long-lived bleach (321 ps). Additionally, the analysis of the isosbestic point still holds as removal of the cross-phase modulation contribution within the first picosecond does not affect the later kinetics in the tens of picoseconds over which the excited state population exchanges. All subsequent discussion of the results reflect the triexponential model and its associated time constants following removal of cross-phase modulation contributions.

#### 3.4.3.2 Solvent and Excitation Wavelength Dependence

To examine the dielectric nature of the photoexcited charge-separated state, the dependence of VOL$^F$ kinetics to solvent polarity was investigated. We note that in the static ultraviolet-visible spectrum, no significant solvatochromism was observed; sample-to-sample variation in the peak position of the absorption spectrum up to $\sim$10 nm was observed but was found

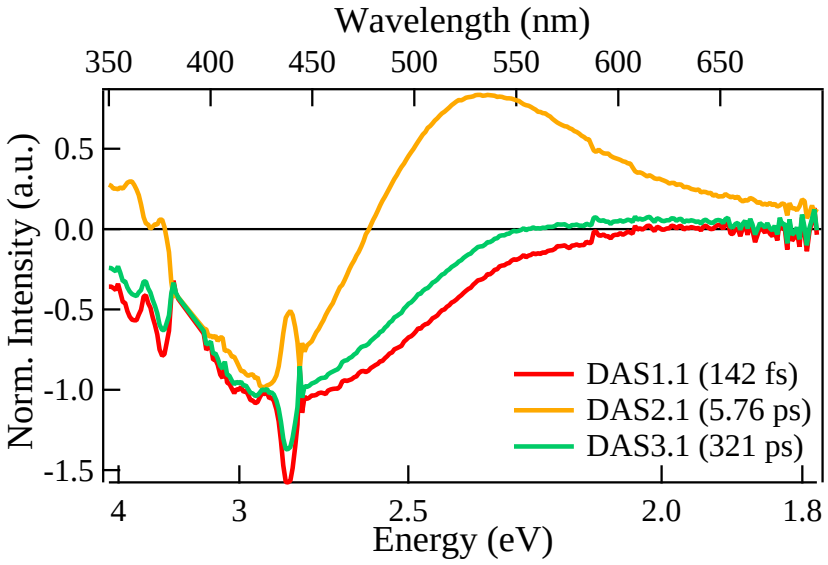


Figure 3.10: Normalized decay associated spectra (DAS) for the new time constants (142 fs, 5.76 ps, 321 ps) determined by our global analysis of the data following removal of cross-phase modulation.

to be independent of solvent polarity. Interestingly, there is very little difference between the observed early timescales but a significant decrease in the long lifetime duration by a factor of 1.5 (Table 3.3). Solvent relaxation is expected to occur on the order of hundreds of femtoseconds to tens of picoseconds, which may account for the similarity of the kinetics in the first ten picoseconds. Notably, the isosbestic point is preserved in the transient data, apparently independent of the polarity of the solvent.

In addition to changing the solvent for our VOL$^F$ samples, the excitation wavelength was also varied. For the original experiments, excitation of the $S_4$ transition was carried out at 390 nm rather than the nominal 400 nm to allow the full spectral probe window to be examined with minimal pump light scatter. Subsequent interrogation of the transitions at $S_3$ (425 nm) and $S_1$ (460 nm) were carried out to determine if any variation in the spectra or kinetics could be identified as predicted by theory. Excitation at the transition $S_2$ (437 nm) was not examined due to its proximity to transition $S_3$. Instead, transition $S_1$ at 460 nm was selected. We opted to excite this transition at 480 nm rather than at the nominal wavelength to avoid excitation of transition $S_2$ and even $S_3$. Due to a combination of Franck-Condon broadening and the breadth of our "monochromatic" OPA output, comprising 10 nm at the full-width half-maximum but covering approximately 20-40 nm due to scatter, excitation of these two transitions at the $S_1$ transition wavelength cannot be ruled out. Data were also collected with excitation wavelengths centered at 500, 525, and 550 nm, on the absorption tail

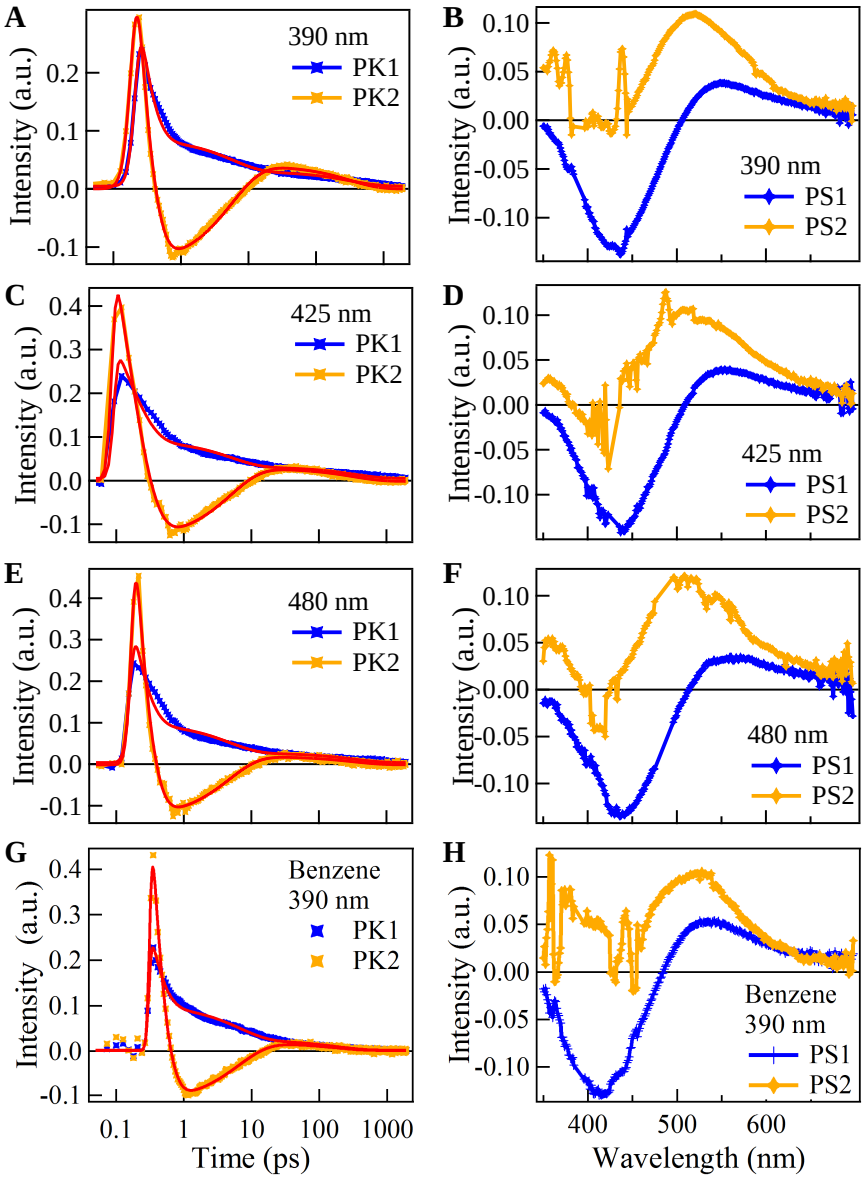


Figure 3.11: Singular value decomposition of VOL$^F$ transient data excited at (a,b) 390 nm, (c,d) 425 nm, and (e,f) 480 nm in tetrahydrofuran. The 390 nm data for VOL$^F$ in benzene are presented in panels g and h. Panels a, c, e, and g display the first eigenkinetic components, and panels b, d, f, and h the corresponding eigenspectra. Only the first two principal components were analyzed.

of the ligand-to-metal charge transfer transition. Surprisingly, these data displayed identical transient behavior to the data obtained with a 480 nm excitation wavelength; consequently, these spectra and kinetics are not included here.

| THF | $\tau_{\text{ISC-IVR}}$ (ps) | $\tau_1$ (ps) | $\tau_2$ (ps) |
|---|---|---|---|
| 390 nm | 0.142 | 5.758 | 321.283 |
| 425 nm | 0.143 | 5.015 | 326.778 |
| 480 nm | 0.120 | 4.728 | 326.146 |
| Benzene | | | |
| 390 nm | 0.177 | 6.560 | 181.263 |
| 425 nm | 0.194 | 7.415 | ∼195 |
| 480 nm | 0.137 | 6.542 | 205.437 |

Table 3.3: Excitation wavelength dependence time constants extracted from global analyses of first two eigenkinetic traces generated by singular value decomposition.

Surprisingly, there was no stark difference in the transient behavior between excitation at 400, 425 and 480 (500-550) nm, as shown in Table 3.3. The eigenkinetics of the transient data were examined to avoid the confounding variable of relative initial populations and absorptivity at the different pump positions. Fits of the first two eigenkinetics at each wavelength gave nearly identical time constants (Fig. 3.11). With higher excitation wavelength, the intermediate time constants of approximately 5-6 ps showed a slight decrease, whereas the long time constant showed a minor increase with wavelength. The longer lifetime of VOL$^F$ in tetrahydrofuran relative to that in benzene was preserved across the examined pump excitations; though the benzene pump dependence experiments showed more variability in measured lifetimes.

## 3.5 Discussion

### 3.5.1 Relaxation Pathway of VOL$^F$

The results show that a long-lived excited LMCT state is created by internal conversion between two charge transfer states, differentiated by their vanadium d-character—$S_3(d_{yz})$ and $S_1(d_{xy})$. The exchange of excited state population between these two ligand field states is evidenced by (1) an isosbestic point at intermediate time scales (from 1 ps to 36 ps); (2) the recovery of the LMCT GSB with two time constants (5.76 ps and 321 ps) following initial relaxation or recombination; (3) a distinct 5.76 ps decay observed in the kinetic traces of the ESA and DAS2.1 within the time window of the isosbestic point and, therefore, attributable to internal conversion; (4) a unique decay-associated spectrum at intermediate time scales (5.76 ps, DAS2.1), where the energy of the ESA can be assigned to a transition to $S_n(d)$; and (5) a second decay-associated spectrum at 321 ps (DAS3.1) that supports the interpretation of the isosbestic point as coming from an internal conversion between different excited electronic states, due to the absence of the $S_n(d)$ ESA at longer times. Corroborating this evidence are TD-DFT calculations that suggest a two-state model where

internal conversion between $S_3(d_{yz})$ and $S_1(d_{xy})$ is likely by orbital symmetry. Furthermore, they suggest a larger transition dipole of $S_3(d_{yz})$ to $S_n(d)$ than for $S_1(d_{xy})$, explaining why a 5.76 ps decay related to internal conversion can be isolated from the ESA. Lastly, the TD-DFT calculations for the different transition dipoles also show that an isosbestic point is viable.

Fig. 3.12 depicts the kinetic pathway that results from this internal conversion. The short time constant (142 fs) is attributed to rapid IVR/ISC from the initially excited state, $S_3^*(3d_{yz})$. Identifying the contributions to this fast decay by intersystem crossing and intra-/intervibrational relaxation is set aside for later experiments, as internal conversion is similarly possible from singlet or triplet states. After a combination of IVR and ISC within 0.142 ps, the initial wave packet excited by the pump relaxes to in a thermalized (geometry relaxed) $S_3(d_{yz})$ excited electronic state. Thereafter, the $S_3(d_{yz})$ population can transfer to the energetically nearby CT state provided by $S_1(3d_{xy})$. To this internal conversion, we assign the 5.76 ps ($\tau_1$) time constant. Finally, decay of $S_1(3d_{xy})$ to the ground state occurs with the last CT time scale associated with the DAS spectra, 321 ps ($\tau_2$).

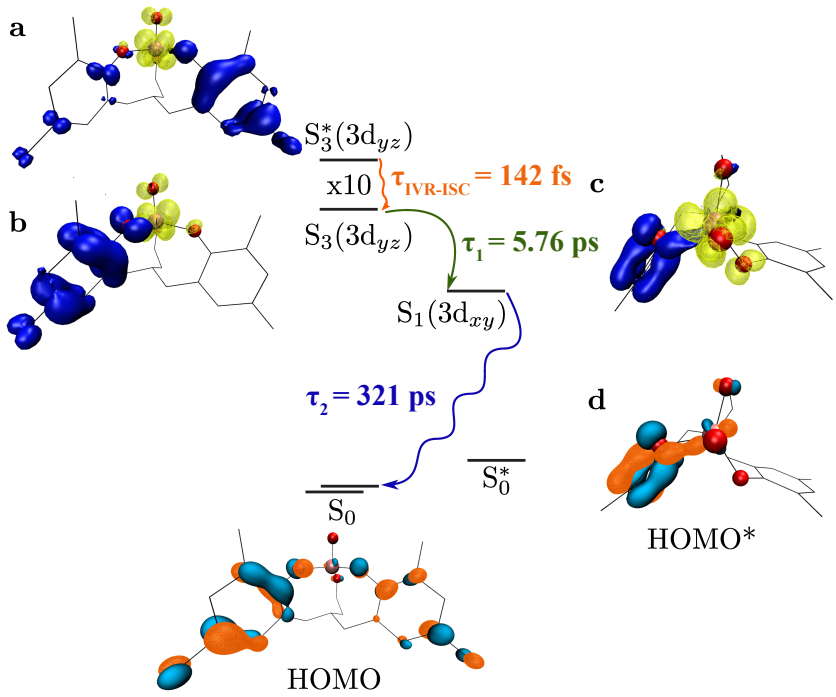


Figure 3.12: Scheme of relaxation pathways for excited VOL$^F$ with corresponding time constants determined from the DAS of the transient optical spectroscopy and excited and ground states depicted by TD-DFT. The relative energy differences are to scale, the one exception being $S_3^*(3d_{yz})$.

We now explore why internal conversion is an efficient pathway and why population of $S_1(3d_{xy})$ leads to such a long lifetime by TD-DFT and MS-CASPT2 calculations. In Fig. 3.12, the symmetries of the excited states are shown with electron occupation in yellow and hole occupation in blue. The electron occupation of the ground state, $S_0$, is shaded in blue/orange, denoting phase. In both $S_0$ and the initially excited $S_3^*(3d_{yz})$, electron occupation for $S_0$ and hole occupation for $S_3^*(3d_{yz})$ span both ligands, $\pi_+$ and $\pi_-$ orbitals (a). As $S_3^*(3d_{yz})$ moves along the potential energy surface the geometry is altered (b), and the hole is localized on $\pi_+$. At this point, $S_3(3d_{yz})$ has the right symmetry to internally convert to $S_1(3d_{xy})$ (c). For $S_1(3d_{xy})$, there is minimal electron weight on the bridging oxygen (i.e. vanadium-coordinating) to the $\pi_+$ ligand. To make this more clear, the molecule is shown from above for (c) and (d). The limited spatial overlap leads to weak coupling between $S_1(3d_{xy})$ and the distorted ground state, $S_0^*$, calculated at the geometry of $S_1(3d_{xy})$ and where the blue/orange indicate unoccupied electron density (d). Further, in this configuration, $S_0^*$ has unoccupied electron density on $\pi_+$ rather than distributed across both $\pi_+$ and $\pi_-$ (d). Together, the minimal electron weight on the bridging oxygen to $\pi_+$ and the $\pi_+$ occupation of $S_0^*$ leads to a very small transition dipole for $S_1(d_{xy}) \rightarrow S_0^*$ (Table 3.1), or $\sim 1$ % of the initially excited transition to $S_3^*(d_{yz})$). Furthermore, Franck-Condon overlap between low energy vibration modes of $S_1(3d_{xy})$ with the ground state is negligible ($< 10^{-8}$). While $S_0^*$ does lie higher in energy than $S_0$, the energy difference is small.

Given the significant distortions in the unoccupied density of $S_0^*$, with the weight on the $\pi_+$ orbital, one could ask whether or not the lifetime of the excited charge transfer state $S_3(3d_{yz})$, would also be long if the $S_1(3d_{xy})$ state was not available. While the TD-DFT and MS-CASPT2 indicate that the overlap of $S_1(3d_{xy})$ with the distorted ground state leads to a very small transition dipole, it is still significant for $S_3(3d_{yz})$. While the transition dipole between $S_3(3d_{yz})$ with the same distorted ground state is indeed reduced, it is still 10% of the initially excited transition to $S_3^*(d_{yz})$. ($S_3(3d_{yz})$ relaxes to a saddle point, thus we cannot assess Franck-Condon overlap). In conjunction with the absence of photoluminescence and identifiable triplet formation at longer time scales, this indicates that the electronic structure of $S_1(3d_{xy})$ is critical for the long charge transfer lifetime. In comparison to $S_3(3d_{yz})$, the electronic structure is primarily differentiated by the symmetry of electron occupied 3d orbital, since in both states the hole is localized on $\pi_+$ (Fig. 3.12).

### 3.5.2 Verifying the Kinetic Model

From initial measurements with excitation at 390 nm and our theoretical model of accessible excited states, a kinetic model was developed as described above. With careful choice of the monochromatic excitation wavelength, we investigated the possibility of selectively populating the $S_3(3d_{yz})$ (425 nm) and $S_1(3d_{xy})$ (480 nm) states as the initial prepared states and following their identical or variable trajectory as compared to the $S_3^*(3d_{yz})$ generated from 390 nm. Unusually, the observed kinetics did not show any dependence on the pump wavelength. Eigenkinetics and eigenspectra extracted from experiments at the various wavelengths in both solvents revealed nearly identical behavior; slight deviations were observed in

the early lifetimes. As expected, an isosbestic point was apparent after excitation at 425 nm, tracking the evolution of $S_3(3d_{yz}) \rightarrow S_1(3d_{xy})$. Incredibly, despite the low signal and pump scatter, the isosbestic was preserved under 480 nm excitation to $S_1(3d_{xy})$ as well. Given that transfer from the excited state $S_3(3d_{yz})$ to $S_1(3d_{xy})$ should not have been possible with initial population of the lowest excited state $S_1(3d_{xy})$, it seems likely that $S_3(3d_{yz})$ was dominantly excited. Furthermore, excitation at the lowest energy wavelength still yielded a lifetime on the order of hundreds of femtoseconds that, for higher energy excitation, we attributed to thermalization of electrons from the $S_3^*(3d_{yz})$ state. We examine two possible explanations.

The Franck-Condon broadening of each of the LMCT single particle transitions ($S_4$ through $S_1$) is unknown. Given that the calculated oscillator strength of the $S_1(3d_{xy})$ transition is orders of magnitude less than that of $S_3(3d_{yz})$ and $S_4$ (at their respective peaks), it is feasible that even at 480 (500-550) nm, the $S_3(3d_{yz})$ (or $S_2$) transition is preferentially excited. This suggests that the assignment of the fast kinetics at hundreds of femtoseconds to picoseconds is not thermalization but rather reflective of strong coupling and relaxation to the ground state. Alternatively, it may be that our theoretical estimate of the energy difference between $S_4$ and $S_3(3d_{yz})$ is minimal, and even residual $S_4$ is populated at the tail of the LMCT band.

Direct excitation of the LMCT band at or above the wavelength threshold for the $S_1$ transition does not confer the expected changes in our transient spectrum based on our excitation pathway. We are unable to make any positive statement about whether that excitation above the lowest transition is required for the long-lived component or at which point in time the necessary geometric distortion is achieved that provides the long lifetime. The full kinetic model that was developed on the 390 nm excitation alone cannot be confirmed due to an inability to selectively populate the $S_1$ transition and follow its excited state dynamics.

Solvent dependence may be explained by the reorganization of tetrahydrofuran to preserve a certain molecular geometry that results in the poor optical coupling and Franck-Condon overlap. Given the similarity in the early lifetimes, it seems reasonable to infer that intersystem crossing, if it does occur, would take place under both solvent conditions. Intersystem crossing rates in transition metal complexes have been shown to be fairly independent of solvent [66–68], which agrees with the hundreds of femtosecond lifetimes that are typically observed for ISC. Consequently, the discrepancy between the longer lifetimes seems likely a result of a excited state charge stabilization in polar and nonpolar media rather than the formation of a triplet state in one solvent versus another. While there is no positive experimental evidence of $VOL^F$ in the triplet state, the possibility of intersystem crossing contributing to the long lifetime that was observed under both solvent conditions and all excitation wavelengths cannot be ruled out.

Despite the resolution of our ultrafast system, it remains difficult to attribute early time scales to specific process(es) in transition metal complexes that can occur in under tens of femtoseconds and are convolved with additional signals and transient artifacts. Fluorescence upconversion is an ultrafast technique that is currently employed to distinguish between fluorescence from ground-state bleach contributions with energy dependence of the conversion

efficiency acting as signal gate. These additional upconversion experiments on the oxovanadium complex are proposed to elucidate the origin of the short lifetime in our relaxation pathway.

## 3.6 Conclusion

Following internal conversion from an initially excited state to a nearby charge transfer state, $S_1(3d_{xy})$, a long-lived (321 ps) LMCT state is observed in a 3d metal-centered compound, $VOL^F$. In conjunction with no observed photoluminescence, theoretical calculations indicate very poor optical and vibrational overlap of the thermalized charge transfer state $S_1$ to the distorted ground state. The long lifetime of the $S_1(3d_{xy})$ is attributed to its relaxation through non-radiative transition with little opportunity to release its energy to vibrations. The results obtained here represent one of the first few studies on the photophysics of a ligand-to-metal charge transfer complex, and one of the longest-lived excited states in a first row transition metal to be observed without a confirmed triplet state. Future work will investigate the universality of this type of long-lived charge transfer in 3d metal-centered compounds by transient absorption and TD-DFT, along with uses for $VOL^F$ and related compounds containing $d^0$ LMCT transitions for driving photochemical reactions.

# References


(1) Gasser, G.; Metzler-Nolte, N. The Potential of Organometallic Complexes in Medicinal Chemistry. *Current Opinion in Chemical Biology* **2012**, *16*, 84–91.

(2) Thorp-Greenwood, F. An Introduction to Organometallic Complexes in Fluorescence Cell Imaging: Current Applications and Future Prospects. *Organometallics* **2012**, *31*, 5686–5692.

(3) Crabtree, R. H., *The Organometallic Chemistry of the Transition Metals*; John Wiley & Sons: 2009.

(4) Crabtree, R. H. An Organometallic Future in Green and Energy Chemistry? *Organometallics* **2011**, *30*, 17–19.

(5) Geoggroy, G., *Organometallic Photochemistry*; Elsevier: 2012.

(6) Daul, C. A.; Gu, H. U. Excited-State Energies and Distortions of $d^0$ Transition Metal Tetraoxo Complexes : A Density Functional Study. *Journal of Chemical Physics* **1997**, *107*, 4606–4617.

(7) Pollagi, T. P.; Stoner, T. C.; Dallinger, R. F.; Gilbert, T. M.; Hopkins, M. D. Nonlinear Optical and Excited-State Properties of Conjugated, One-Dimensional $[N{\equiv}M(OR)_3]_n$ Polymers. *Journal of the American Chemical Society* **1991**, *113*, 703–704.

(8) Da Re, R. E.; Hopkins, M. D. Electronic Spectroscopy And Photophysics Of Metal-Alkylidyne Complexes. *Coordination Chemistry Reviews* **July 2005**, *249*, 1396–1409.

(9) Vogler, A.; Kunkely, H. Photochemistry of Peroxo Complexes Induced by LMCT, MLCT and Peroxide IL/LLCT Excitation. *Coordination Chemistry Reviews* **July 2006**, *250*, 1622–1626.

(10) Caspar, J. V.; Westmoreland, T. D.; Allen, G. H.; Bradley, P. G.; Meyer, T. J.; Woodruff, W. H. Molecular and Electronic Structure in the Metal-to-Ligand Charge-Transfer Excited States of $d^6$ Transition-Metal Complexes in Solution. *Journal of the American Chemical Society* **1984**, *106*, 3492–3500.

(11) Huynh, M. H. V.; Dattelbaum, D. M.; Meyer, T. J. Exited State Electron and Energy Transfer in Molecular Assemblies. *Coordination Chemistry Reviews* **Feb. 2005**, *249*, 457–483.

(12) Furue, M.; Maruyamaa, K.; Kanematsub, Y.; Kushiiab, T.; Kamachii, M. Competitive Energy and Electron-Transfer Quenching in lntramolscular Processes of Excited Polypyridine Ruthenium(ll)/Osmium(ll) Binuclear Complexes M. *Coordination Chemistry Reviews* **1994**, *132*, 201–208.

(13) Huse, N.; Kim, T.; Jamula, L.; McCusker, J.; de Groot, F.; Schoenlein, R. Photo-Induced Spin-State Conversion in Solvated Transition Metal Complexes Probed via Time-Resolved Soft X-ray Spectroscopy. *Journal of the American Chemical Society* **2010**, *132*, 6809–6816.

(14) Juris, A.; Balzani, V.; Barigelletti, F.; Campagna, S.; Belser, P.; von Zelewsky, A. Ru(II) Polypyridine Complexes: Photophysics, Photochemistry, Electrochemistry, and Chemiluminescence. *Coordination Chemistry Reviews* **1988**, *84*, 85–277.

(15) McCusker, J. K. Femtosecond Absorption Spectroscopy of Transition Metal Charge-Transfer Complexes. *Accounts of Chemical Research* **2003**, *36*, 876–887.

(16) Grätzel, M. Solar Energy Conversion by Dye-Sensitized Photovoltaic Cells. *Inorganic Chemistry* **2005**, *44*, 6841–6851.

(17) Samia, A. C. S.; Cody, J.; Fahrni, C. J.; Burda, C. The Effect of Ligand Constraints on the Metal-To-Ligand Charge-Tranfer Relaxation Dynamics of Copper (I) - Phenanthroline Complexes : A Comparative Study by Femtosecond Time-Resolved Spectroscopy. *Journal of Physical Chemistry B* **2004**, *108*, 563–569.

(18) McCusker, C. E.; Castellano, F. N. Orange-to-Blue and Red-to-Green Photon Upconversion with a Broadband Absorbing Copper(I) MLCT Sensitizer. *Chemical Communications* **2013**, *49*, 3537–9.

(19) Chen, L. X.; Shaw, G. B.; Novozhilova, I.; Liu, T.; Jennings, G.; Attenkofer, K.; Meyer, G. J.; Coppens, P. MLCT State Structure and Dynamics of a Copper(I) Diimine Complex Characterized by Pump-Probe X-ray and Laser Spectroscopies and DFT Calculations. *Journal of the American Chemical Society* **2003**, *125*, 7022–7034.

(20) Penfold, T.; Karlsson, S.; Capano, G.; Lima, F.; Rittmann, J.; Reinhard, M.; Rittmann-Frank, M.; Braem, O.; Baranoff, E.; Abela, R.; Tavernelli, I.; Rothlisberger, U.; Milne, C.; Chergui, M. Solvent-Induced Luminescence Quenching: Static and Time-Resolved X-Ray Absorption Spectroscopy of a Copper (I) Phenanthroline Complex. *Journal Physical Chemistry A* **2013**, *117*, 4591–4601.

(21) Zhang, W. et al. Tracking Excited State Charge and Spin Dynamics in Iron Coordination Complexes. *Nature* **2014**, *509*, 345–348.

(22) Harlang, T. C.; Liu, Y.; Gordivska, O.; Fredin, L. A.; Ponseca Jr, C. S.; Huang, P.; Chábera, P.; Kjaer, K. S.; Mateos, H.; Uhlig, J. *et al.* Iron Sensitizer Converts Light to Electrons with 92% Yield. *Nature Chemistry* **2015**, *7*, 883–889.

(23) Van Kuiken, B. E.; Cho, H.; Hong, K.; Khalil, M.; Schoenlein, R. W.; Kim, T. K.; Huse, N. Time-Resolved X-ray Spectroscopy in the Water Window: Elucidating Transient Valence Charge Distributions in an Aqueous Fe (II) Complex. *Journal of Physical Chemistry Letters* **2016**.

(24) McCusker, J. K.; Rheingold, A. L.; Hendrickson, D. N. Variable-Temperature Studies of Laser-Intiated $^5T_2 \rightarrow {}^1A_1$ Intersystem Crossing in Spin-Crossover Complexes: Empirical Correlations Between Activation Parameters and Ligand Structure in a Series of Polypyridyl Ferrous Complexes. *Inorganic Chemistry* **1996**, *35*, 2100–2112.

(25) Bressler, C.; Milne, C.; Pham, V.-T.; ElNahhas, A.; Van der Veen, R.; Gawelda, W.; Johnson, S.; Beaud, P.; Grolimund, D.; Kaiser, M., et al. Femtosecond XANES Study of the Light-Induced Spin Crossover Dynamics in an Iron (II) Complex. *Science* **2009**, *323*, 489–492.

(26) Gütlich, P.; Hauser, A. Thermal and Light-Induced Spin Crossover in Iron (II) Complexes. *Coordination Chemistry Reviews* **1990**, *97*, 1–22.

(27) Monat, J. E.; McCusker, J. K. Femtosecond Excited-State Dynamics of an Iron (II) Polypyridyl Solar Cell Sensitizer Model. *Journal of the American Chemical Society* **2000**, *122*, 4092–4097.

(28) Juban, E. A.; Smeigh, A. L.; Monat, J. E.; McCusker, J. K. Ultrafast Dynamics of Ligand-Field Excited States. *Coordination Chemistry Reviews* **2006**, *250*, 1783–1791.

(29) Liu, Y.; Harlang, T.; Canton, S. E.; Chábera, P.; Suárez-Alcántara, K.; Fleckhaus, A.; Vithanage, D. A.; Göransson, E.; Corani, A.; Lomoth, R., et al. Towards Longer-Lived Metal-to-Ligand Charge Transfer States of Iron (II) Complexes: an N-Heterocyclic Carbene Approach. *Chemical Communications* **2013**, *49*, 6412–6414.

(30) Fredin, L. A.; Pápai, M.; Rozsállyi, E.; Vankó, G.; Wärnmark, K.; Sundström, V.; Persson, P. Exceptional Excited-State Lifetime of an Iron (II)–N-Heterocyclic Carbene Complex Explained. *Journal of Physical Chemistry Letters* **2014**, *5*, 2066–2071.

(31) Armaroli, N.; Accorsi, G.; Cardinali, F.; Listorti, A. Photochemistry and Photophysics of Coordination Compounds: Copper. *Topics in Current Chemistry* **2007**, *280*, 69–115.

(32) Choing, S. N.; Francis, A. J.; Clendenning, G.; Schuurman, M. S.; Sommer, R. D.; Tamblyn, I.; Weare, W. W.; Cuk, T. Long-Lived LMCT in a $d^0$ Vanadium (V) Complex by Internal Conversion to a State of $3d_{xy}$ Character. *Journal of Physical Chemistry C* **2015**, *119*, 17029–17038.

(33) Bartelmess, J.; Francis, A.; El Roz, K.; Castellano, F.; Weare, W.; Sommer, R. Light-Driven Hydrogen Evolution by BODIPY Sensitized Cobaloxime Catalysts. *Inorganic Chemistry* **2014**, *53*, 4527–4534.

(34) Connelly, N.; Geiger, W. Chemical Redox Agents in Organometallic Chemistry. *Chemical Reviews* **1996**, *96*, 877–910.

(35) Frisch, M. J. and Trucks, G. W. and Schlegel, H. B. and Scuseria, G. E. and Robb, M. A. and Cheeseman, J. R. and Scalmani, G. and Barone, V. and Mennucci, B. and Petersson, G. A. et al., Gaussian 09, Revision A.02, Gaussian, Inc., Wallingford, CT, 2009.

(36) Shao, Y. et al. Advances in Methods and Algorithms in a Modern Quantum Chemistry Program Package. *Physical Chemistry Chemical Physics* **2006**, 3172.

(37) Heyd, J.; Scuseria, G. E.; Ernzerhof, M. Hybrid Functionals Based on a Screened Coulomb Potential. *Journal of Chemical Physics* **2003**, *118*, 8207–8215.

(38) Becke, A. D. Density-Functional Thermochemistry. III. The Role of Exact Exchange. *Journal of Chemical Physics* **1993**, *98*, 5648–5652.

(39) Lee, C.; Yang, W.; Parr, R. G. Development of the Colle-Salvetti Correlation-Energy Formula into a Functional of the Electron Density. *Physical Review B* **Jan. 1988**, *37*, 785–789.

(40) Hay, P. J.; Wadt, W. R. Ab Initio Effective Core Potentials for Molecular Calculations. Potentials for K to Au Including the Outermost Core Orbitals. *Journal of Chemical Physics* **1985**, *82*, 299–310.

(41) Stout, E.; Politzer, P. An Investigation of Definitions of the Charge on an Atom in a Molecule. *Theoretica Chimica Acta* **1968**, *12*, 379–386.

(42) Ros, P.; Schuit, G. C. A. Molecular Orbital Calculations on Copper Chloride Complexes. *Theoretica Chimica Acta (Berlin)* **1966**, *4*, 1–12.

(43) Brydson, R.; Sauer, H.; Engel, W.; Thomass, J.; Zeitler, E.; Kosugi, N.; Kuroda, H. Electron Energy Loss and X-Ray Absorption Spectroscopy of Rutile and Anatase: A Test of Structural Sensitivity. *Journal of Physics: Condensed Matter* **1989**, *1*, 797.

(44) De Groot, F.; Grioni, M.; Fuggle, J.; Ghijsen, J.; Sawatzky, G.; Petersen, H. Oxygen 1s X-Ray-Absorption Edges of Transition-Metal Oxides. *Physical Review B* **1989**, *40*, 5715.

(45) Van Aken, P.; Liebscher, B.; Styrsa, V. Core Level Electron Energy-Loss Spectra of Minerals: Pre-Edge Fine Structures at the Oxygen K-Edge. *Physics and Chemistry of Minerals* **1998**, *25*, 494–498.

(46) Minasian, S. G.; Keith, J. M.; Batista, E. R.; Boland, K. S.; Bradley, J. A.; Daly, S. R.; Kozimor, S. A.; Lukens, W. W.; Martin, R. L.; Nordlund, D., et al. Covalency in Metal–Oxygen Multiple Bonds Evaluated Using Oxygen K-edge Spectroscopy and Electronic Structure Theory. *Journal of the American Chemical Society* **2013**, *135*, 1864–1871.

(47) Brydson, R.; Garvie, L.; Cravens, A.; Sauer, H.; Hofer, F.; Cressey, G. $L_{2,3}$ Edges of Tetrahedrally Coordinated $d^0$ Transition-Metal Oxyanions $XO_4^{n-}$. *Journal of Physics: Condensed Matter* **1993**, *5*, 9379–9392.

(48) Seena, E.; Mathew, N.; Kuriakose, M.; Kurup, M. Synthesis, Spectral and EPR Studies of Oxovanadium (IV) Complexes Incorporating Tridentate ONO Donor Hydrazine Ligands: Structural Study of One Oxovanadium (V) Complex. *Polyhedron* **2008**, *27*, 1455–1462.

(49) Ortolano, T.; Selbin, J.; McGlynn, S. Electronic Structure, Spectra, and Magnetic Properties of Oxycations. V. the Electronic Spectra of Some Vanadyl Complexes. *Journal of Chemical Physics* **1964**, *41*, 262–268.

(50) Kuska, H.; Rogers, M. Assignment of Optical Spectra for Vanadyl Complexes. *Inorganic Chemistry* **1965**, *5*, 313–315.

(51) Boucher, L.; Tynan, E.; Yen, T. Spectral Properties of Oxovanadium (IV) Complexes. I. $\beta$-Ketimines. *Inorganic Chemistry* **1967**, *7*, 731–736.

(52) Ferrer, E.; Baran, E. Electronic and Photoelectron Spectra of Vanadyl (IV) Tetraphenylporphyrin. *Journal of Electron Spectroscopy* **1991**, *57*, 189–197.

(53) Song, L.; Fayer, M. Temperature Dependent Intersystem Crossing and Triplet-Triplet Absorption of Rubrene in Solid Solution. *Journal of Luminescence* **1991**, *50*, 75–81.

(54) Han, Y.; Spangler, L. Use of Isosbestic Points for Determination of Quantum Efficiency in Transient Absorption Spectroscopy. *Journal of Physical Chemistry A* **2002**, *106*, 1701–1707.

(55) Kuciauskas, D.; Monat, J. E.; Villahermosa, R.; Gray, H. B.; Lewis, N. S.; McCusker, J. K. Transient Absorption Spectroscopy of Ruthenium and Osmium Polypyridyl Complexes Adsorbed onto Nanocrystalline $TiO_2$ Photoelectrodes. *Journal of Physical Chemistry B* **2002**, *106*, 9347–9358.

(56) Einterz, C.; Lewis, J.; Kliger, D. Spectral and Kinetic Evidence for the Existence of Two Forms of Bathorhodopsin. *Proceedings of the National Academy of Sciences U.S.A.* **1987**, *84*, 3699–3703.

(57) Gawelda, W.; Cannizzo, A.; Pham, V.-T.; Van Mourik, F.; Bressler, C.; Chergui, M. Ultrafast Nonadiabatic Dynamics of $[Fe^{II}(bpy)_3]^{2+}$ in Solution. *Journal of the American Chemical Society* **2007**, *129*, 8199–8206.

(58) Iwamura, M.; Takeuchi, S.; Tahara, T. Real-Time Observation of the Photoinduced Structural Change of Bis(2,9-Dimethyl-1,10-Phenanthroline)Copper(I) by Femtosecond Fluorescence Spectroscopy: A Realistic Potential Curve of the Jahn-Teller Distortion. *Journal of the American Chemical Society* **2007**, *129*, 5248–5256.

(59) Damrauer, N. H.; Cerullo, G.; Yeh, A.; Boussie, T. R.; Shank, C. V.; McCusker, J. K. Femtosecond Dynamics of Excited-State Evolution in $[Ru(bpy)_3]^{2+}$. *Science* **1997**, *275*, 54–57.

(60) McCusker, J. K.; Walda, K. N.; Dunn, R. C.; Simon, J. D.; Magde, D.; Hendrickson, D. N. Subpicosecond $^1$MLCT $\rightarrow$ $^5T_2$ Intersystem Crossing of Low-Spin Polypyridyl Ferrous Complexes. *Journal of the American Chemical Society* **1993**, *115*, 298–307.

(61) Aubard, J.; Maurel, F.; Buntinx, G.; Poizat, O.; Levi, G.; Guglielmetti, R.; Samat, A. Femto/Picosecond Transient Absorption Spectroscopy of Photochromic 3,3-Diphenylnaphtho[2,1-b]pyran. *Molecular Crystals and Liquid Crystals* **2000**, *345*, 215–220.

(62) Martin, M.; Plaza, P.; Meyer, Y.; Bégin, L.; Bourson, J.; Valeur, B. A New Concept of Photogeneration of Cations: Evidence for Photoejection of $Ca^{2+}$ and $Li^{+}$ from Complexes with a Crown-Ether-Linked Merocyanine by Picosecond Spectroscopy. *Journal of Fluorescence* **1994**, *4*, 271–273.

(63) Kwok, W.; Ma, C.; Phillips, D.; Matousek, P.; Parker, A.; Towrie, M. Picosecond Time-Resolved Study of 4-Dimethylaminobenzonitrile in Polar and Nonpolar Solvents. *Journal of Physical Chemistry A* **2000**, *104*, 4188–4197.

(64) Fenske, R. F. Intensities of Forbidden Transitions in Octahedral Complexes. *Journal of the American Chemical Society* **1967**, *89*, 252–256.

(65) Zink, J. I. Photo-Induced Metal-Ligand Bond Weakening, Potential Surfaces, and Spectra. *Coordination Chemistry Reviews* **2001**, *211*, 69–96.

(66) Dose, E. V.; Hoselton, M. A.; Sutin, N.; Tweedle, M. F.; Wilson, L. J. Dynamics of Intersystem Crossing Processes in Solution for Six-Coordinate $d^5$, $d^6$, and $d^7$ Spin-Equilibrium Metal Complexes of Iron (III), Iron (II), and Cobalt (II). *Journal of the American Chemical Society* **1978**, *100*, 1141–1147.

(67) Koster, G.; Kropman, B. L.; Rijnders, G. J.; Blank, D. H.; Rogalla, H. Quasi-Ideal Strontium Titanate Crystal Surfaces Through Formation of Strontium Hydroxide. *Applied Physics Letters* **1998**, *73*, 2920–2922.

(68) Forster, L. S. Intersystem Crossing in Transition Metal Complexes. *Coordination Chemistry Reviews* **2006**, *250*, 2023–2033.

# Chapter 4

# Formation Dynamics of Multiple Hole Species on Niobium-Doped Strontium Titanate

## 4.1 Abstract

Surface sensitive transient optical reflectance spectroscopy of an n-doped strontium titanate single crystal (001) reveals multiple surface hole midgap states, one of which can be correlated to a water oxidation intermediate previously observed in the far-infrared. In prior studies, two hole species were separately identified at 800 nm and 800 $cm^{-1}$, corresponding to valence band holes and a titanium-oxyl radical (Ti-O*), respectively. The transient reflectance response of $SrTiO_3$ is examined using sub-band gap probe light (400 nm, 450-700 nm) to map the formation dynamics of coexisting radical species. In the 400 nm kinetics, two distinct surface hole states are revealed, with both displaying in-plane transition dipole moments. The formation rate of the first hole state was found to mirror the early time dynamics for the formation of a Ti-O*-induced vibration at 800 $cm^{-1}$ as well as vibrational relaxation dynamics in bulk and interfacial water. The signature was generally ascribed to an oxyl radical (Ti-O*), though contributions from other surface-localized radical species, such as a lateral hole (Ti-O*-Ti), were not discounted from consideration. The second surface hole species was found only to appear following a delay time (4 ps) and a much longer formation time (36 ps) than was observed for the first radical species. The delay time was taken to represent necessary surface rearrangement—e.g., solvent reorganization and lattice thermalization—following the localization of the first hole in its final state. Based upon the significant duration of the time between the formation of the first radical and the second hole species and the preceding surface rearrangement, the second species was attributed to a distorted surface-trapped hole with a distinct but undetermined molecular form. With a white light continuum probe, three distinct holes are identified as arising out of the excess photogenerated holes within the depletion region. Singular value decomposition of the broadband data is carried out

to elucidate these hole states' contributions to the monochromatic and broadband white light kinetics under a number of reaction conditions, specifically voltage. Under negative bias, the dominant hole species observed in the broadband spectrum is attributed to valence band holes; conversely, under positive applied bias, the white light transient response reveals major contributions from the two hole species that were observed in the 400 nm kinetics. The population distribution of these three hole species at the interface depends strongly on voltage conditions ($k_{WLC}(V)$), with direct competition between the two radical states ($k_1$, $k_2$) for surface sites. Furthermore, the number of available surface-sites appears to be heavily influenced by current density.

## 4.2 Introduction

The mechanism for water oxidation on solid-state transition metal oxide photocatalysts is a topic of extreme interest for optimizing artificial photosynthetic systems. Unfortunately, a precise description of the mechanistic pathway has long eluded researchers. In addition to the complexity of identifying metal oxidation states and their corresponding coordination environments following photoexcitation, further difficulty arises in determining the molecular intermediates that subsequently form at the solid-liquid interface. The difficulty in doing so derives from the fact that the creation of oxygen gas requires the transfer of four holes. Several research groups have investigated various systems in order to determine the individual reaction steps of the multistep process. [1–3] A clear understanding of the mechanism, however, requires the ability to distinguish the individual hole transfer steps and the resultant intermediates from the preceding and succeeding charge transfers. Notably, previous studies in n-doped titanium dioxide and iron oxide *in situ* have reported a range of timescales spanning several orders of magnitude for the first hole transfer of the oxidation mechanism. [2, 4–6] The breadth of timescales over which the first hole transfer is observed is likely attributable to the low quantum efficiency of these systems, [2, 7] indicating competitive decay channels to the overall oxygen evolution process. With charge recombination as a competing pathway to the water oxidation mechanism, there may be insufficient concentrations of the appropriate water oxidation intermediate(s) to detect signal or extract signal from that of other synchronous species.

In transient reflectance measurements previously undertaken by our group, specific efforts were made to tailor the wavelengths and geometry of the experimental setup to a niobium-doped (0.1 wt. %) strontium titanate (n-$SrTiO_3$) single crystal such that the depletion width (25 nm) would match the excitation and interrogation depths (Figures 4.1a and b, and 4.2a). [8] Under matching conditions, the electric field created by interfacial band bending under *in situ* conditions reduces carrier recombination by driving electrons into the bulk and allows for complete drift of photogenerated holes to the interface. Therefore, all signals recorded *in situ* using this geometry can be attributed to holes and their dynamics. In this particular experimental configuration, as shown in Fig. 4.1b, quantum yields up to 70% under 266 nm illumination could be achieved based on photocurrent measurements (Fig. 4.2b), further

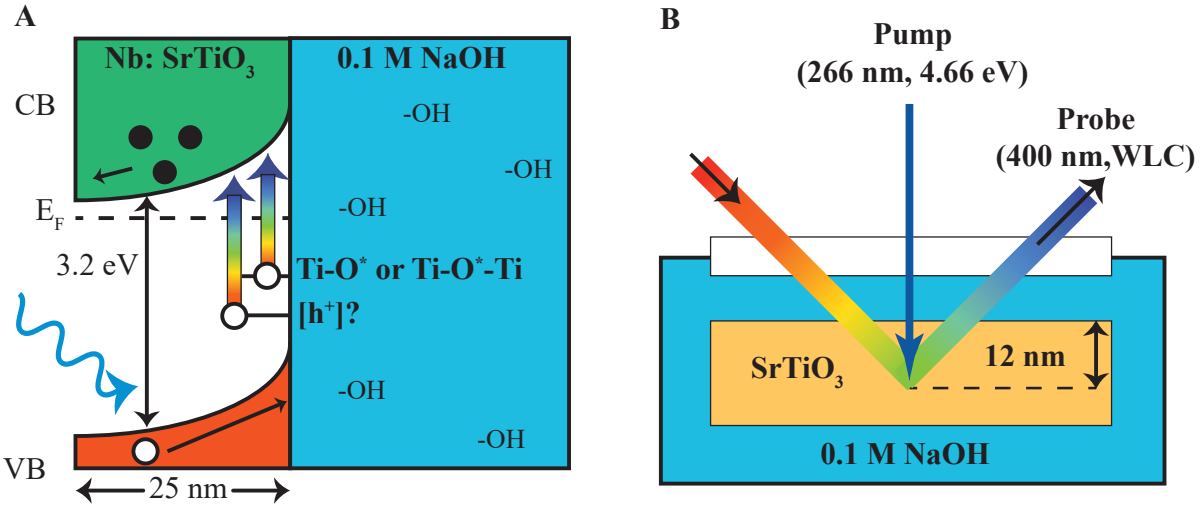


Figure 4.1: (a) Schematic of the interface of n-$SrTiO_3$ and water. Charge equilibration induces band bending over the first 25 nm. Under a UV pulse at or above band gap (3.2 eV), photogenerated electrons are swept into the bulk and holes towards the solid-liquid interface. Ti-O* and Ti-O*-Ti are two possible hole species created at the surface, though others ($h^+$) may occur. (b) In the transient reflectance geometry, the pump and probe depths are equal to or less than the $SrTiO_3$ depletion width (25 nm). The pump pulse employed here is well above the band gap (266 nm, 4.66 eV) to match the interrogation depth of optical probes at 400 nm and 450-700 nm (white light continuum, WLC). Sub-band gap transitions to the conduction band probed by the 400 nm and WLC are shown in panel (a).

indicating that a large number of holes are produced and reach the surface. The high incident photon-to-current conversion efficiency of strontium titanate makes the system an ideal choice for examining both electronic relaxation pathways and the formation of molecular bonds under ultrafast time-resolved techniques.

As a model perovskite, strontium titanate has a cubic structure of interleaved rock salt crystals SrO and $TiO_2$, shown in Fig. 4.3. As has been observed in studies of titanium dioxide, the exposed crystal face and surface preparation can have a significant effect on the observed kinetics and thermodynamics of water oxidation. [9] Although many facets of strontium titanate, like those of titanium dioxide, have shown catalytic activity, [1, 10] the focus of this study is limited to the $SrTiO_3$ (001) surface. The (001) crystal face of $SrTiO_3$ comprises alternating layers of titanium dioxide and strontium oxide. $SrTiO_3$ can be doped as p-type (e.g. $Fe^{3+}$) and n-type (e.g. $Nb^{5+}$) through substitutional replacement of native titanium ($Ti^{4+}$) atoms, thereby providing large gains in conductivity. [11] Upon the introduction of niobium dopants, the material changes its appearance from a white, translucent crystal to a dark, glossy black crystal. Other defect, or midgap, states such as oxygen vacancies can contribute to the electronic properties of $SrTiO_3$ as well. [12–14]

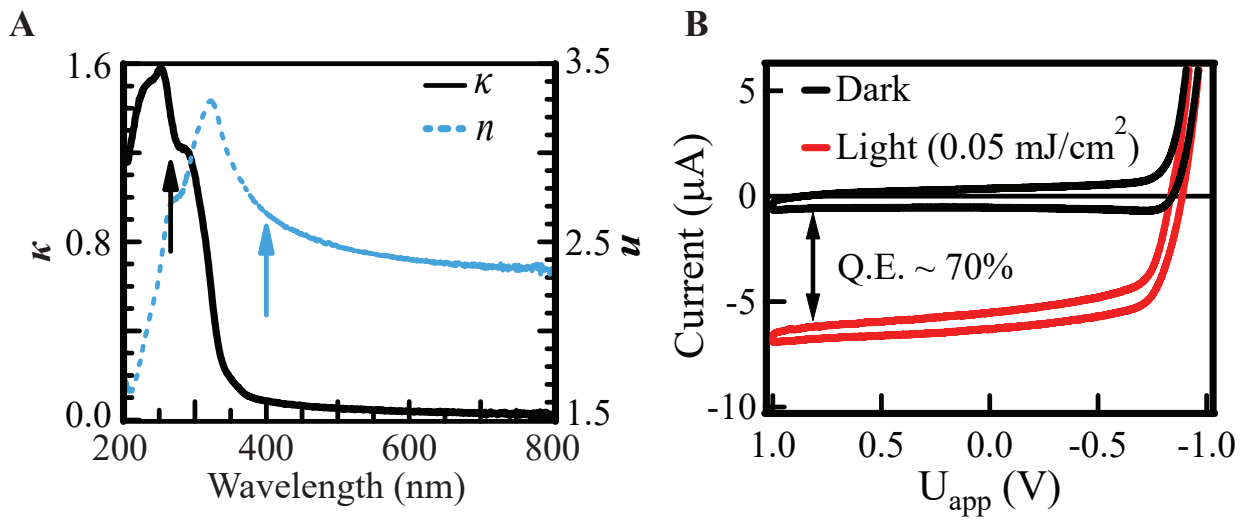


Figure 4.2: (a) Ellipsometry measurement of $SrTiO_3$, showing the refractive index $n$ and extinction coefficient $\kappa$ at the monochromatic pump (266 nm) and probe (400 nm) wavelengths. (b) Comparison of cyclic voltammograms of $SrTiO_3$ in the dark and under laser light.

In this chapter, transient optical absorption measurements were undertaken to investigate the possibility of coexistent radical hole species at the solid-liquid interface of Nb-doped $SrTiO_3$. Due to the importance of distinguishing contributions from multiple hole states to the strontium titanate water oxidation mechanism, the general probes of monochromatic 400 nm and broadband (450-700 nm) white light were used to track sub-band gap ($\lambda$ >355 nm) transitions—some of which are shown in Fig. 4.1a—for which the midgap states of radical species are expected to contribute. Additionally, the use of a broadband spectral probe enables measurement of the time dynamics of many possible hole species simultaneously. Two principal radical species were distinguished based on their unique experimental behavior in the 400 nm kinetics. One hole species was observed to form within the first 1.25 ps following excitation; both oxyl radical (Ti-O*) and lateral (Ti-O*-Ti) holes were considered as candidates for this initial state. The observed time constant was confirmed as reflecting the formation of the titanium-oxyl (Ti-O*) radical species, based upon an identical rise time observed for a subsurface vibration induced by the titanium-oxyl radical in the far-infrared. However, the formation of lateral holes within the timescale of this early 1.25 ps rise signal could not be eliminated; indeed, theoretical calculations strongly suggest possible contributions to the signal arising from a lateral hole. A second hole species with an unidentified molecular form was observed to appear following a 4 ps delay and a substantial rise time (36 ps). The preceding delay was assigned to surface rearrangement—thermalization of the surrounding electrolyte and hydrogen bonding network—that was likely induced by the

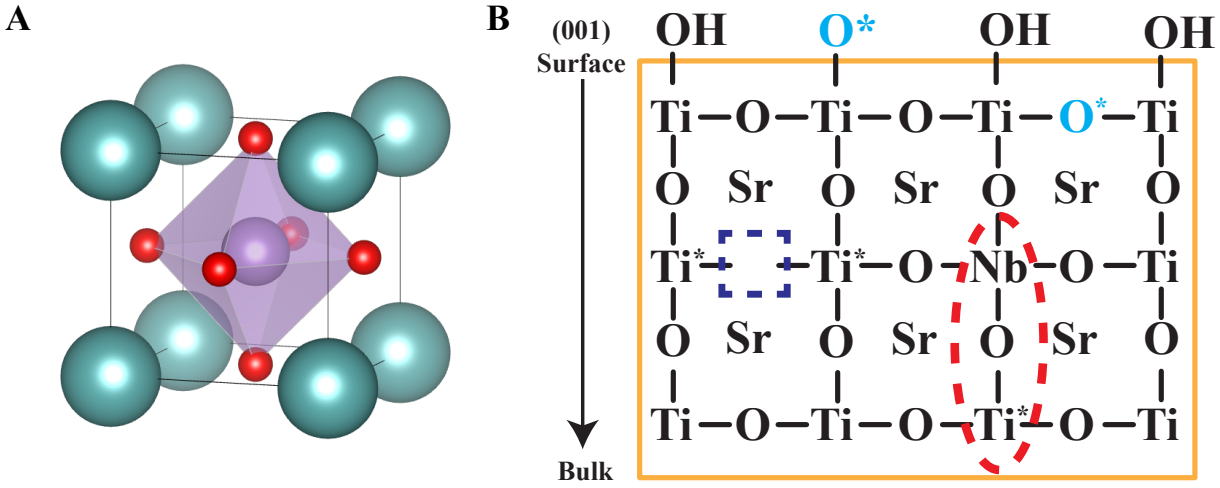


Figure 4.3: (a) Crystal structure of n-doped strontium titanate, n-$SrTiO_3$. Strontium titanate is a cubic perovskite with two overlapping rock salt structures. (b) Niobium ($Nb^{5+}$ atoms act as substitutional donors, replacing $Ti^{4+}$ atoms in the lattice (red). Oxygen vacancies (purple) are a common defect state, producing excess charge carriers. Oxyl radicals and lateral holes (blue) are two species implicated in the water oxidation mechanism. [1]

localization of the first surface hole. A supercontinuum probe was also employed to examine the behavior of these radical hole species under various reaction conditions. In the broadband measurements, an additional valence band hole signature was distinguished from the two radical species of the monochromatic traces. It was determined that, while the formation dynamics of these two radical hole species remained unchanged, the overall distribution of holes in the valence band and the two radical states was highly sensitive to voltage. In addition, the number of accessible surface-sites strongly depended on photocurrent.

## 4.3 Experimental Methods

### 4.3.1 Sample Preparation

Single crystalline samples of (001) niobium-doped n-type strontium titanate (n-$SrTiO_3$) (0.1 wt. % Nb) were purchased from MTI Corp (Richmond, CA). Samples were received as polished on both surfaces; to improve electrical contact, one side was roughened manually with sandpaper. Given that ultraviolet irradiation has previously shown the formation of oxygen vacancies [15] and electrochemical treatment (+0.8 V vs. Ag/AgCl) has been implicated in surface rearrangement [16], all $SrTiO_3$ samples were subjected to ultraviolet irradiation at 266 nm and an applied bias of +0.5 V for 15 minutes to establish a stable (roughened)

surface prior to acquisition of transient reflectance data. To characterize the surface of strontium titanate following transient measurements, both low energy electron diffraction (LEED) patterns and scanning electron microscopy (SEM) images were acquired for pristine and roughened samples. Inductively-coupled plasma atomic emission spectra (ICP-AES) were also collected on the electrolyte solutions before and after catalysis to quantify loss of surface material as a result of photoelectrochemical treatment. The effect of the surface roughening procedure on our ability to distinguish discrete molecular radicals at the interface is discussed below and, ultimately, found to be negligible.

### 4.3.2 Electrochemistry

A three-electrode setup incorporated into a homemade teflon electrochemical cell and a potentiostat from CH Instruments (CHI 1400B, Austin, TX) were used for all electrochemical measurements and transient absorption experiments. Platinum wire was employed as a counter electrode; a Ag/AgCl electrode in 3 M KCl (MF-2052, Basi, West Lafayette, IN) was used as a reference (0.20 V vs. normal hydrogen electrode). For the working electrode, ohmic contact was obtained by securing a copper wire to the unpolished backside of the n-$SrTiO_3$ sample with silver paste (Electron Microscopy Sciences, Hatfield, PA) or with indium-gallium eutectic; the choice of contact had a negligible effect in our electrochemical measurements. An insulating lacquer (Miccrostop, Tolber Chemical Division, Hope, Arkansas) was applied to all surfaces except the front polished side of the n-$SrTiO_3$ crystal. Prior to conducting transient absorption experiments, each sample was tested for carrier concentration (Mott-Schottky measurements). In addition, before each pump-probe experiment, cyclic voltammograms were taken of each sample in the dark and under illumination by laser pulse to determine photocurrent and ensure good electrical contact within the setup. The open circuit kinetics were collected prior to and following the roughening procedure, described above, at the probe wavelength(s) being examined.

### 4.3.3 Transient Absorption Measurements

Transient optical absorption measurements were conducted in the same homemade teflon electrochemical cell, with the exception of fluence dependence measurements in air. The cell was designed to hold a transparent window for transient reflectance measurements *in situ*. An uncoated calcium fluoride flat was chosen as the window to enclose electrolyte solution in the electrochemical cell while allowing transmission of both ultraviolet pump and visible probe pulses.

Both the excitation and probe pulses were derived from a regeneratively amplified Ti: Sapphire laser (Legend Elite HE, Coherent, Santa Clara, CA) with an output of 150 fs pulses centered at 800 nm at a repetition rate of 1 kHz. In order to generate the necessary photon energy to excite strontium titanate above its band gap—3.25 eV (indirect) [12, 17–19], the fundamental beam was directed into a series of type I birefringent $\beta$-barium borate (BBO) crystals (Eksma Optics, FK-800-200-M, Vilnius, Lithuania) for third harmonic generation to

produce 266 nm (4.66 eV) light. Residual 400 nm and 800 nm light were removed by a Pellin-Broca prism and high reflector harmonic separator (CVI Melles Griot, Rochester, NY). A small fraction of the 800 nm pulse was used to generate probe light at 400 nm (3.1 eV) by focusing the fundamental into a BBO cut for second harmonic generation (0.5 mm thick, 29°). The broadband white light continuum probe, extending from 450-700 nm, was created by focusing approximately 3 $\mu$J of 800 nm light into a sapphire plate. Reflected probe light was directed into a fiber optic cable coupled to a Ultrafast Systems visible light detection module (Sarasota, FL). The Ultrafast Systems detection module was triggered with a TTL pulse derived from the signal delay generator of the regenerative amplifier and connected to an optical chopper modulating the pump pulse for recording signal phase (laser-on, laser-off). Within the detection module, the probe light was dispersed by a self-contained grating and imaged onto a 1024-pixel CMOS detection array for an intrinsic 2 nm energy resolution of the continuum probe.

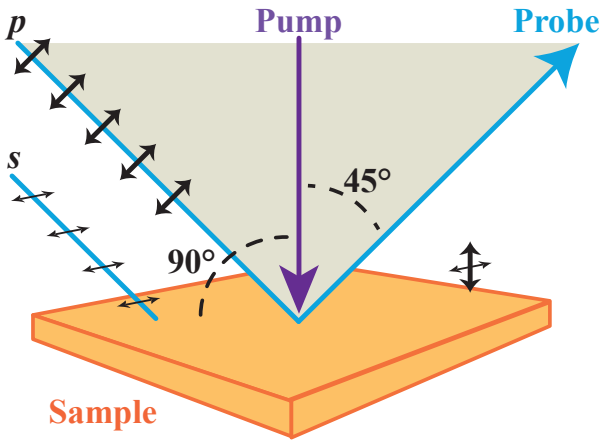


Figure 4.4: Polarization orientation of probe pulse in the transient reflectance measurements. The *p*-polarized light contains electric field components along the surface plane and the surface normal. *s*-polarized light only contains an electric field in the plane of the surface.

The particular geometry of the experimental setup was arranged such that the excitation pulse was incident along the surface normal of the sample and the probe pulse reflected at 45 degrees incidence (Figs. 4.1b and 4.4). Based on a calculation of the depletion width at 0.1 wt. % Nb doping, 300 nm (4.1 eV) and 800 nm (1.55 eV) light pulses were selected as the pump and probe wavelengths in prior experiments to illuminate the entire space charge region of 25 nm. [8] Here, due to a significantly higher energy excitation in the ultraviolet and interrogation wavelengths in the visible (Fig. 4.2a), the expected pump and probe depths are less than the 25 nm depletion region—with the 266 nm pump providing 13 nm excitation depth ($d = \lambda/4\pi\kappa$) and the 400 nm pulse yielding a 12 nm probe depth. With both a 400 nm and broadband visible light probe, sub-band gap transitions are interrogated, either between

in-gap states or between bulk band states and midgap states. Signals arising from intraband transitions, as were examined with 800 nm probe light, may also be present with these probe wavelengths as well.

Pump fluences of 0.05-0.06 mJ/cm$^2$ were utilized for excitation for all experimental conditions unless explicitly varied for fluence dependence measurements in air or at open circuit in 0.1 M sodium hydroxide solution. Polarization of both the pump and monochromatic probe were modulated through the use of a 266 nm and 800 nm $\lambda/2$ waveplates, respectively. Due to the inherent difficulty in generation of white light with controlled polarization, [20] no polarization studies were conducted for the supercontinuum probe.

Global analysis of white light continuum data was carried out following singular value decomposition (SVD), the methodologies of which are detailed in Appendix A. Briefly, singular value decomposition enables the extraction of the principal components (eigenvectors) that contribute to total transient kinetics and spectra; these components are often directly related to electronic species or states in the overall system. [21] In contrast to considering the non-decomposed broadband spectra as a whole, by analyzing each component independently through SVD, the behavior and reactivity of one electronic species can be distinguished from that of another state under different conditions. The relative weight of each component's contribution to the total transient response is indicated by its corresponding singular value.

## 4.4 Results

### 4.4.1 Photoelectrochemical Roughening

In Fig. 4.5a and b, SEM images of the pristine and roughened surfaces of strontium titanate are shown. The pristine $SrTiO_3$ sample shows a smooth, polished surface ($R_a <$ 5 Å) and no significant features on the 100 nm scale. In contrast, the roughened surface displays striations on the order of 20-100 nm, indicating that some rearrangement of the surface takes place under photoelectrochemical conditions. Comparison of the low-energy electron diffraction patterns for a pristine sample and a roughened sample, also in Fig. 4.5c and d, led to a similar conclusion. The diffraction pattern for the as-received n-type strontium titanate sample showed a (1 x 1) surface symmetry at beam electron energies of 100 eV, and 70 eV at significantly lower intensity. The roughened sample, interestingly, also displayed a (1 x 1) symmetry, though it only showed this pattern at a beam energy of 97.5 eV, with a drop-off in intensity as the energy was modulated around this center value. The absence of a distinct diffraction pattern at lower electron energies indicated rearrangement to a surface with limited long-range periodicity; the development of an amorphous surface during roughening is also a possibility. ICP-AES analysis revealed negligible leaching of strontium or titanium atoms in the electrolyte. Of the total charge applied to the sample, only 0.054% (0.018% Sr, 0.036% Ti) contributed directly to the dissolution of $SrTiO_3$. Together, the SEM images, LEED patterns, and ICP-AES measurements indicate that minimal material was lost during the roughening procedure and, further, that the depth of the roughened layer

extends no more than a few nanometers into the sample surface at most.

Over the course of transient reflectance measurements, a decrease in reflectivity was observed—primarily at the higher wavelengths 600-700 nm—as evidenced by decreasing photon counts reaching the detector. The reduced reflectivity was likely correlated with the physical roughening of the sample surface. The 400 nm and broadband white light probes were expected to report on discrete molecular surface states that lay energetically within the band-gap, with observed transients mapping the formation and/or resultant charge transfer dynamics of midgap states. Interestingly, despite the loss of periodicity and the apparent striation in the sample surface (Fig. 4.5), neither the 400 nm kinetics nor the broadband white light data showed any changes, producing identical behavior before, during and after the treatment. Previous studies have confirmed that optical signatures of discrete molecular

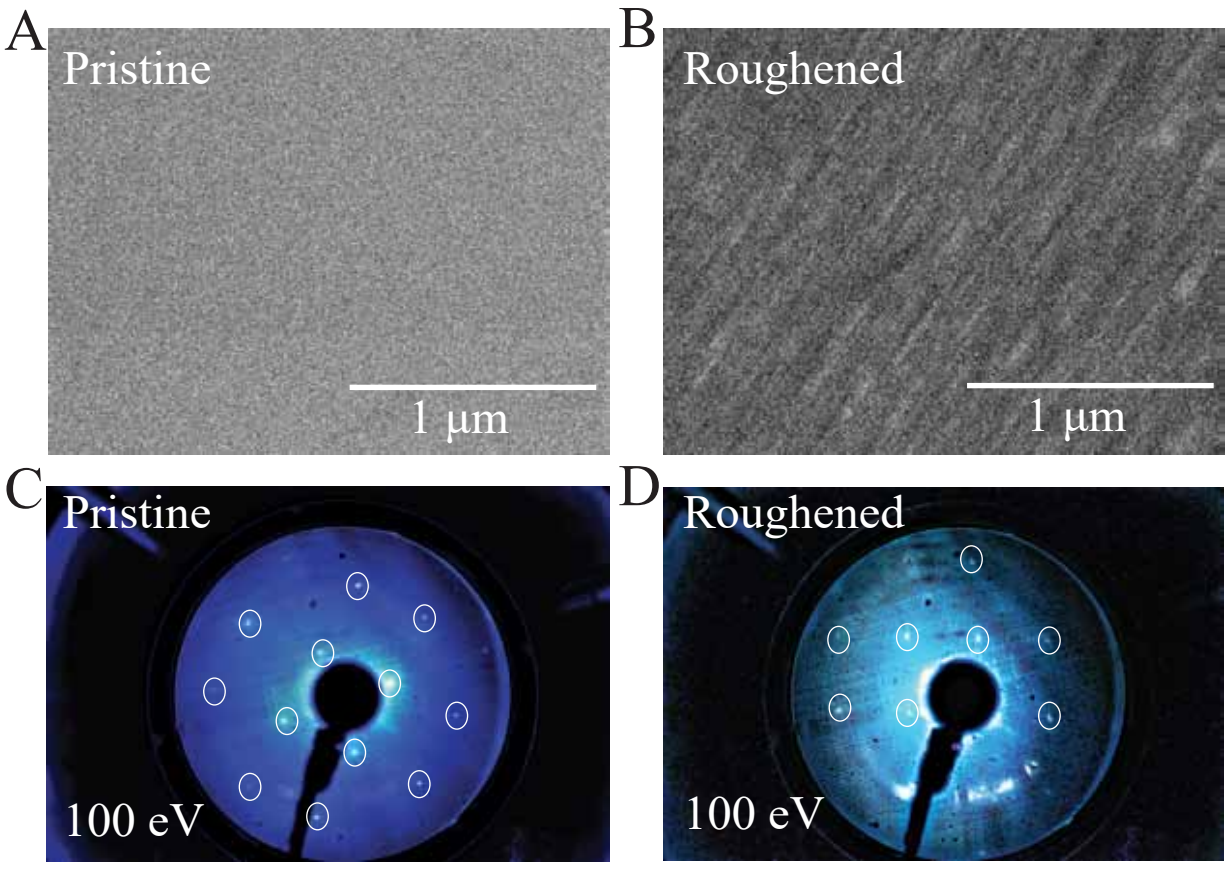


Figure 4.5: SEM images of (a) pristine and (b) photoelectrochemically roughened n-doped strontium titanate at 12000x magnification. LEED diffraction patterns of corresponding (c) pristine and (d) roughened n-$SrTiO_3$, at electron beam energies 100 eV. Bright spots of the diffraction pattern are circled for easier identification.

structures may be observed in the absence of long-range periodic order. [22, 23] The preservation of the kinetics after roughening was taken as evidence that the presence of discrete molecular midgap states, their formation and charge transfer dynamics—evidenced by sub-band gap optical transitions—and their interactions with the local electrolyte environment were unaffected by the photoelectrochemical treatment.

### 4.4.2 Transient Data with 400 nm Probe

Using a monochromatic 400 nm probe pulse, two distinct hole species were isolated and identified by their unique formation dynamics. The transient behavior of the two states was analyzed under several experimental conditions, including probe polarization, hole scavengers, and pump fluence, which revealed the localized, interfacial nature of the hole species. Based on their formation rates, the dynamics of the two holes were ultimately attributed to those of a titanium-oxyl radical (Ti-O*) and an additional surface-bound, possibly distorted hole species with an unknown molecular form.

Initially, the ultrafast dynamics of n-$SrTiO_3$ were collected at 400 nm under an applied bias of 0 V. The 400 nm kinetic trace at 0 V, shown in Fig. 4.6a, comprised a strong negative absorption signal. Before delving into the data, it is important to note that, although the data are collected in reflectance mode $\Delta R/R$ (%), the transient signals here are referred to as changes in optical density $\Delta A/A$ (OD), which is more commonly used for transient transmission measurements. Absorbance changes themselves are defined as $\Delta A = -\log(I_{on}/I_{off})$. Consequently, positive reflectance signals, where the amount of probe light reaching the detector increases, are represented as negative changes in absorbance—arising from ground-state bleach or stimulated emission contributions. Similarly, negative reflectance responses, or decreases in light intensity at the detector, are interpreted as increases in optical density due to excited state absorptions. As described above, negative absorbance signals are considered indicative of either a ground-state bleach or stimulated emission transition. Given several studies on the photoluminescent behavior of strontium titanate—specifically transitions occurring between the conduction band and in-gap defect states—the negative signal was interpreted as arising from stimulated emission contributions. [24–27]

A significant probe polarization dependence was observed at 400 nm, as depicted in Fig. 4.6a, indicating that the observed hole species were in fact surface states and that the dynamics at 400 nm uniquely describe the competition between these two surface states to dictate the surface composition. Upon changing the polarization of the probe pulse from *p*-polarization to *s*-polarization, a two-fold increase in bleach signal was observed, though the kinetics were unchanged. The nature of our reflectance measurement adds a small layer of complexity in analyzing the polarization data. Because the probe pulses are angled at 45 degrees with respect to the surface normal, the *p*-polarization light pulse will probe electronic transitions with transition dipole moments both in- and out-of-plane with the sample (Fig. 4.4) at a ratio of 50:50. In contrast, *s*-polarization will selectively (i.e., 100%) probe optical transition dipoles parallel to the plane of the crystal face. From the doubled 400 nm signal, it was concluded that the monochromatic hole signature(s)

exclusively contained in-plane transition dipole moments. Because strontium titanate is a cubic perovskite and, therefore, very symmetric, hole species within the three-dimensional bulk would be expected to show equal contributions from both out-of-plane (perpendicular to the surface) and in-plane optical dipoles. However, as no out-of-plane component was observed in the polarization measurements at 400 nm, the two hole species were attributed to surface states with in-plane optical dipoles. Theoretical calculations additionally confirm that in-plane (*s*-polarized) transition dipoles can be described by transitions of surface-bound radical holes to conduction band edge electron states (Fig. 4.7). This confirms both our assignment of the observed signal to stimulated emission and two common radical hole species as possible contributors to the signal. Subsequent scavenger dependence measurements also

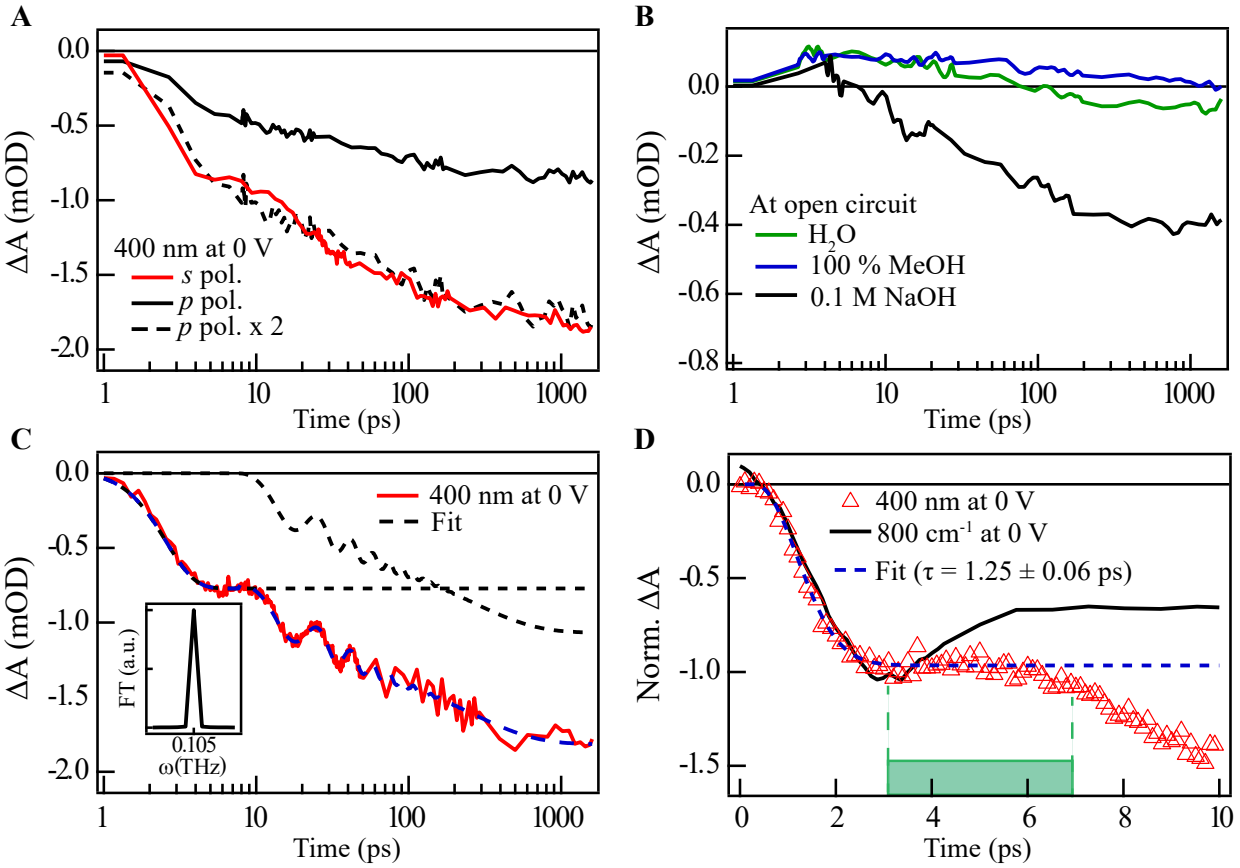


Figure 4.6: Dependence of the $SrTiO_3$ 400 nm kinetics to (a) probe polarization and (b) the presence of scavengers and hydroxide ions. (c) The fit of the kinetic trace is composed of a stretched exponential and a delayed normal exponential function. (d) The early rise time of the 400 nm kinetics matches that observed in the far-infrared for the Ti-O* radical. The 400 nm delay extends from $\sim$ 3 ps to 7 ps, as shown by the parallel shaded region.

confirmed the interfacial—not sub- or near-surface—nature of the 400 nm hole signatures.

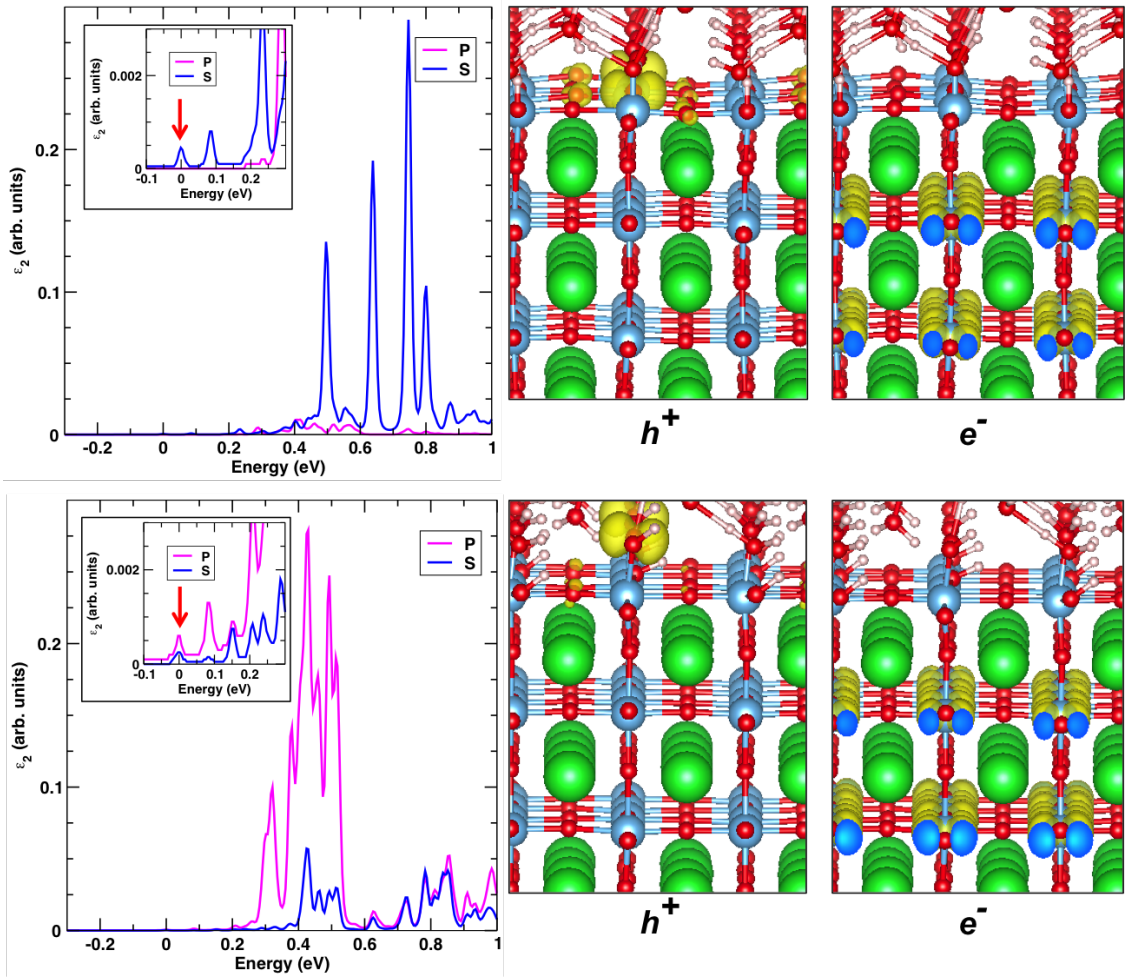


Figure 4.7: Comparison of transitions for hole states coupled to electron states in the conduction band for a lateral surface hole (top) and a titanium-oxyl radical hole (bottom). From left to the right: plots of oscillator strength versus the energy of the final conduction band state (the band edge is 0 eV)—*s*-polarization indicates in-plane transition dipole moments, whereas *p*-polarization tracks out-of-plane transition dipoles; molecular orbital depiction of initial hole states; and the corresponding lowest energy conduction band state, also marked by a red arrow in the transition plots.

Under open circuit conditions, the kinetics at 400 nm reveal a long-lived bleach signal in 0.1 M NaOH solution; the dynamics are roughly identical to those measured under an applied bias (0 V). When the basic environment is replaced by pure water at pH = 7, a drastic decrease in the amplitude of the bleach is observed, as seen in Fig. 4.6b, along with the growth of a positive absorption signal. In the presence of both methanol and thiocyanate

hole scavengers [28], the negative signal disappears completely, leaving only an absorptive feature. There is a significant dependence on the concentration of hydroxide ions as evidenced by the kinetics in pure water at pH 7 versus those in 0.1 M NaOH (pH 13). Valence band holes would not be expected to show such sensitivity to electrolyte conditions. Therefore, the strong dependence of the 400 nm kinetics on the presence of hole scavengers, as well as the absence of hydroxide ions at the solid-liquid interface, further supports the assignment of the 400 nm signal to surface-bound species.

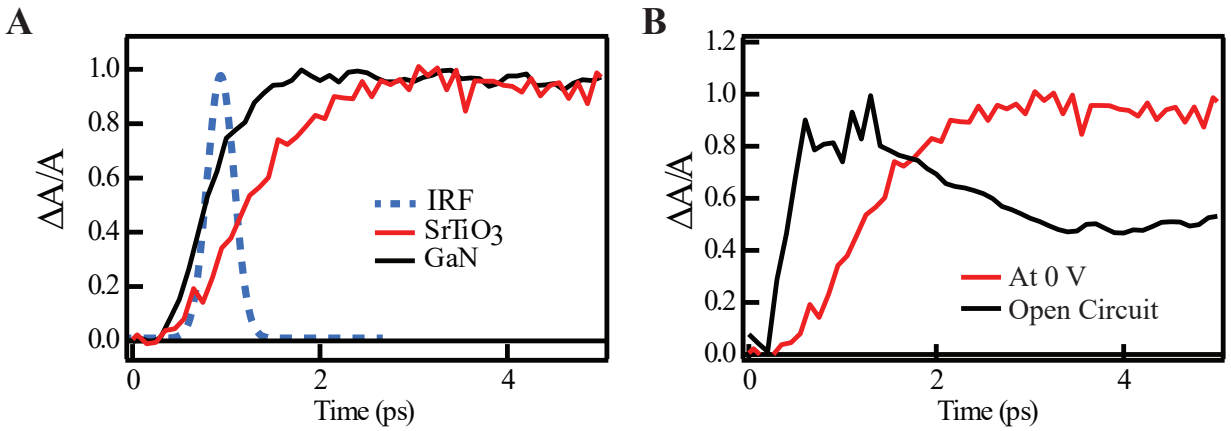


Figure 4.8: (a) Early time kinetics of n-$SrTiO_3$ compared with kinetics of gallium nitride (GaN) and the instrumental response function (IRF) (b) a comparison of the early time kinetics of n-$SrTiO_3$ at low and high fluence.

To model the formation of and identify these hole species, the 400 nm kinetic trace was fit with a single exponential function convolved with the instrument response function ($\sim$ 200 fs) for the first radical and a delayed single exponential function for the second (Fig. 4.6c). The fits yielded a rise time of 1.25 $\pm$ 0.06 ps for the first species, and a 4 ps delay time followed by a 36 $\pm$ 10 ps formation time for the second radical species. The early dynamics of the 400 nm probe were recorded in very fine detail, provided by small delay increments ($\Delta\ t =$ 100 fs), to ensure that the 400 nm rise time was accurately measured. The measurement of this 1.25 ps rise time was not limited by the instrument response function of our set-up—the convolution of the pump and probe pulses—as evidenced by additional measurements on a sample of gallium nitride (GaN) under the same experimental conditions. With the same 100 fs delay increments, a faster rise time (0.63 ps) was observed in kinetic fits for GaN (Fig. 4.8a), significantly shorter than the rise time of 400 nm measurements of n-$SrTiO_3$ at 0 V. Thus, the recorded formation time of the first hole species (1.25 ps) was deemed accurate and not an artifact of the measurement. An additional oscillation with a frequency of $\sim$ 0.1 THz was observed, overlaid on the second rise component (Fig. 4.6c).

The first rise of 1.25 ps charts the formation of the first surface-bound hole species following excitation. The 400 nm kinetic trace, which was previously shown to reflect in-

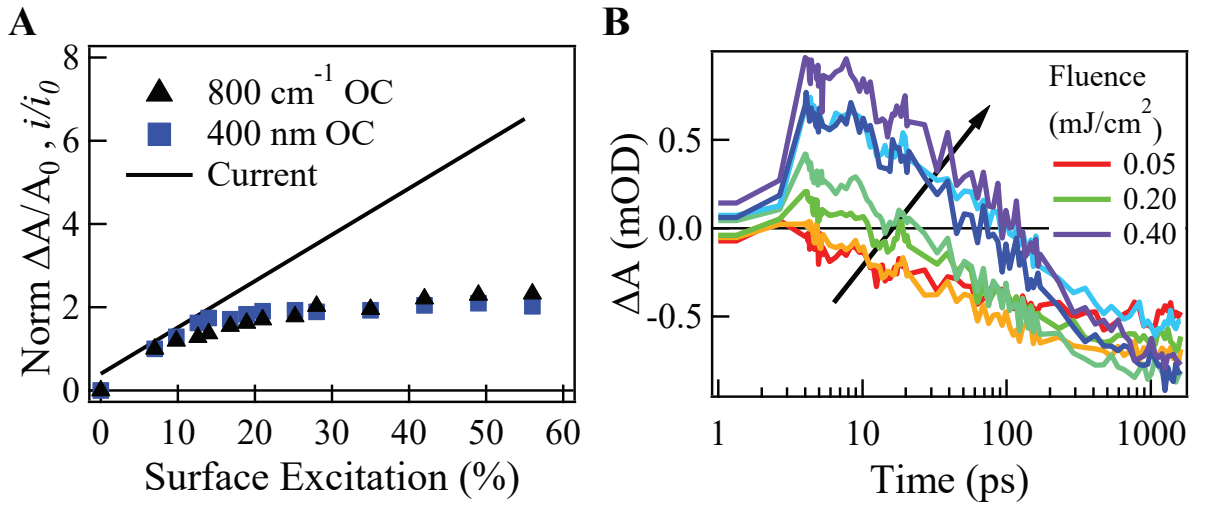


Figure 4.9: (a) Fluence dependence of the 400 nm signal magnitude at open circuit, compared with the fluence dependence of far-infrared Ti-O* signal under fluence and measured photocurrent. (b) The 400 nm kinetic traces, at 0.05 mJ/cm$^2$ increments, show the growth of an absorptive feature with increasing fluence.

plane optical dipole transitions and to depend significantly on electrolyte conditions, was expected to involve potentially both a lateral hole and oxyl radical state as well as other molecularly ill-defined, surface-trapped hole species. The two main candidates considered for the assignment of the early rise were the lateral and oxyl radical states based on previous reports of their coexistence at longer timescales in $TiO_2$. [1] Density functional theory calculations of photohole configurations at the surface have also revealed that the oxyl radical and lateral hole are thermodynamically low in energy and, therefore, preferred hole states. While the contribution of the lateral hole to the first rise time could not be confirmed, theory suggested its contribution to the signature due to its strongly *s*-polarized transition dipole moment. The contribution of the oxyl radical formation to the 1.25 ps time constant was supported by earlier transient measurements on $SrTiO_3$ and literature values for the relaxation of surface hydroxyl O-H stretches.

Notably, the rise time (1.25 ps) of the first hole species matched the observed rise time of the Ti-O*-induced subsurface vibration from far-infrared experiments (Fig. 4.6d), [29] strongly evidencing contributions to the initial rise of the 400 nm signal from the formation dynamics of the Ti-O* species. The decrease in the 800 cm$^{-1}$ kinetics over 3 ps, illustrated in Fig. 4.6d, in a time window where the 400 nm signal remains flat (delay time), can be explained by the coupling of the infrared subsurface vibration to external solvent and electron dynamics. The coupling of the vibration to its external environment results in a Fano lineshape that evolves during initial relaxation of the solvent. The Fano lineshape is asymmetric and, for the oxyl-induced vibration, shifts the center energy and amplitude of

the vibration such that the kinetics at this particular wavenumber (800 $cm^{-1}$) appear to decrease.

In the literature, there have also been reports of solvent reorganization and hydrogen bonding network relaxation following the excitation of surface-bound hydroxyl groups [30] as well as bulk water [31]. In ultrafast transient infrared measurements of water, the introduction of energy into water through vibrational excitation results in both vibrational and orientational relaxation of O-H bonds. The relaxation processes display time constants of 1.45 ps and 1.53 ps, respectively, followed by 0.8 ps over which O-H bonds break due to the energy introduced; in isotopically mixed water ($H_2O/D_2O$) these time constants were observed to have a spread of 1-1.8 ps. [31] A similar time constant is observed for surface-bound hydroxyl species. [30] Orientational relaxation is less important to a constrained O-H bond and $H_2O$ at an interface than in bulk water. However, the rapid injection of vibrational energy into the O-H bond by a laser pulse is rather analogous to the ultrafast localization of a hole on a Ti-OH moiety at the $SrTiO_3$ interface; therefore, the vibrational relaxation following far-infrared photoexcitation is likely to be very relevant. The localization of a hole carrier onto the oxygen atom of a dangling Ti-OH bond and the subsequent release of its energy as it thermalizes will similarly introduce vibrational energy into the Ti-O and O-H bond as they adjust to accommodate the hole carrier.

Indeed, the observed rise time at 400 nm shows the 1.25 ps time constant that would signify vibrational relaxation of an O-H bond. Furthermore, the subsequent thermalization of the solvent and interfacial hydrogen bonding network to the generated hydroxyl species is expected to occur over the course of several picoseconds (4 ps) following vibrational relaxation of the excited water molecule, [31] which matches the observed delay in our 400 nm kinetic trace. The oxyl radical is similarly expected to induce relaxation of the surrounding electrolyte environment relative to the localized hole. However, we cannot discount contributions from other hole species (such as a lateral hole) to the 1.25 ps rise time at 400 nm. The localization of a positive carrier on the oxygen of a lateral hole (Ti-O*-Ti) could similarly induce perturbations of the surrounding water environment as the oxyl radical is presumed to do; there is no evidence to support or negate the contribution of lateral hole formation to this 1.25 ps rise time. Generally, the observed 1.25 ps time constant may indicate localization of holes on surface oxygen sites—either Ti-O* or Ti-O*-Ti. For the time being and in the absence of evidence to suggest that other contributions are present, the agreement with infrared transient data and reported time constants of 1.25 ps and 4 ps for the relaxation of water and surface-bound hydroxyl species supports the tentative assignment of the first rise and delay time to the formation of surface radical hole species of a possible oxyl (Ti-O*-Ti) or lateral (Ti-O*-Ti) form.

Unfortunately, no prior transient measurements or literature could assist in the assignment of the relatively long rise component (36 ps) of the second species. The interfacial nature of the second hole was previously indicated by polarization and scavenger dependence measurements. The additional distorted nature of the surface hole was suggested by an associated oscillation overlaid on the second rise component (Fig. 4.6c), the frequency of which (0.1 THz) was within the range expected for acoustic phonons in $SrTiO_3$. [32–34] The

second hole was tentatively attributed to surface-bound, distorted hole without a specified molecular form.

Figure 4.9 shows the behavior of the signal at 400 nm with increasing fluence under open circuit conditions. The number of photogenerated holes at the surface is expected to increase linearly with pump fluence. Here, surface excitation coverage is defined as the number of holes per in-plane oxygen atoms at the surface of a perfectly uniform $TiO_2$-terminated crystal. At open circuit, the lowest fluence (0.06 mJ/cm$^2$) corresponds to 8% excitation whereas the highest fluence examined (0.42 mJ/cm$^2$) equates to 52% surface excitation, indicating excess photogenerated carriers. The kinetics under voltage (0 V) are preserved under the lowest fluence at open circuit (Fig. 4.6a and b). With increasing fluence, the 400 nm kinetics produce an additional absorptive component at early times, preceding the 1.25 ps rise of the oxyl radical (Fig. 4.9b). The absolute magnitude of the negative signal increases until an average 20% surface excitation is achieved, after which the signal magnitude saturates and remains constant despite increasing numbers of incident photons and photogenerated holes (Fig. 4.9). The saturation of the 400 nm signal at open circuit implies a limited number of surface sites accessible to the photogenerated holes.

In summary, two distinct surface radicals could be distinguished from the 400 nm kinetics alone. The observed dependence on probe polarization and scavengers indicated that hole species having in-plane optical transition dipoles and existing at the interface contributed to the monochromatic signal. The assignment of the strong negative absorption signal to stimulated emission involving midgap states—based on $SrTiO_3$ photoluminescence literature—was supported by theoretical calculations of in-plane optical transition dipoles between conduction band electron states and midgap, surface-localized holes. Two well-separated time constants were also extracted from fits to the 400 nm kinetics, indicating that two hole species were formed within our time window. Furthermore, the 400 nm kinetic trace showed a fixed delay time between rise components that has previously been attributed to solvent and lattice rearrangement. In particular, the first hole species was found to display a formation rate (1.25 ps) that matched the dynamics of an oxyl radical-induced response in the far-infrared. This time constant also agreed with previous reports of relaxation dynamics in bulk water and interfacial hydroxyl species, bolstering our assessment of the signal as a surface-bound oxygen-localized hole state. The similarity between the observed rise time and that of water thermalization in the literature supported a tentative assignment to the formation of a Ti-O* radical, though contributions from Ti-O*-Ti and similar radicals could not be excluded. The second species was attributed to a distorted surface-bound hole of unknown molecular structure. Lastly, fluence dependence measurements at open circuit demonstrated saturation, indicating a limited number of surface-sites available to both interfacial hole species.

### 4.4.3 Scavenger and Fluence Dependence of White Light Data

In addition to measurements at 400 nm, the n-$SrTiO_3$ solid-liquid interface was also probed with a white light continuum in the presence of scavengers and under variable pump fluence

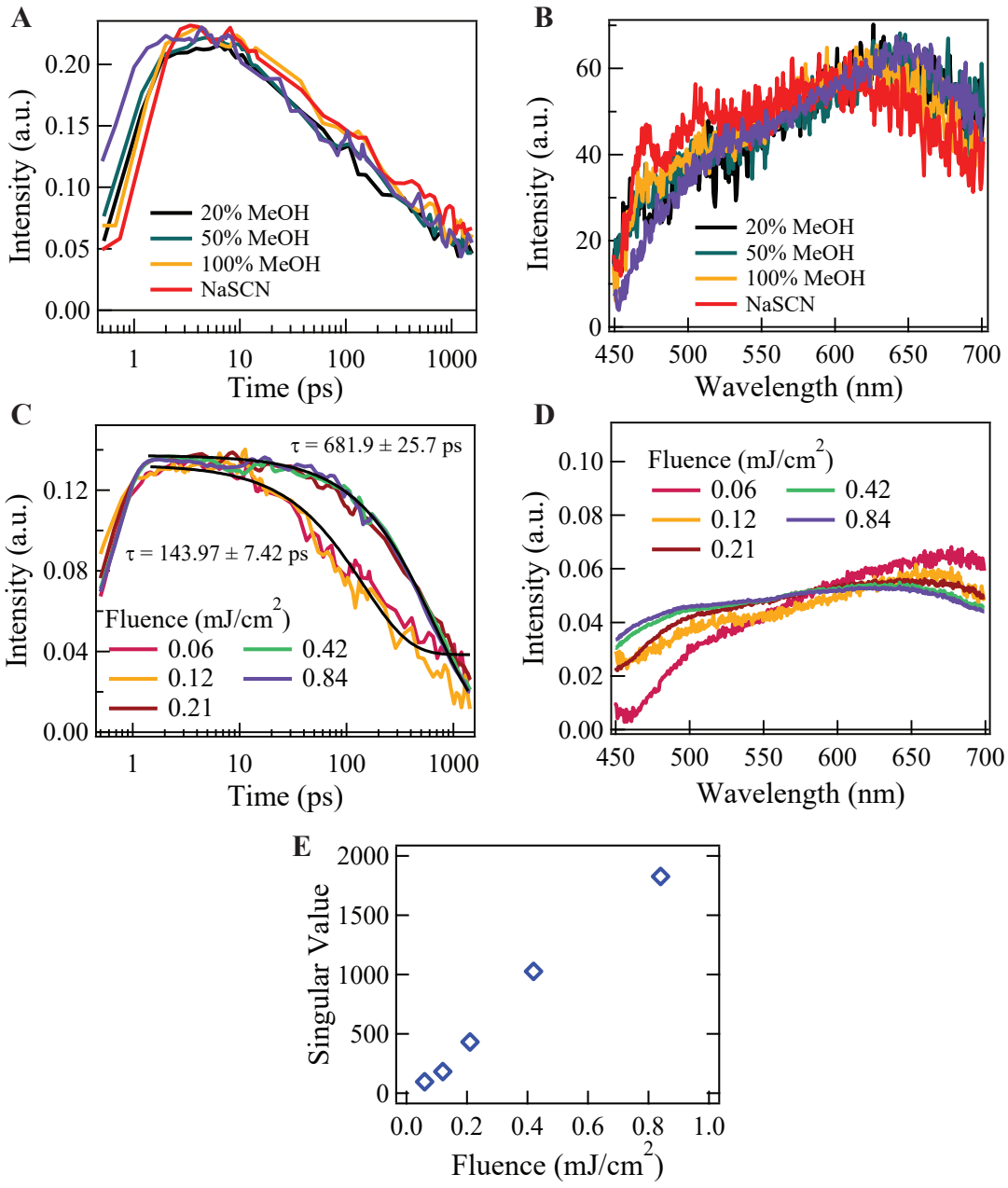


Figure 4.10: The eigenkinetics (a, c) and eigenspectrum (b, d) of the first component of the white light singular value decomposition in the presence of hole scavengers (a,b) and under increasing pump fluence (c,d). The weight, or contribution, of the first component to the raw broadband spectrum is given by its singular value. Under increasing fluence, the singular value also increases.

at open circuit. Ultimately, a third hole signature was extracted from singular value decomposition analysis and assigned to excited state absorptions involving valence band holes within the depletion region.

Under open circuit conditions and a fluence of 0.06 mJ/cm$^2$, the dominant component of the white light spectrum—whose eigenkinetics and eigenspectrum were extracted by the SVD analysis—revealed a positive absorption signal. The eigenspectrum displayed a broadband excited state absorption, with a peak of 650 nm (1.9 eV); the eigenkinetics were observed to decay with a time constant of 143.97 ± 7.42 ps—greater than the observed rise times in the 400 nm kinetics by almost an order of magnitude. Based upon our band banding model and the expected removal of electrons to the bulk, the signal was interpreted as an excited state hole absorption. Interestingly, the eigenkinetics and eigenspectrum of the dominant SVD component proved to be insensitive to hole scavengers—both methanol and thiocyanate (Fig. 4.10a,b)—unlike the two radical surface holes in the 400 nm traces. The lack of dependence on the electrolyte conditions was taken as evidence of the holes in question being physically separated from the interface.

Furthermore, the first SVD component under open circuit conditions did not display the same signal saturation with increasing fluence as the 400 nm probe (Fig. 4.10e). Instead, the dominant component's contribution to the raw spectrum—i.e., the singular value—continued to grow linearly with pump fluence while its eigenkinetic and eigenspectral profiles remained relatively unchanged in having both a positive kinetic and spectral profile (Fig. 4.10c,d). We note that the decay constant for the hole signature did increase significantly under high fluence (681.9 ± 25.7 ps) and the spectral weight of the eigenspectrum shifted towards lower wavelengths. However, both the constancy of the positive absorption signal and the linear growth of the broadband signal can be interpreted as evidence that the dominant component of the white light signal is not surface site-limited and, moreover, that a large density of states was available to this particular hole species.

From the dominant SVD component of the white light probe, an additional third hole species —apart from the two hole states that were identified in the 400 nm kinetics—was clearly observed under open circuit conditions. Due to the red-shifted (650 nm peaked) broadband eigenspectrum of the first component and a previous assignment of energetically similar species at 800 nm to free holes [8], these additional carriers at open circuit were assigned to excess holes in the valence band. This assignment was supported by several other observations. Firstly, the broadband signature differed from the emissive negative monochromatic signal in its absorptive nature and the long time constant describing its decay. The assignment of this transition to excited state hole absorptions was founded upon the general picture of the $SrTiO_3$ solid-liquid interface (Fig. 4.1a), in which negative charge carriers are removed from the 12 nm probe region. The long decay is expected for valence band holes in the depletion region, for which recombination with electrons is substantially reduced. Secondly, the insensitivity of the absorption signal to hole scavengers imply a non-surface-bound hole species. Finally, its lack of saturation with fluence demonstrated both that the hole species was not surface-site limited and had an enormous density of states available. While polarization dependence measurements were not conducted with the white

light probe and could not be used to provide additional information regarding nature of the broadband signature, the white light hole species was definitively not a surface-bound species.

### 4.4.4 Voltage Dependence of 400 nm and White Light Data

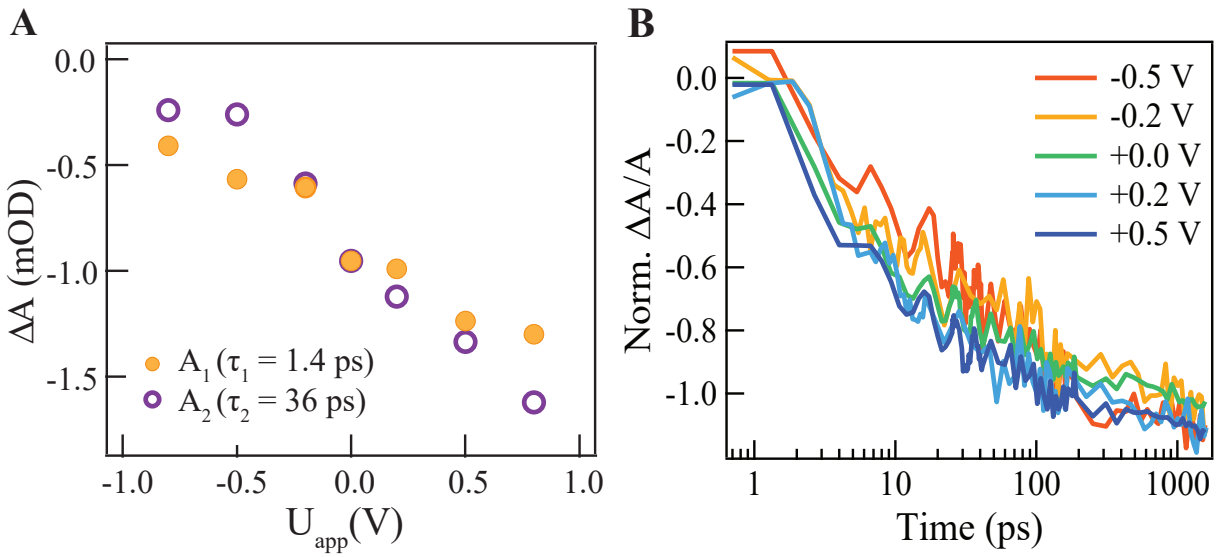


Figure 4.11: (a) Signal amplitude at 400 nm separated into contributions from both the first and second rise components; the contributions increase linearly with applied voltage. (b) Comparison of 400 nm kinetic traces under different bias; the kinetics remain the same.

The 400 nm kinetics, which were initially examined under an applied bias of 0 V, were recorded as a function of voltage, as shown in Fig. 4.11. A negative absorption signal—previously attributed to a stimulated emission transition—was observed at all voltages. Interesting, the stimulated emission signal was found to increase linearly with the application of voltage (Fig. 4.11a). However, the kinetic profile and the measured time constants at 400 nm remained fairly constant irrespective of the bias.

To understand voltage response of the 400 nm signal, the transient response of the broadband white light probe was also examined as function of applied potential. The transient behavior of the dominant first SVD component—both eigenkinetics and eigenspectra—is shown in Fig. 4.12a,b. At -0.8 V, a positive absorption signal identical to the signal at open circuit was observed; this signal was previously attributed to valence band holes. As the applied bias was adjusted to more positive potentials, two changes were observed. Notably, the eigenkinetics changed from an entirely positive absorption signal under OC and -0.8 V into a predominantly negative absorption under positive bias. Furthermore, as positive volt-

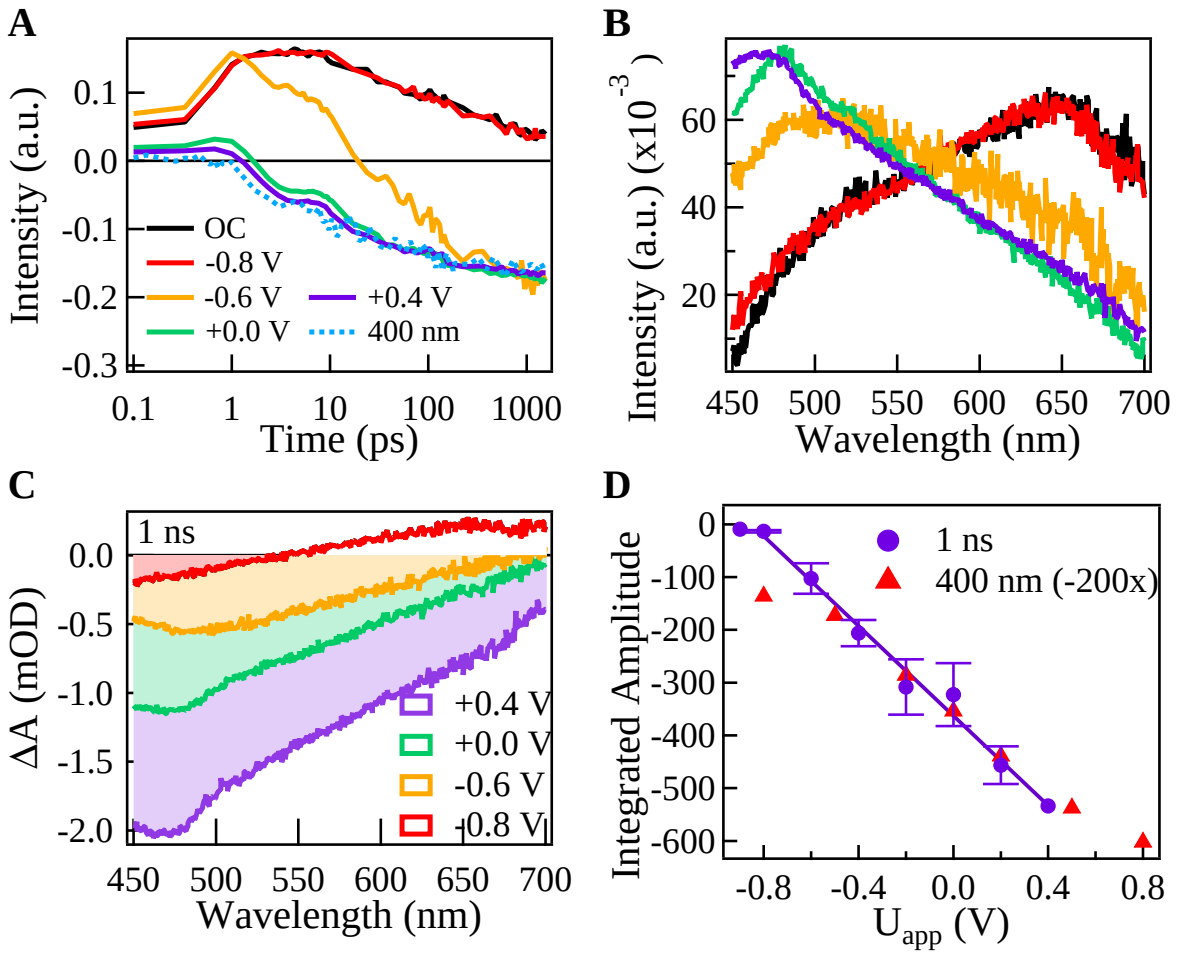


Figure 4.12: The eigenkinetics (a) and eigenspectrum (b) of the first component of the white light singular value decomposition as a function of applied voltage. (c) The raw white light transient spectra at 1 ns with voltage. (d) A plot of the integrated amplitude of the negative absorption signal (shaded in panel c) as a function of voltage. The white light integrated amplitude is compared with the 400 nm signal magnitude.

age was applied, the eigenkinetics transformed into an identical match of the kinetics taken at 400 nm (Fig. 4.12a). In addition, between -0.8 V and +0.4 V, the eigenspectrum was seen to change its profile, shifting its spectral weight towards lower wavelengths and peaking at 475 nm (2.6 eV) for an overall shift of 0.7 eV (Fig. 4.12b). In the raw transient white light spectrum, the signal at 1 nanosecond delay was also found to change drastically with voltage, with an increase in overall signal amplitude. Taking the integrated area of the negative absorption signal in the raw spectra (Fig. 4.12c, shaded), the increase in the signal magnitude was determined to be linear with voltage (Fig. 4.12d). The linear trend reveals a

similar voltage dependence as exhibited by the 400 nm signal.

Before moving on to the significance of the 400 nm and white light voltage dependence, we briefly discuss the necessity of singular value decomposition analysis to elucidating the observed behavior. SVD eigenkinetics and eigenspectra are extracted not simply from one wavelength but the entire spectrum, thereby evaluating global transient responses. Furthermore, as the raw transient spectrum contains contributions from several SVD components—each with its own eigenkinetics and eigenspectrum—decomposition of the raw broadband response enables us to distinguish the effects of certain experimental conditions on each component. For example, as shown in Fig. 4.12c, the 1 ns spectrum at -0.8 V arises from a secondary, less significant SVD component. This component is not the dominant component that is highlighted in panels a and b and that was the subject of earlier discussion for white light scavenger and fluence measurements. However, as increasingly positive voltage is applied, the changes in the raw spectra—both spectral shift and increase in signal magnitude—are a result of dynamic behavior in the eigenspectrum of the dominant component (Fig. 4.12b) not in that of the secondary SVD component. As shown in Fig. 4.13, the eigenspectrum of the secondary component does not change substantially with applied voltage. We have omitted discussion of the secondary component in relation to fluence and scavenger dependence as it was shown to contribute less than the dominant component to the raw transients—i.e., the secondary component had a lower singular value by a factor of ten.

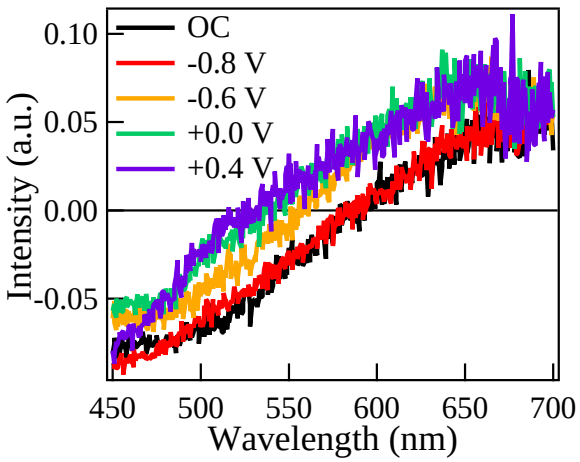


Figure 4.13: The evolution of the eigenspectra of the secondary SVD component as a function of applied bias. The observed spectrum does not appear to change substantially between -0.8 V and +0.4 V.

Taken together, the potential-dependent behavior of the first SVD component supports a model in which excess photogenerated holes are redistributed from the valence band into the two distinct surface-bound radical hole states (400 nm) under increasing voltage. This redistribution is illustrated by four main observations: (1) the transformation of the eigenkinetics

into the 400 nm kinetic trace; (2) the change of the eigenspectrum to a negative absorption, peaked at lower wavelengths; (3) the absence of change in the secondary component eigenspectrum; and (4) the linear dependences of the 400 nm and white light signal amplitudes on voltage.

Under increasingly positive voltages, the primary SVD eigenkinetics assumes the profile of the 400 nm kinetics (Fig. 4.12a). The kinetic transformation shows that the two surface radical species replace the valence band holes as the dominant species observed in the white light. At -0.6 V, an eigenkinetic trace that appears to be a hybrid of the open circuit/-0.8 V eigenkinetics (valence band holes) and the monochromatic profile (surface radicals) is observed. This indicates that at some voltages, the valence band holes and the two surface-bound radicals contribute somewhat equally to the white light response. While the kinetic transformation is occurring, a related shift in the primary SVD component's eigenspectrum is observed (Fig. 4.12b). The eigenspectrum evolves from an excited state absorption signal to a negative absorption signal, which in consideration of the eigenkinetic changes is most probably due to a broadband stimulated emission. The change from a valence band excited state hole absorption to a stimulated emission signal is further supported by the shift of the peak energy for the eigenspectra—moving from a 650 nm (1.9 eV) peak to a 475 nm (2.6 eV) peak. These wavelengths are approximately close to the corresponding monochromatic transitions measured for excited state (intraband) absorption by valence band holes (800 nm) [8] and the stimulated emission signal from the conduction band to midgap radical states (400 nm), described earlier.

In contrast to the changes in the primary SVD component eigenvectors, the eigenspectrum of the secondary SVD component remains fairly fixed across the voltages applied. It would not be unreasonable to expect the valence band holes to displace this unknown species (shown in Fig. 4.13) as the second most important component if the population of valence band holes was independent of the two surface radicals' populations. In such a case, the first SVD component would reflect the growing contribution from the two surface radicals, the second component the valence band holes, and the third component the lesser, unchanged eigenspectrum of Fig. 4.13; however, this displacement does not occur. Therefore, in the broadband data, the valence band hole contribution is not independent from that of the surface hole radicals. Lastly, both the signal amplitudes of the raw broadband transient spectrum and the 400 nm kinetic trace show a similar linearity in their dependence on voltage, implying that both signals track the growth of the same species.

A schematic illustrating the redistribution of holes from the valence band into the surface radical states is presented in Fig. 4.14, where the voltage-dependent eigenkinetics of the dominant SVD component (Fig. 4.12a) is given by $k_{WLC}(V)$. The rate constants $k_0$, $k_1$, $k_2$ represent the decay of the valence band holes ($\tau$ = 143.97 ps, under open circuit and negative applied bias, -0.8 V), the formation of the oxyl radical or lateral hole ($\tau$ = 1.25 ps), and the formation of the second distorted radical species ($\tau$ = 36 ps). The population of photogenerated holes that we observed in the first SVD component (Fig. 4.12a,b) is apportioned between the surface radical species and the valence band holes by a fractional weight $x$ that depends on voltage. As a purely speculative example, the fractional value

$x$ may reflect a voltage-dependent activation energy barrier for hole transfer to a discrete surface state from the valence band, as has been considered previously. [8] In such a case, the application of positive bias might induce an increase in the reaction free energy $\Delta G$, such that the rate of (hole) charge transfer would increase, as described by Marcus theory. Therefore, as voltage changes, so will the value of $x$. At a given voltage, the dominant SVD component's eigenkinetics and eigenspectra will reflect contributions from either the valence band holes (-0.8 V), the two distinct surface radicals (+0.4 V), or both (under -0.6 V). Within the disproportionation of holes between the valence band and surface radicals, the two radical species—Ti-O* and the second distorted, surface-trapped hole—are expected to compete for surface sites.

While changes in the eigenkinetics arise from the increasing contributions of the two radical species within our spectral window—as shown in our schematic, there is likely an additional contribution from a voltage-dependent decay for the valence band holes, $k_0$'(V), that we have not illustrated. As described earlier, the valence band hole contribution is not

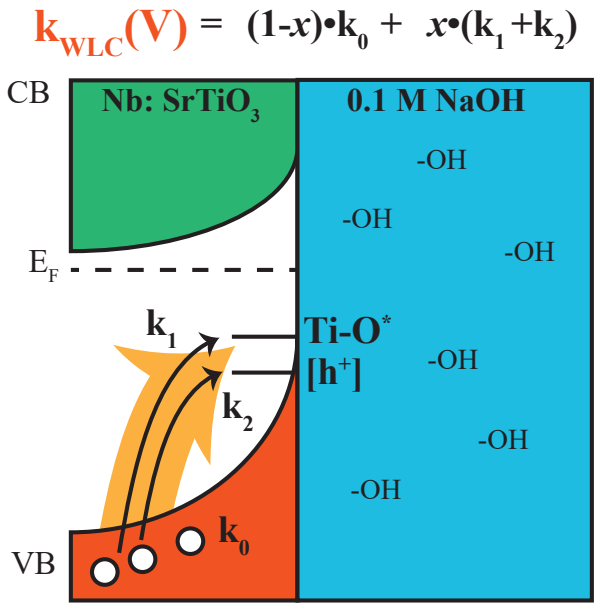


Figure 4.14: Schematic of the voltage-dependent hole redistribution in $SrTiO_3$. Under applied bias, the photogenerated holes are distributed amongst the two surface radical states and depletion region valence band states, as illustrated in the white light SVD kinetics, $k_{WLC}(V)$. The allocation of holes is dictated by a voltage-dependent fractional weight, $x(V)$. The formation time constants of the surface hole species ($k_1$, $k_2$) remain fixed, as shown by voltage dependence measurements; the decay of valence band holes ($k_0$), however, is likely voltage-dependent. Changes in the white light kinetics reflects the different weight of the formation and decay rates to the broadband response.

independent of the surface radicals. Consequently, under an applied voltage the decay of the valence band holes should reflect two time constants—one for the original decay pathway (recombination) as well as another for the transfer of holes to the surface states. In order to deconvolve the contributions of the voltage-dependent disproportionation factor $x$ from the voltage-dependent hole transfer rate, $k_0$'(V) in the white light data $k_{WLC}$(V), further transient experiments with a probe window (such as 800 nm or broadband near-infrared) that will not contain spectral contributions from the surface radical states will be necessary.

### 4.4.5 Current Dependence of 400 nm Transient Data

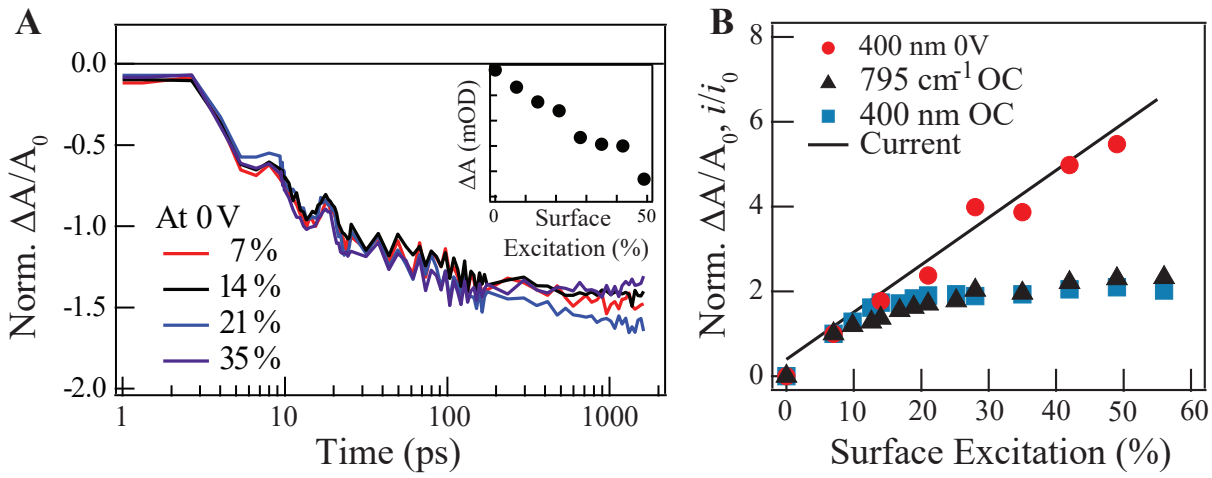


Figure 4.15: (a) Under 0 V, the 400 nm kinetics do not change as a function of pump fluence. The inset shows that the overall 400 nm signal amplitude at 0 V, however, does grow with increasing excitation. (b) In comparison with the fluence dependence measurements at open circuit, the 400 nm signal with an applied bias increases linearly with fluence and tracks the photocurrent.

In addition to voltage-dependence measurements at fixed fluence (0.06 mJ/cm$^2$, fluence dependence measurements at 400 nm were also conducted under an applied bias of 0.0 V (Fig. 4.15a). Interestingly, no change in the 400 nm kinetics was observed under these conditions. At higher pump fluences, however, the signal amplitude was found to increase linearly. Furthermore, unlike the fluence measurements under open circuit, no saturation of the emission amplitude was observed (Fig. 4.15b), implying that the density of available states under voltage was significantly larger than at open circuit. The linear growth of the signal with applied bias also appeared to scale with the increase in photocurrent under increasing pump power.

While the fluence dependence measurements at open circuit established the surface site-limited nature of radical formation, the number of surface sites appeared to increase sub-

stantially under an applied bias. Furthermore, the 400 nm signal matched the linear growth of photocurrent under increasing pump power, which suggested a correlation between charge density/flux and surface sites. It is unknown why the increased concentration of charges at the interface enables more surface radicals to exist but, in all likelihood, the increase in surface sites makes the voltage-dependent redistribution of the valence band hole population into a limited number of surface states a feasible process.

## 4.5 Discussion

The monochromatic and broadband visible light results presented here justify the existence of multiple distinct hole states—two of which are surface-bound—based on their individual responses under a number of experimental conditions. Within the ultrafast window under consideration, the dynamics of the 400 nm probe focus exclusively on site-limited hole species and provide spectroscopic handles with which the evolution of these holes and their reactivity at the surface can be tracked out to later timescales. The broadband white light transient response is also highly sensitive to surface carrier distributions, revealing a transfer of valence band holes to the 400 nm surface states in the presence of an applied bias.

### 4.5.1 Coexistence of Three Hole Species

Fits to the 400 nm kinetic trace—with a stretched exponential for the first rise—reveal two formation times of 1.25 ps and 36 ps, separated by a 4 ps delay time. Due to the long time constant extracted for second rise and the separation of the two rise components by a substantial delay, two distinct hole species were assigned to the optical signature at 400 nm. In the mononchromatic trace at 0 V, polarization dependence measurements revealed that these two hole states contained exclusively in-plane transition dipole moments and, consequently, had to be ascribed to surface-bound radicals. The interfacial nature of the two hole species was supported by the sensitivity of the 400 nm signal to changing electrolyte conditions, including the presence of methanol and thiocyanate scavengers as well as a decrease in the concentration of hydroxide ions at the interface. Additional confirmation for assignment of the two surface-bound radical species was evidenced by signal saturation at open circuit with increasing pump fluence, thereby implying a limited number of accessible surface sites.

The similarity of the early rise time in the 400 nm trace (1.25 ps) to the formation time observed for the titanium-oxyl radical in the far-infrared supported the assignment of the first rise to the formation of the Ti-O* radical; theoretical calculations also supported the possibility of contributions from lateral holes Ti-O*-Ti to this early signature. Both the 1.25 ps rise time and the 4 ps delay have also been previously implicated in the relaxation dynamics of surface hydroxyl species and hydrogen bond networks in water, respectively, and may be indicative of general hole localization at the interface. The second hole species was tentatively attributed to a distorted, surface-bound hole of an unknown molecular form. This assignment was made on the basis of an associated oscillation in the second rise, whose

frequency matched literature values for acoustic phonons, and the fact that a substantial delay and rise time, which can result from lattice or solvent rearrangement, were observed. Unfortunately, there was no comparable signature in the far-infrared to make a confident assignment of the second surface hole species (with a 4 ps delay and 36 ps rise) to the distorted lateral hole. Further investigation to determine the precise molecular form of the second hole—through a time-resolved, structurally-sensitive technique—will likely be necessary to confirm the current assignment. An alternative assignment to the second intermediate in the 400 nm kinetics would be an interfacial bridging species ([Ti-O* + HO-Ti] or [Ti-O* + (H/Ti)-O-Ti]) with dipole components parallel to the surface plane, which have been proposed previously. [1] The formation time of these states would also be expected to display a delay time following diffusion of hole states to the same physical location along the surface as limited by polaronic transport [32] and/or (solvent-mediated) proton-coupled charge transfer [35].

A third hole species was identified through the use of a broadband white light probe, which displayed distinctly different behavior to that seen at 400 nm. For example, the primary SVD signature in the white light was predominantly absorptive, in contrast to the negative signal of the monochromatic kinetics. Additionally, the first SVD component showed neither a change in eigenkinetics or eigenspectrum with scavengers nor a signal saturation with increasing photogenerated holes. In consideration of both its apparent surface insensitivity and its eigenspectrum, which was peaked at 650 nm, the principal SVD component was ascribed to excess valence band holes within the space charge region of $SrTiO_3$.

### 4.5.2 Carrier Distribution and Site Competition at the Interface

Voltage-dependent measurements using both the monochromatic 400 nm and broadband white light probes revealed a redistribution of holes between the valence band and the two radical hole states at the interface. With increasingly positive applied bias, the 400 nm signal increased in magnitude. It is worthwhile to note that, in the voltage dependence measurements, the incident pump fluence was held constant across all voltages. Therefore, the number of photogenerated holes was constant. Consequently, the increase in 400 nm signal with voltage could only have arisen from additional holes moving into these surface states from another pre-existing source. Indeed, from the voltage-dependent 400 nm and white light data, a redistribution of charge carriers across the three hole states was observed—in particular the allocation of excess valence band holes into the two midgap radical hole states. This was evidenced by the increasing signal magnitude at 400 nm, the linear increase in the integrated amplitude of the broadband signal (with an identical slope to the 400 nm increase), and the transformation of the first SVD component's eigenkinetics into the 400 nm kinetic trace all under increasingly positive bias. The eigenspectrum was observed to blueshift as well, by approximately 0.7 eV, indicating a change in the dominant hole species being probed. The observed redistribution of charges to surface sites was in agreement with previous results at 800 nm, which displayed the rapid, voltage-dependent decay of valence band holes to (an) unknown species [8], and the generalized scheme of electron transfer in Marcus

theory, for which the free energy $\Delta G$ of the hole transfer reaction is probably increased with applied bias.

Under open circuit conditions, the 400 nm probe signal was observed to saturate above 20% surface excitation, suggesting that a limited number of surface sites existed for both radical hole species. Unusually, under an applied bias of 0 V, the 400 nm signal did not appear to saturate with fluence, suggesting that the density of accessible surface states increases. The growth in the 400 nm emissive signal tracked linearly with the photocurrent as well, implying a correlation between the addition of surface sites and (the flow of) charge at the surface. Voltage-dependence measurements at fixed fluence also revealed a linear growth of these surface radicals. At present, mechanism for creating additional surface sites and accommodating high concentrations of radical species is unclear. However, the number of accessible surface sites appears to be linear with respect to both current and voltage.

Given their coexistence on the picosecond timescale—and unless the second hole species is a subsequent intermediate of the oxyl radical—it is likely that the two radical hole species will compete for these sites. Interestingly, for both the voltage-dependent measurements at a fluence of 0.06 mJ/cm$^2$ and the fluence dependence measurements at 0 V, the monochromatic kinetic profile remained the same. Consequently, the population ratio of the two radical hole species to one another must have also remained constant under the application of voltage. Given that the a fixed number of surface sites exists for the 0 V condition, the constant ratio suggests that the number of surface holes generated—even at the highest fluences—is still less than the number of surface sites open. Furthermore, the fixed ratio also indicates that the competition between the two surface radicals isolated in the 400 nm trace is not particularly dominant at low pump fluences. A precise molecular description of the second radical species would be extremely informative in clarifying the nature of its competition with the titanium-oxyl radical for surface sites.

### 4.5.3 Future Work: Identifying the (Multiple?) Active Species

The number of active surface sites is widely considered to be one of the critical parameters for water oxidation performance. [36–41] However, it is not clear how many surface sites are occupied by a radical species and further which of these two surface states, if not both, is the most relevant to oxygen evolution. Now that signatures for several radical hole species have been identified, additional experiments are necessary to evaluate the population distribution of each hole species as well as their involvement in the oxidation mechanism. Further investigation is also required to clarify the molecular form of the second distorted radical species observed in the 400 nm kinetics and its relationship—competitive or otherwise—with respect to the oxyl radical.

At present, there is insufficient information to estimate the absolute, or even the relative, distribution of holes between the three states under different voltages. The initial density of states for the valence band holes at open circuit is expected to be larger than that of both surface hole states under open circuit; yet it is apparent that the density of surface states changes under voltage. Furthermore, it is difficult to generate estimates of relative

populations based on the optical signatures alone. The strength of the transition dipole moments will vary for each hole species and will affect the observed signal magnitudes; therefore, the signal amplitudes are not directly reflective of excited state hole populations. While theoretical calculations of transition dipole moments have been conducted, as shown earlier, and may help to resolve this ambiguity, the undetermined molecular form of the second radical hole species precludes this level of quantitation.

Even after the issue of relative populations is settled, the question of each state's catalytic activity must be addressed. It is possible that one of these surface radical species may only contribute to the photocurrent and not correlate to the actual evolution of oxygen gas—a quantity that is not measured under our current set-up. In such a case, it would not be unreasonable, however unlikely, for the lesser populated hole species to drive the majority of water oxidation. Alternatively, the two states may also drive different oxidation pathways simultaneously. If two water oxidation mechanisms are, in fact, simultaneously operative for a certain voltage, it becomes more difficult to distinguish a relationship between external quantum efficiency and the active species. With distinctive signatures for both hole species in the visible, however, it should be possible to track the evolution of both states out to longer times under traditional nanosecond transient absorption measurements in the visible and discriminate their respective reactivities.

## 4.6 Conclusion

Transient optical reflectance experiments on niobium-doped strontium titanate single crystals (001) were conducted under several conditions including variable fluence, voltage, polarization and hole-scavenging molecules. The optical probes of monochromatic 400 nm and a broadband white light spectrum (450-700 nm) were explicitly chosen to investigate the existence of midgap radical hole species at the solid-liquid interface. In addition to valence band holes, the electronic transitions of two surface-bound hole states were identified. From the observed results, the surface hole species were assigned to an titanium-oxyl radical (with possible contributions from a lateral hole) and an unidentified, distorted hole state, both of which might serve as oxygen evolution intermediates. Under an applied voltage, the distribution of holes was found to shift substantially away from valence band hole states towards increasing populations of surface radical species, though the ratio of the two surface hole species remained constant under all examined voltages. As previously mentioned, the difficulty in examining the water oxidation mechanism in heterogeneous systems is largely due to the synchronous species that exist at the solid-liquid interface. Although it is not clear how many of each (surface) hole species exists under a certain set of conditions and which of these species may contribute to the water oxidation mechanism of $SrTiO_3$, the identification of unique kinetic and spectral signatures for these states within a broadband optical window enables future measurements that track their evolution and reactivity out to longer timescales for catalytic bond formation.

# References


(1) Nakamura, R.; Okamura, T.; Ohashi, N.; Imanishi, A.; Nakato, Y. Molecular Mechanisms of Photoinduced Oxygen Evolution, PL Emission, and Surface Roughening at Atomically Smooth (110) and (100) n-$TiO_2$ (Rutile) Surfaces in Aqueous Acidic Solutions. *Journal of the American Chemical Society* **2005**, *127*, 12975–12983.

(2) Tang, J.; Durrant, J. R.; Klug, D. R. Mechanism of Photocatalytic Water Splitting in $TiO_2$ Reaction of Water with Photoholes, Importance of Charge Carrier Dynamics, and Evidence for Four-Hole Chemistry. *Journal of the American Chemical Society* **2008**, *130*, 13885–13891.

(3) Maeda, K.; Domen, K. Photocatalytic Water Splitting: Recent Progress and Future Challenges. *Journal of Physical Chemistry Letters* **2010**, *1*, 2655–2661.

(4) Kasinski, J.; Gomez-Jahn, L. A.; Faran, K.; Gracewski, S.; Miller, R. D. Picosecond Dynamics of Surface Electron Transfer Processes: Surface Restricted Transient Grating Studies of the n-$TiO_2$/$H_2O$ Interface. *Journal of Chemical Physics* **1989**, *90*, 1253–1269.

(5) Lantz, J. M.; Corn, R. M. Time-Resolved Optical Second Harmonic Generation Measurements of Picosecond Band Flattening Processes at Single Crystal $TiO_2$ Electrodes. *Journal of Physical Chemistry* **1994**, *98*, 9387–9390.

(6) Cowan, A. J.; Barnett, C. J.; Pendlebury, S. R.; Barroso, M.; Sivula, K.; Grätzel, M.; Durrant, J. R.; Klug, D. R. Activation Energies for the Rate-Limiting Step in Water Photooxidation by Nanostructured $\alpha$-$Fe_2O_3$ and $TiO_2$. *Journal of the American Chemical Society* **2011**, *133*, 10134–10140.

(7) Huang, Z.; Lin, Y.; Xiang, X.; Rodríguez-Córdoba, W.; McDonald, K. J.; Hagen, K. S.; Choi, K.-S.; Brunschwig, B. S.; Musaev, D. G.; Hill, C. L., et al. In situ Probe of Photocarrier Dynamics in Water-Splitting Hematite ($\alpha$-$Fe_2O_3$) Electrodes. *Energy & Environmental Science* **2012**, *5*, 8923–8926.

(8) Waegele, M. M.; Chen, X.; Herlihy, D. M.; Cuk, T. How Surface Potential Determines the Kinetics of the First Hole Transfer of Photocatalytic Water Oxidation. *Journal of the American Chemical Society* **2014**, *136*, 10632–10639.

(9) Imanishi, A.; Fukui, K.-I. Atomic-Scale Surface Local Structure of $TiO_2$ and Its Influence on the Water Photooxidation Process. *Journal of Physical Chemistry Letters* **2014**, *5*, 2108–2117.

(10) Imanishi, A.; Okamura, T.; Ohashi, N.; Nakamura, R.; Nakato, Y. Mechanism of Water Photooxidation Reaction at Atomically Flat $TiO_2$ (Rutile)(110) and (100) Surfaces: Dependence on Solution pH. *Journal of the American Chemical Society* **2007**, *129*, 11569–11578.

(11) Karczewski, J.; Riegel, B.; Gazda, M.; Jasinski, P.; Kusz, B. Electrical and Structural Properties of Nb-Doped $SrTiO_3$ Ceramics. *Journal of Electroceramics* **2010**, *24*, 326–330.

(12) Ricci, D.; Bano, G.; Pacchioni, G.; Illas, F. Electronic Structure of a Neutral Oxygen Vacancy in $SrTiO_3$. *Physical Review B* **2003**, *68*, 224105.

(13) Marshall, M. S.; Newell, D. T.; Payne, D. J.; Egdell, R. G.; Castell, M. R. Atomic and Electronic Surface Structures of Dopants in Oxides: STM and XPS of Nb-And La-Doped $SrTiO_3$ (001). *Physical Review B* **2011**, *83*, 035410.

(14) Rodenbücher, C.; Wicklein, S.; Waser, R.; Szot, K. Insulator-to-Metal Transition of $SrTiO_3$:Nb Single Crystal Surfaces Induced by $Ar^+$ Bombardment. *Applied Physics Letters* **2013**, *102*, 101603.

(15) Zhang, S.; Guo, D.; Wang, M.; Javed, M. S.; Hu, C. Magnetism in $SrTiO_3$ Before and After UV Irradiation. *Applied Surface Science* **2015**, *335*, 115–120.

(16) Plaza, M.; Huang, X.; Ko, J.; Brock, J. D.; Shen, M.; Simpson, B. H.; Rodríguez-López, J.; Ritzert, N. L.; Abruña, H. D.; Letchworth-Weaver, K., et al. Structure of the Photo-Catalytically Active Surface of $SrTiO_3$. *arXiv preprint arXiv:1508.01220* **2015**.

(17) Van Benthem, K.; Elsässer, C.; French, R. Bulk Electronic Structure of $SrTiO_3$: Experiment and Theory. *Journal of Applied Physics* **2001**, *90*, 6156–6164.

(18) Guo, X.; Chen, X.; Lu, W. Optical Properties of Nb-Doped $SrTiO_3$ from First Principles Study. *Solid State Communications* **2003**, *126*, 441–446.

(19) Takizawa, M.; Maekawa, K.; Wadati, H.; Yoshida, T.; Fujimori, A.; Kumigashira, H.; Oshima, M. Angle-Resolved Photoemission Study of Nb-Doped $SrTiO_3$. *Physical Review B* **Mar. 2009**, *79*, 113103.

(20) Johnson, P. J.; Prokhorenko, V. I.; Miller, R. D. Stable UV to IR Supercontinuum Generation in Calcium Fluoride with Conserved Circular Polarization States. *Optics Express* **2009**, *17*, 21488–21496.

(21) Van Stokkum, I. H.; Larsen, D. S.; van Grondelle, R. Global and Target Analysis of Time-Resolved Spectra. *Biochimica Biophysica Acta* **2004**, *1657*, 82–104.

(22) Cuk, T.; Weare, W. W.; Frei, H. Unusually Long Lifetime of Excited Charge-Transfer State of All-Inorganic Binuclear $TiOMn^{II}$ Unit Anchored on Silica Nanopore Surface. *Journal of Physical Chemistry C* **2010**, *114*, 9167–9172.

(23) Soo, H.; Macnaughtan, M.; Weare, W. W.; Yano, J.; Frei, H. EXAFS Spectroscopic Analysis of Heterobinuclear TiOMn Charge-Transfer Chromophore in Mesoporous Silica. *Journal of Physical Chemistry C* **2011**, *115*, 24893–24905.

(24) Kan, D.; Terashima, T.; Kanda, R.; Masuno, A.; Tanaka, K.; Chu, S.; Kan, H.; Ishizumi, A.; Kanemitsu, Y.; Shimakawa, Y., et al. Blue-Light Emission at Room Temperature from $Ar^+$-Irradiated $SrTiO_3$. *Nature Materials* **2005**, *4*, 816–819.

(25) Yasuda, H.; Kanemitsu, Y. Dynamics of Nonlinear Blue Photoluminescence and Auger Recombination in $SrTiO_3$. *Physical Review B* **2008**, *77*, 193202.

(26) Longo, V.; De Figueiredo, A.; de Lazaro, S.; Gurgel, M.; Costa, M.; Paiva-Santos, C.; Varela, J. A.; Longo, E.; Mastelaro, V.; Vicente, F. S. d., et al. Structural Conditions That Lead to Photoluminescence Emission in $SrTiO_3$: An Experimental and Theoretical Approach. *Journal of Applied Physics* **2008**, 11.

(27) Xu, W.; Yang, J.; Bai, W.; Tang, K.; Zhang, Y.; Tang, X. Oxygen Vacancy Induced Photoluminescence and Ferromagnetism in $SrTiO_3$ Thin Films by Molecular Beam Epitaxy. *Journal of Applied Physics* **2013**, *114*, 154106.

(28) Pendlebury, S. R.; Barroso, M.; Cowan, A. J.; Sivula, K.; Tang, J.; Grätzel, M.; Klug, D.; Durrant, J. R. Dynamics of Photogenerated Holes in Nanocrystalline $\alpha$-$Fe_2O_3$ Electrodes for Water Oxidation Probed by Transient Absorption Spectroscopy. *Chemical Communications* **2011**, *47*, 716–718.

(29) Herlihy, D. M.; Waegele, M. M.; Chen, X.; Pemmaraju, C. D.; Prendergast, D.; Cuk, T. Uncovering the Oxyl Radical of Photocatalytic Water Oxidation by Its Sub-Surface Vibration. *Nature Chemistry* **2016**.

(30) McGuire, J. A.; Shen, Y. R. Ultrafast Vibrational Dynamics at Water Interfaces. *Science* **2006**, *313*, 1945–1948.

(31) Steinel, T.; Asbury, J. B.; Zheng, J.; Fayer, M. Watching Hydrogen Bonds Break: A Transient Absorption Study of Water. *Journal of Physical Chemistry A* **2004**, *108*, 10957–10964.

(32) Stoneham, A. M. Electronic and Defect Processes in Oxides. The Polaron in Action. *IEEE Transactions on Dielectrics and Electrical Insulation* **Oct. 1997**, *4*, 604–613.

(33) Brivio, S.; Polli, D.; Crespi, A.; Osellame, R.; Cerullo, G.; Bertacco, R. Observation of Anomalous Acoustic Phonon Dispersion in $SrTiO_3$ by Broadband Stimulated Brillouin Scattering. *Applied Physics Letters* **2011**, *98*, 1907.

(34) Shayduk, R.; Herzog, M.; Bojahr, A.; Schick, D.; Gaal, P.; Leitenberger, W.; Navirian, H.; Sander, M.; Goldshteyn, J.; Vrejoiu, I., et al. Direct Time-Domain Sampling of Subterahertz Coherent Acoustic Phonon Spectra in $SrTiO_3$ Using Ultrafast X-Ray Diffraction. *Physical Review B* **2013**, *87*, 184301.

(35) Chen, J.; Li, Y.-F.; Sit, P.; Selloni, A. Chemical Dynamics of the First Proton-Coupled Electron Transfer of Water Oxidation on $TiO_2$ Anatase. *Journal of the American Chemical Society* **2013**, *135*, 18774–18777.

(36) Bak, T.; Li, W.; Nowotny, J.; Atanacio, A. J.; Davis, J. Photocatalytic Properties of $TiO_2$: Evidence of the Key Role of Surface Active Sites in Water Oxidation. *Journal of Physical Chemistry A* **2015**, *119*, 9465–9473.

(37) Friebel, D.; Louie, M. W.; Bajdich, M.; Sanwald, K. E.; Cai, Y.; Wise, A. M.; Cheng, M.-J.; Sokaras, D.; Weng, T.-C.; Alonso-Mori, R., et al. Identification of Highly Active Fe Sites in (Ni, Fe) OOH for Electrocatalytic Water Splitting. *Journal of the American Chemical Society* **2015**, *137*, 1305–1313.

(38) Kudo, A.; Miseki, Y. Heterogeneous Photocatalyst Materials for Water Splitting. *Chemical Society Reviews* **2009**, *38*, 253–278.

(39) Bell, A. T. The Impact of Nanoscience on Heterogeneous Catalysis. *Science* **2003**, *299*, 1688–1691.

(40) Nowotny, J.; Bak, T.; Nowotny, M.; Sheppard, L. $TiO_2$ Surface Active Sites for Water Splitting. *Journal of Physical Chemistry B* **2006**, *110*, 18492–18495.

(41) Nørskov, J. K.; Bligaard, T.; Hvolbæk, B.; Abild-Pedersen, F.; Chorkendorff, I.; Christensen, C. H. The Nature of the Active Site in Heterogeneous Metal Catalysis. *Chemical Society Reviews* **2008**, *37*, 2163–2171.

# Chapter 5

# Ambient Pressure X-Ray Photoelectron Spectroscopy of Water Adsorption on Strontium Titanate (001)

## 5.1 Abstract

The (001) surface of $SrTiO_3$ was characterized through ambient pressure x-ray photoelectron spectroscopy (APXPS) with water. Isobaric ambient pressure x-ray photoelectron spectra of three niobium-doped strontium titanate single crystals—as-received, $TiO_2$-terminated, roughened—and one undoped strontium titanate single crystal were collected to investigate the roles of surface termination and defects, dopants, and photoelectrochemical roughening in wetting behavior. In the near future, a detailed, quantitative analysis will be carried out such that measurements across the different samples can be compared and the effects of each variable can be distinguished. The methodology for APXPS data processing (removal of adventitious carbon contaminants, peak fitting procedures), the subsequent analysis that will be applied, and the information that can be extracted from the analysis are described. Potential changes in the wetting behavior of the four samples that could be revealed by the analysis are discussed.

## 5.2 Introduction

Due to the interfacial nature of its many applications, much effort has been focused on identifying the surface structure of $SrTiO_3$ [1–4] and establishing the relationship of its structure to the desired chemical and electrical properties. Indeed, strontium titanate shows a great variety of surface reconstructions under different treatments, complicating studies of structure-activity relationships. [5, 6] As examples of interesting sample treatments, both

photoillumination and applied voltage have been demonstrated to change the surface of $SrTiO_3$. Zhang *et al.* were able to introduce oxygen vacancies through ultraviolet excitation, as shown by x-ray photoelectron measurements. [7] Similarly, a recent x-ray absorption study by Plaza *et al.* revealed that the surface of a $TiO_2$-terminated strontium titanate sample was converted to anatase titanium dioxide over the course of electrochemical operation. [8] Such alterations in electronic structure and surface morphology may produce drastic changes in the behavior of a material at an interface. The surface sensitivity of photoelectron measurements combined with the atomic specificity of x-rays provide an ideal means to probe the electronic structure of reactive surface species in polyatomic solid state systems such as strontium titanate. For this reason, $SrTiO_3$ has been studied extensively with x-ray photoelectron spectroscopy (XPS) over the last two decades, showing the effects of various sample preparation methods on the surface and the correlations to its surface chemistry. [3, 9–11]

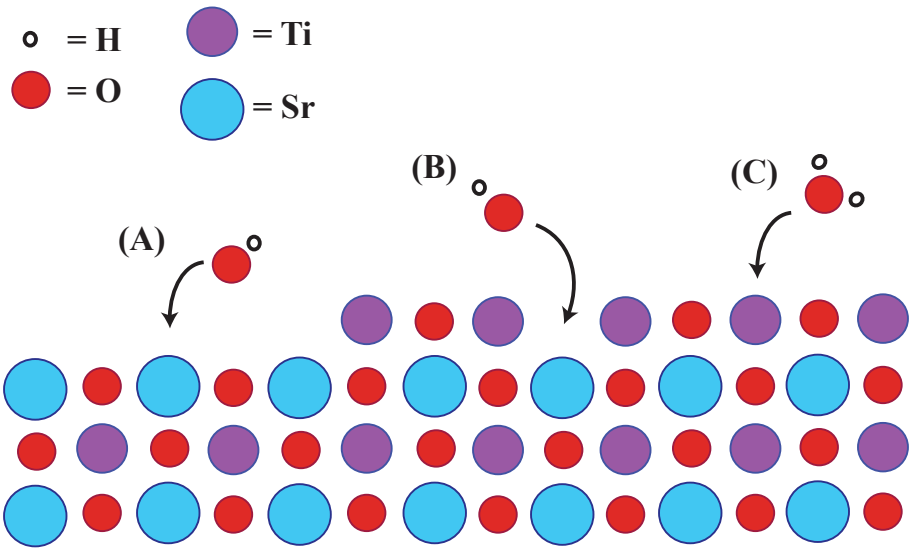


Figure 5.1: Schematic of the $SrTiO_3$ (001) face showing both (a,b) hydroxylation (dissociative adsorption), and (c) molecular adsorption of water. Both (a) surface strontium oxide and (b) oxygen vacancies are believed to be hydroxyl adsorption sites; (c) molecular water coordinates to a surface titanium atom.

The wetting behavior of the strontium titanate (001) face is of particular interest due the material's potential as a water oxidation photocatalyst. Water adsorption has recently been investigated in a number of useful metal oxide systems, including titanium dioxide [12], iron oxide [13], magnesium oxide [14], and lanthanum cobalt oxide [15], by synchrotron-based ambient pressure x-ray photoelectron spectroscopy (APXPS). The gradual transition from

laboratory-scale x-ray experiments to synchrotron-based measurements [16, 17] has resulted in higher x-ray photon fluxes for detection and, consequently, higher vapor pressures up to several torr, through which the sample can be probed. [18] Examination of the wetting properties of oxide surfaces under ambient conditions provides a deeper understanding of the catalyst as it may behave at a solid-liquid interface. Although water oxidation occurs in a condensed phase system, ambient pressure x-ray experiments can be informative in describing the types of interactions that the catalyst surface has with water, determining the energetics of those interactions, and providing insight into the surface reactivity as it might influence catalytic efficiency. In addition, when several different treatments are applied to a material, as has been done here, APXPS measurements may reveal unusual changes in the propensity of a surface to bind water associatively (hydration) and dissociatively (hydroxylation).

Ambient pressure x-ray photoelectron spectroscopic experiments are undertaken in this chapter for two purposes: (1) to establish a generalized water adsorption scheme for the (001) surface of strontium titanate and (2) to differentiate contributions from dopants, SrO and $TiO_2$ terminations, and surface roughening to the binding mechanism. The scheme of water adsorption on $SrTiO_3$ (001) is expected to follow that of its close relative, titanium dioxide, and will be compared to a previous ambient pressure study on the (110) surface of $TiO_2$. [12] In our investigation of surface terminations, strontium oxide moieties are expected contribute significantly to the preferential binding of hydroxyl groups versus water in mixed SrO:$TiO_2$ surfaces on $SrTiO_3$. Similarly, the additional surface charge introduced by n-type doping (0.1 wt. % Nb) may produce different adsorption energetics between the undoped and doped samples as a result of charge equilibration with the adsorbed electrolyte and solvent molecules. Roughened $SrTiO_3$ is anticipated to show any number of changes in its wetting behavior, including alterations in the hydroxylation:hydration ratio, the number of total adsorption sites, the types of adsorption sites, and the associated energetics of each site. In the near future, the ambient pressure x-ray photoelectron data that are shown here will undergo processing (removal of contamination contributions, peak fitting) and a quantitative analysis—all of which will be detailed below—to provide information on surface coverage, preferential dissociative (versus associative) binding, onset temperatures and corresponding relative humidities. Experimental results will also be combined with molecular dynamics simulations to compare the different lineshapes of the three unroughened $SrTiO_3$ samples—due to the difficulty in modeling the irregular surface of the roughened sample—in ambient pressure conditions with the lineshapes from APXPS measurements of $TiO_2$ (110).

## 5.3 Experimental Methods

### 5.3.1 Sample Preparation

Undoped and niobium-doped (0.1 wt. %) strontium titanate ($SrTiO_3$ and n-$SrTiO_3$) single crystals were purchased from MTI Corp. (Richmond, CA). Crystals with an exposed (001) facet were selected to simplify analysis of the surface behavior—limiting the surface to large

domains of $TiO_2$ or SrO termination—in addition to complementing previous work from *in situ* transient optical reflectance measurements on the same face. Samples labeled as "as-received" were utilized for measurements without any prior surface preparation or modification, unless otherwise noted. The as-received samples are expected to present mixed $TiO_2$ and SrO terminations at a 7:3 ratio, as determined in previous studies. [19] The $TiO_2$-terminated undoped and n-type $SrTiO_3$ samples were generated by subjecting the corresponding as-received samples to a known preparation involving a buffered hydrofluoric acid etch and subsequent annealing procedure (900 degrees Celsius) under oxygen atmosphere. [20–24] The acidic medium solubilizes strontium oxide more readily than titanium oxide species on the surface, leaving surfaces of $TiO_2$ exposed; annealing in an oxygen environment allows the surface to reequilibrate to an atomically flat crystal face. [24] To produce "roughened" samples for ambient pressure XPS measurements, as-received crystals were placed under an applied bias of +0.5 V vs. Ag/AgCl in 0.1 M NaOH solution and illuminated with 266 nm light for approximately 15 min. The roughened samples employed for static XPS measurements were taken from the set of samples used previously in transient optical reflectance measurements.

### 5.3.2 Monochromatic Static X-Ray Photoelectron Spectroscopy and Valence Band Measurements

Static x-ray photoelectron and valence band edge measurements on as-received and roughened n-$SrTiO_3$ were carried out by Dr. Ian Sharp at the Joint Center for Artificial Photosynthesis at Lawrence Berkeley National Laboratory. X-ray photoelectron measurements were conducted with a monochromatized Al K$\alpha$ source ($h\nu$ = 1486.6 eV), operated at 225 W, on a Kratos Axis Ultra DLD system at a takeoff angle of 0 degrees relative to the surface normal, and a pass energy of 160 eV and 20 eV for wide scan spectra and valence band scans, respectively. Due to charging, data for undoped strontium titanate samples could not be obtained. The XPS spectra were calibrated by the observed work function for a piece of gold foil.

### 5.3.3 Ambient Pressure X-Ray Photoelectron Spectroscopy

Ambient pressure XPS Experiments were carried out at beamline 11.0.2 of the Advanced Light Source at Lawrence Berkeley National Laboratory. Two separate chambers were utilized—one for surface preparation (i.e., cleaning) and an adjacent chamber for ambient pressure x-ray photoelectron measurements. Both chambers were maintained at pressures on the order of $10^{-8}$- $10^{-10}$ torr, with the exception of the high pressure chamber during ambient pressure experiments.

For ambient pressure measurements, all samples were first heated in the preparation chamber under an ultrahigh vacuum environment at 600-700 degrees Celsius in order to remove adventitious carbon contaminants on the sample surfaces. [25] Previous studies on $SrTiO_3$ have shown no substantial surface rearrangement or damage upon heating to 650

degrees Celsius in a vacuum environment. [26] Annealing in oxygen atmospheres [2, 27] and argon sputtering [9, 10, 28–30] are two alternative methods commonly utilized to facilitate the removal of carbon contaminants. However, these conditions were actively avoided during surface preparation to prevent reconstruction or depletion of surface defect states in the $TiO_2$-terminated and roughened samples.

Samples were initially monitored for x-ray damage over successive scans. In as-received n-$SrTiO_3$, x-ray damage manifested in the form of dehydroxylation at high temperatures under 0.1 torr of water. In the undoped $SrTiO_3$ sample, no dehydroxylation was observed; however, charging effects resulted in a constant kinetic energy offset across all edges that increased as the temperature was reduced. The spectra shown here were collected each at a different position on the sample surface to minimize the effects of dehydroxylation. As a result of spot-to-spot variation in carbon contamination, the oxygen edge spectra contain varying amounts of carbonate contaminants; carbon 1s spectra were periodically collected to enable quantification of carbon contaminants in the oxygen spectra. Prior to APXPS experiments, millipore $H_2O$ was degassed with three freeze-pump-thaw cycles; we note that this procedure does not remove carbonate ions within the water. Four samples were analyzed under APXPS conditions including undoped $TiO_2$-terminated $SrTiO_3$, n-doped $TiO_2$-terminated $SrTiO_3$, as-received n-doped $SrTiO_3$, and roughened n-doped $SrTiO_3$. A minimum of three isobar measurements were collected for each sample at 0.03 and 0.1 Torr, and either 0.008 or 0.5 Torr. The undoped $SrTiO_3$ sample was not analyzed under the lowest pressure conditions due to overwhelming charging effects at increasingly low temperatures. For the preliminary analysis conducted here, only the spectra collected at 0.1 torr were considered. Future work to determine the thermodynamics of hydroxylation and liquid water adsorption on strontium titanate will take all three isobaric data sets for each sample into account. These will be compared on an a scale of relative humidity—$\mathrm{RH} = p/p_v(\mathrm{T}) \times 100\%$, where $p$ is the experimental pressure and $p_v$ is the equilibrium vapor pressure at the experimental temperature T.

Spectra at the O 1s, Ti 2p, Sr 3d, C 1s/Sr 3p, and Nb 3d edges were collected with a constant photon energy of 735 eV. The spectra, which have not yet been treated with a quantitative analysis, will be subjected to a multipeak fitting procedure in Igor Pro 6.3, scripted for the fitting of x-ray photoelectron spectra (XPSTools, Dr. Martin Schmid, ETH Zurich). All x-ray photoelectron spectra shown are calibrated using the principal titanium 2p photoelectron peak (binding energy, BE = 459 eV) as an internal standard, adjusted to match the literature values of the reported binding energy in $SrTiO_3$. [30] All fits will employ Voigt functions—with an initial Gaussian:Lorentzian ratio of 70:30—and a Shirley background to model the experimental data.

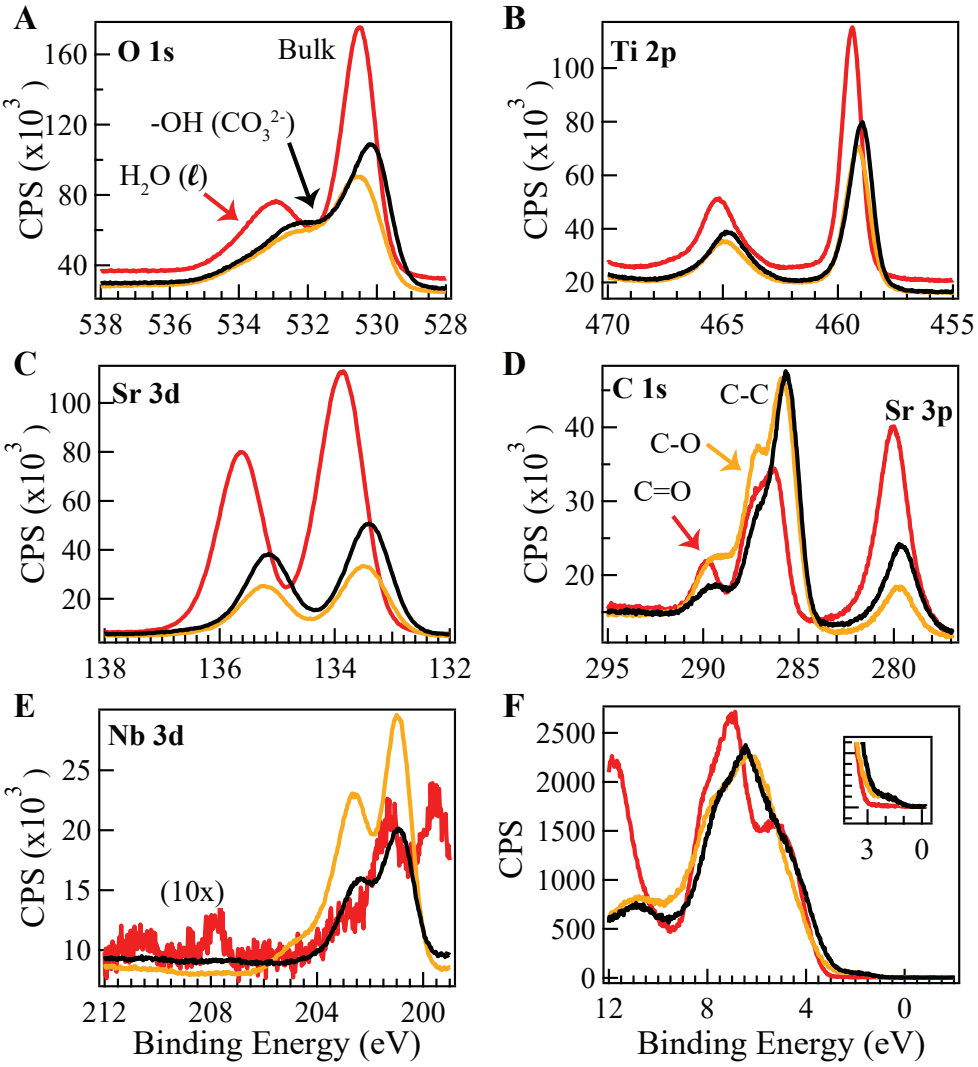


Figure 5.2: Static x-ray photoelectron spectra shown for three samples of n-$SrTiO_3$: one as-received (red) and two roughened (yellow, black). Spectra shown include the (a) oxygen 1s, (b) titanium 2p, (c) strontium 3d, (d) strontium $3p_{1/2}$ (280.3 eV) and carbon 1s (284.2 eV), and (e) niobium 3d edges. In the oxygen edge, the photoelectron contribution from bulk lattice oxygen atoms is shown; additional contributions due to hydroxyl species (or carbon contaminants) and liquid, molecular water are highlighted by arrows. At the carbon edge, contamination peaks from adventitious carbon—aliphatic (C-C), alcoholic (C-O), acidic (COOH), and carbonate ($CO_3^{2-}$)—are also identified. (f) The valence band shows drastic changes in the density of deeper states, shifts at the VB edge and the growth of midgap states (inset).

## 5.4 Results

### 5.4.1 Static X-Ray Photoelectron Spectroscopy and Valence Band Measurements

Vacuum x-ray photoemission measurements were conducted on n-doped $SrTiO_3$ to provide a foundation for later ambient pressure XPS measurements as well as to examine the effect of surface rearrangement—occurring under our experimental conditions in transient reflectance measurements (photoillumination, applied bias)—on the electronic structure of strontium titanate as well as its wetting behavior. The x-ray photoelectron spectra of the as-received (mixed $TiO_2$:SrO) sample are considered first. In the oxygen 1s edge (Fig. 5.2a, two peaks are observed at 530.5 eV and 532.95 eV. The 530.5 eV peak corresponds to electrons ejected by bulk lattice oxygen atoms, in agreement with previous XPS studies on $SrTiO_3$ and transition metal oxides in general. [31, 32] The second peak at higher binding energy is ascribed to adsorbed molecular water, $H_2O$ ($\ell$). [12, 15, 33] A small component attributable to hydroxyl species, carbonate, or both at the surface may be present but are convolved with the overlapping contributions from bulk and water-derived oxygen. The titanium edge of $SrTiO_3$ (Fig. 5.2b) displays two prominent peaks at 459.38 eV and 465.2 eV, each corresponding to the expected transitions of photoelectrons from the respective titanium $2p_{3/2}$ and $2p_{1/2}$ orbitals. [34] Similarly, in Fig. 5.2c, the strontium 3d edge reveals two photoelectron transitions at 133.85 eV and 135.62 eV. In Fig. 5.2d, both the strontium $3p_{1/2}$ and the carbon 1s edges are shown; the recorded spectral window excludes the second $3p_{3/2}$ transition, which will be seen in the ambient pressure measurements. The carbon edge shows two peaks centered at 286.77 eV and 289.77 eV; the peak at 286.77 eV is, in fact, a convolution of two peaks. These contributions to the carbon edge have been previously identified as adventitious carbon contaminants on the sample surface, arising from aliphatic carbon (C-C), alcoholic and carboxylic acid carbon (C-O, COOH), and carbonate carbon ($CO_3^{2-}$)—highlighted by arrows in Fig. 5.2d. The niobium 3d edge shows a very low photoelectron signal, with two peaks that agree with literature reports for their binding energies. The observation of a small signal is expected given the low concentration of niobium dopants (0.1 wt. %) in the sample. The concentration of niobium in the doped samples (0.1 wt. %) is such that only two titanium atoms out of a thousand unit cells are expected to be substituted by niobium.

| sample | O 1s | Ti $2p_{3/2}$ | Sr $3d_{5/2}$ | Sr $3p_{1/2}$ | Nb $3d_{5/2}$ |
|---|---|---|---|---|---|
| as-received | 530.50 | 459.38 | 133.85 | 280.00 | 199.53 |
| roughened (1) | 530.48 | 459.125 | 133.53 | 279.65 | 201.00 |
| roughened (2) | 530.23 | 458.93 | 133.40 | 279.73 | 200.93 |

Table 5.1: Static XPS binding energies for the as-received and roughened n-doped $SrTiO_3$ samples. All values are in electron-volts.

Lastly, in Fig. 5.2f, the valence band spectrum displays two large, convolved peaks centered at roughly 199.53 eV and 201.25 eV; an additional peak can be seen at the edge of the spectral window around 12 eV. The valence band edge is determined to be 3.0 eV, which agrees with literature values for the optical band gap (3.25 eV, indirect) with $\Delta E = 0.25$ eV. [35–38]

From static x-ray photoelectron spectroscopy measurements, very distinct shifts of the roughened sample to the as-received sample were observed (Fig. 5.2). Although the precise shift in binding energy was not constant across all recorded edges, a general trend of a shift to lower binding energies with surface roughening was observed (Fig. 5.2 and Table 5.1). The niobium 3d edge and valence band measurements were notable exceptions to this trend, for which the spectra shifted approximately 1 eV to higher binding energies in both cases. The shifts observed in all other spectra were $\Delta BE \leq$ -0.3 eV. An increase in the quantity of carbonaceous contaminants following roughening procedure was evidenced by the growth of higher energy shoulders in the oxygen and carbon 1s edges relative to the intensity of the lattice oxygen 1s and strontium 3p peaks, respectively. The increase in carbon at the surface may not have been directly due to roughening—as the photoelectrochemical treatment is conducted in 0.1 M NaOH, in which there is expected to be very little dissolved $CO_3^{2-}$. However, the apparent increase in contamination may have indicated an increase in the predilection of the roughened sample surface to adsorb carbon contaminants during transfer from treatment conditions to the UHV chamber. Both the titanium 2p and strontium 3d spectra show no significant changes in the spectral profile other than reduced signal magnitude and the aforementioned binding energy shift. Under the same x-ray excitation depth, however, significantly higher signal magnitudes at the niobium edge are observed in the roughened samples relative to the as-received samples despite nominally identical doping concentrations. Prior studies have shown niobium atom migration to the surface and grain boundaries under high heat and oxygen, [30, 39] but not specifically through photoelectrochemical preparations. The application of positive bias under illumination also appears to have shifted the band edge ($\Delta E = 0.3$ and 0.5 eV for the two samples). Furthermore, the photoelectrochemical treatment induced new defect states near the valence band edge (Fig. 5.2f, inset), extending the band edge approximately 2 eV into the gap but with a small density of associated states. There were no apparent defect $Ti^{3+}$ states that could be identified from the titanium 2p spectrum, corresponding to midgap states generated by the roughening process, likely as a result of the large excitation depth of the x-ray beam ($h\nu =$ 1486.6 eV) and the small density of midgap states produced.

Although the vacuum XPS measurements indicate that some amount of hydration and hydroxylation occurs on both surfaces, these static x-ray photoelectron spectra illustrate the need to conduct ambient pressure x-ray photoelectron measurements with careful control of the water environment to separate the respective contributions of liquid water and hydroxyl groups to the spectrum. Furthermore, the vacuum environment must also be controlled to mitigate contamination that could reduce the number of available adsorption sites or contribute spurious carbon-derived peaks to the XPS data. Comparison of the oxygen edges for the as-received and roughened samples does reveal a change in the ratio of $H_2O$ ($\ell$),

OH, and $CO_3^{2-}$ contaminants that exist on the surface of roughened $SrTiO_3$. However, the exact quantities of each adsorbed species and the mechanism of their adsorption cannot be determined from these measurements alone. Each oxygen spectrum presents only a single snapshot of the sample surface, without any indication of where the precise OH and $H_2O$ binding energies may sit (other than from the literature) and without providing a sense of how the surface arrived at this wetted state. Therefore, ambient pressure measurements are the logical next experiments to carry out to address these concerns and provide insight into the wetting mechanism of the $SrTiO_3$ surface.

## 5.4.2 Ambient Pressure (Static) X-Ray Photoelectron Spectroscopy

### 5.4.2.1 Titanium 2p and Strontium 3d Spectra

In the ambient pressure measurements of all four samples (Figure 5.3), two peaks corresponding to the titanium 2p $L_3$ and $L_2$ edges were observed. No lower binding energy shoulders relative to the main $2p_{3/2}$ and $2p_{1/2}$ peaks were identified in the ambient pressure experiments. These shoulders often reflect the presence of reduced titanium atoms—$Ti^{3+}$ or $Ti^{2+}$—created by niobium dopants $Nb^{5+}$ and oxygen vacancies. Due to the low concentration of dopants (0.1 wt. %) in the samples investigated, low-energy shoulders were not expected to appear in the titanium edge solely as a result of $Nb^{5+}$ atoms, as has been observed for higher dopant levels (e.g., 1.5 at. %). [40] The absence of lower binding energy shoulders also implied the absence of oxygen vacancies in the as-received and roughened n-$SrTiO_3$ samples; oxygen vacancies were not expected in the $TiO_2$-terminated samples following the oxygen-rich anneal step in the surface preparation. In both rutile titanium dioxide and strontium titanate at the (110) planes, bridging oxygen vacancies, whose concentration can be determined by corresponding concentrations of surface $Ti^{3+}$ atoms, have been proposed to act as hydroxylation sites. [12, 41] In ambient pressure x-ray photoelectron measurements on $TiO_2$ (110)—shown in Fig. 5.4a, oxygen vacancies were observed in the titanium 2p edge under ultrahigh vacuum and found to disappear as water vapor was introduced to the reaction chamber. The spectra taken on the four $SrTiO_3$ samples do not display this behavior. Therefore, there are minimal concentrations of oxygen vacancies on the mixed SrO;$TiO_2$ and roughened strontium titanate surfaces. However, we cannot completely eliminate contributions of oxygen vacancies to the titanium edge without a quantitative peak fitting. In the near future, the absence of oxygen vacancies in our $SrTiO_3$ samples will be confirmed with a detailed peak fitting.

Qualitatively, the strontium 3d spectrum does not appear to change with the variables of surface termination and dopants. These strontium 3d spectra are excluded from our current consideration but will be examined in greater detail following the proposed quantitative analysis. Previous studies have indicated the preferential binding of hydroxyl species to surface strontium atoms, evidenced by the appearance of a peak at an intermediate binding energy to both $3d_{5/2}$ and $3d_{3/2}$ peaks. [42, 43] Given previous reports of 30% SrO surface

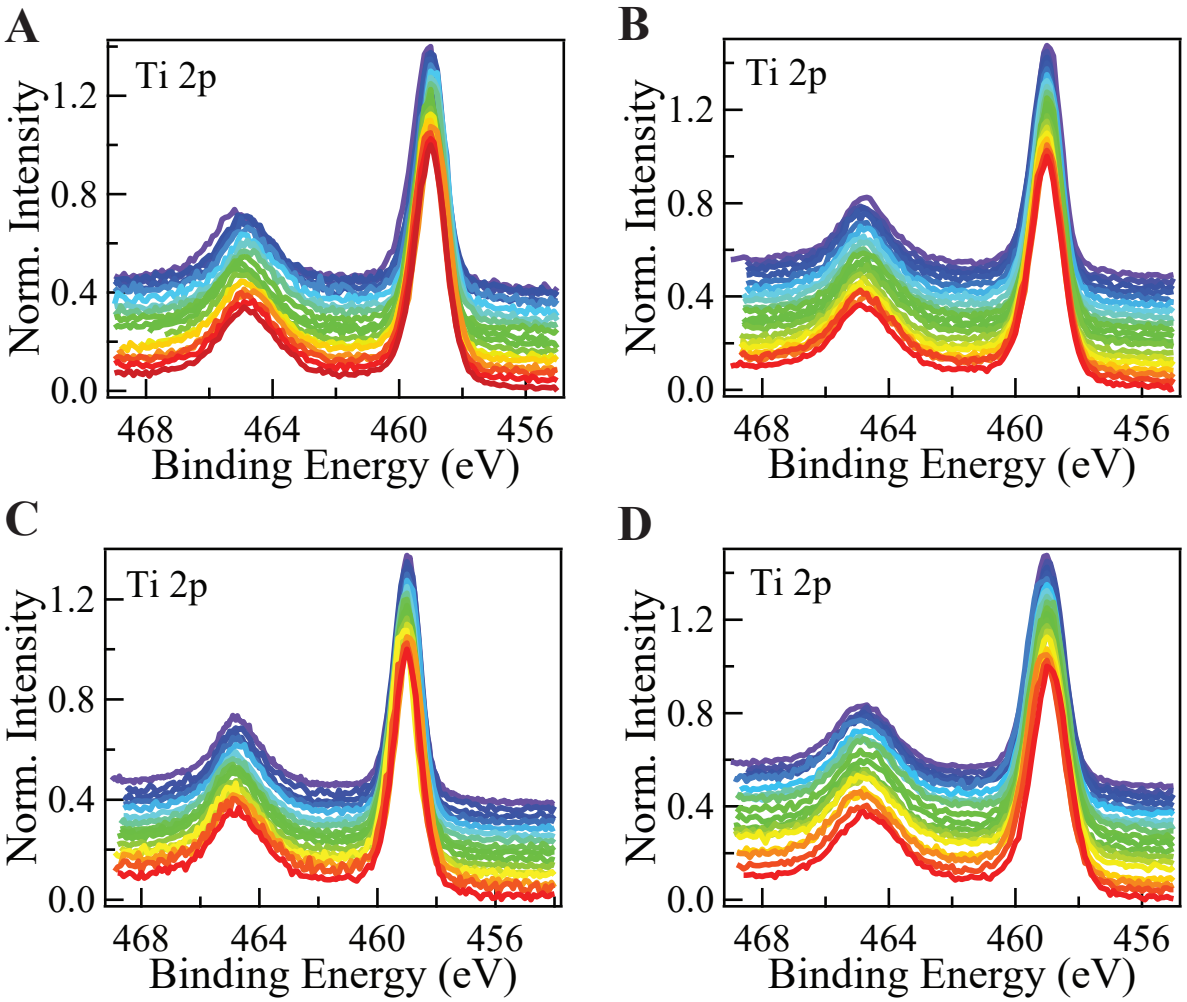


Figure 5.3: Isobaric measurements of the titanium $L_{3,2}$-edge for (a) undoped $TiO_2$-terminated $SrTiO_3$, (b) Nb-doped $TiO_2$-terminated $SrTiO_3$, (c) as-received Nb-doped $SrTiO_3$, and (d) roughened Nb-doped $SrTiO_3$, shown under 0.1 torr water. The color progression is such that the highest temperatures (up to 550 degrees Celsius) are shown in red and lowest temperatures (down to 5 degrees Celsius) are in blue.

termination on untreated surfaces, [19] a change in the Sr 3d spectrum of the $TiO_2$-terminated (n-doped) sample relative to that of the as-received sample is expected. The growth of an intermediate peak corresponding to the Sr-OH species may be more obvious following quantitative analysis in which both integrated areas and lineshapes of the spectra can be considered across the different samples.

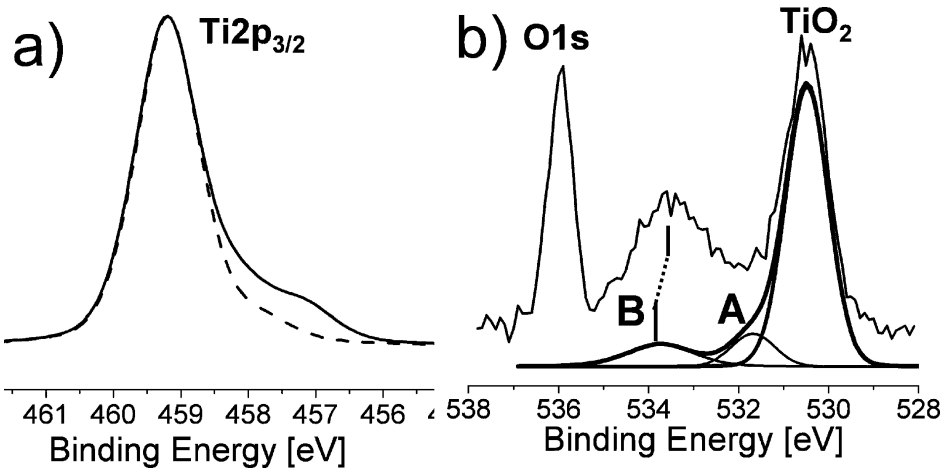


Figure 5.4: Titanium 2p and oxygen 1s ambient pressure XPS spectra taken with x-ray energy 650 eV. (a) A slight shoulder in the titanium edge attributable to oxygen vacancies ($Ti^{3+}$ and $Ti^{2+}$) was observed (solid line). The intensity of the shoulder decreased after the introduction of water, implying hydroxylation of these surface defects (dashed). (b) The oxygen edge shows contributions from bulk/lattice oxygen atoms ($TiO_2$), hydroxyl species (A), and adsorbed liquid water (B). Reprinted with permission from Ketteler *et al.* "The Nature of Water Nucleation Sites on $TiO_2$ (110) Surfaces Revealed by Ambient Pressure X-ray Photoelectron Spectroscopy", *J. Phys. Chem. C*, **2007**, *111* (23), 8278-8282. Copyright 2007 American Chemical Society. [12]

#### 5.4.2.2 Oxygen 1s Spectra

Based upon our spectra from the static XPS measurements, general measurements of transition metal oxides [31, 32], and similar ambient pressure x-ray photoelectron spectra collected for $TiO_2$ (110), [12], four principal peaks are expected in the oxygen 1s spectrum of $SrTiO_3$. As can be seen from the undoped $TiO_2$-terminated $SrTiO_3$ APXPS oxygen edge measurements (Figs. 5.5a), the undoped $TiO_2$-terminated surface shows contributions from bulk lattice oxygen atoms within the single crystal at approximately 531 eV [44, 45], from hydroxyl species centered roughly around 532 eV, from liquid water near 534 eV, and from gaseous water near 536 eV [12, 14, 15, 33]. The detection of the oxygen 1s photoelectrons derived from gaseous water is more obvious in the spectra for the remaining three samples; the intensity of the $H_2O$ (g) peak depends strongly on the distance of the electromagnetic lens tip from the sample. As the temperature is reduced, equilibrium favors the interaction of water with the $SrTiO_3$ surface; the corresponding growth of a prominent shoulder comprising adsorbed hydroxyl species and molecular water can be observed in all four samples (Fig. 5.5). The dissociative adsorption of hydroxyl species visually appears to precede the associative adsorption of liquid water though quantitative analysis—detailed below—will be required confirm this assessment. The growth of the hydroxyl species prior to the adsorp-

tion of molecular water is most evident in the n-doped $TiO_2$-terminated $SrTiO_3$ spectra. The roughened sample displayed a slight reduction in its water adsorption relative to the other three samples; the wetting behavior of the roughened sample will be addressed in the discussion.

We note that the oxygen spectra for the doped samples likely contain contributions of

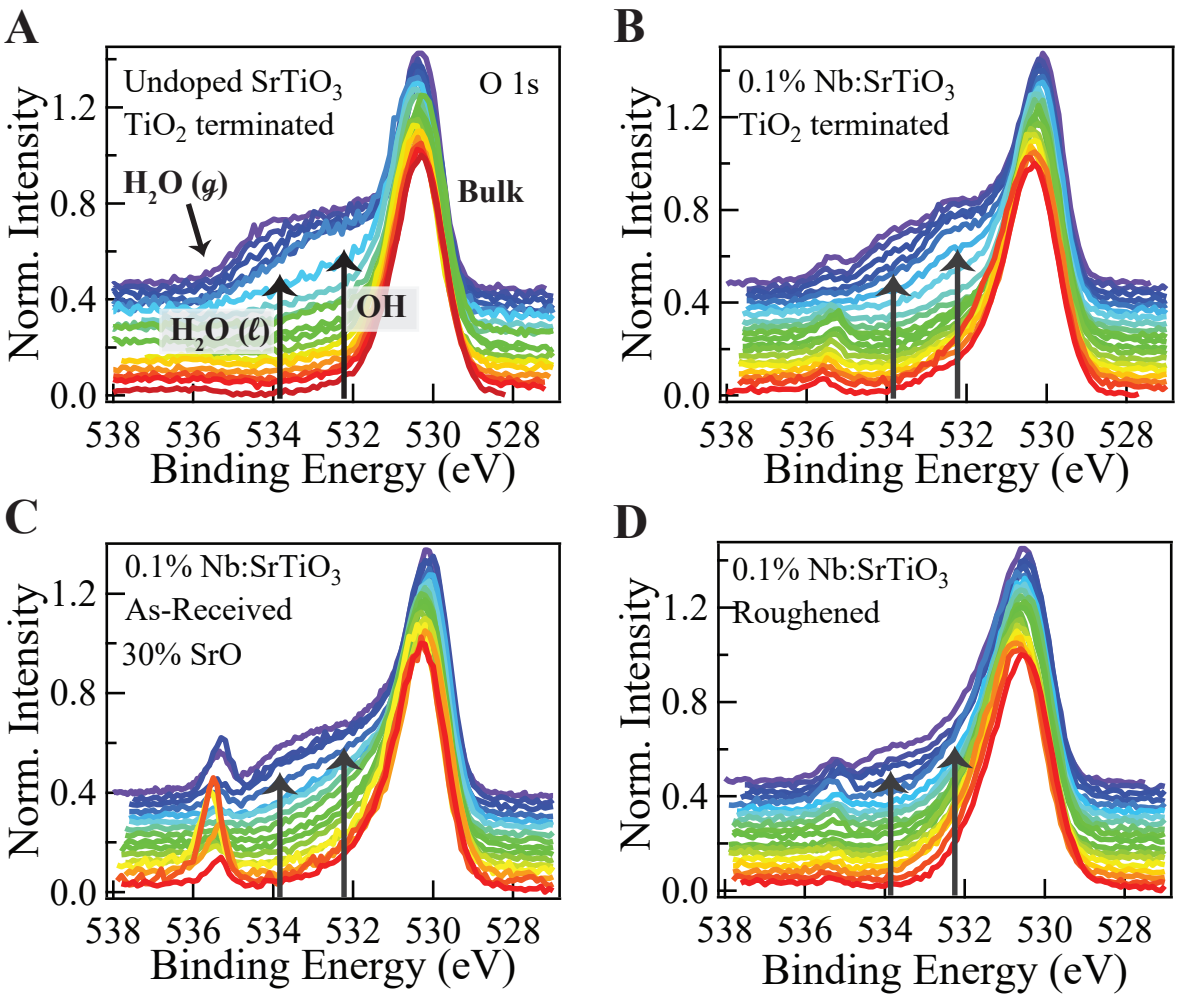


Figure 5.5: Isobaric measurements of the oxygen K-edge for (a) undoped $TiO_2$-terminated $SrTiO_3$, (b) Nb-doped $TiO_2$-terminated $SrTiO_3$, (c) as-received Nb-doped $SrTiO_3$, and (d) roughened Nb-doped $SrTiO_3$ are shown under 0.1 torr $H_2O$. The color progression is such that the highest temperatures (up to 550 degrees Celsius) are shown in red and lowest temperatures (down to 5 degrees Celsius) are in blue. The arrows indicate roughly where gaseous water, liquid water, and hydroxyl groups are expected to contribute.

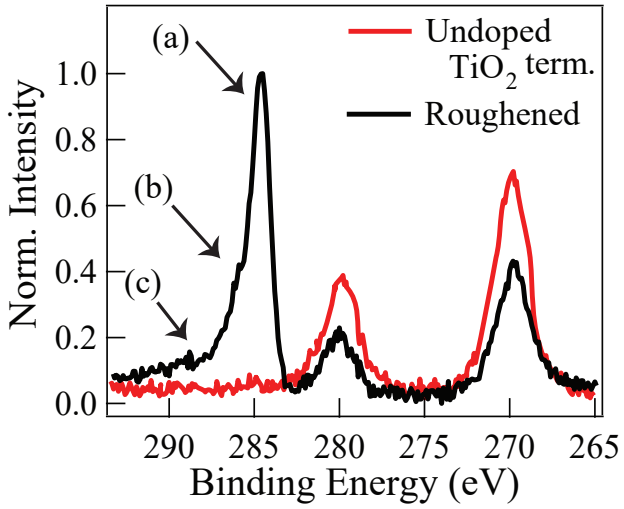


Figure 5.6: Comparison of the undoped $TiO_2$-terminated and roughened n-doped $SrTiO_3$ samples at the carbon 1s and strontium 3p edges following cleaning (UHV, 650 degrees Celsius, 30 min). The undoped $TiO_2$-terminated sample displays only contributions from the strontium; there are no carbon contaminants. In contrast, the roughened sample shows large peaks in the carbon 1s region, with (a) aliphatic (C-C), (b) alcoholic/carboxylic acid (C-O, COOH) and (c) carbonate (C=O) contributions. [46]

carbonate. The presence of carbonates on the surfaces of n-doped samples were indicated by carbon 1s spectra acquired for every fifth sample spot examined. In contrast, the undoped sample did not show any detectable concentration of either oxygenic or aliphatic contaminants in the carbon 1s spectrum (Fig. 5.6). The carbon 1s spectra for the roughened doped sample and $TiO_2$-terminated undoped sample following the cleaning procedure (UHV, 650 degrees Celsius, 30 min) are shown in Fig. 5.6. The carbon edge of the roughened sample shows contributions from aliphatic carbon (C-C) as well as oxygen-containing alcohol/carboxylic acid (C-O, COOH) and carbonate ($CO_3^{2-}$) contaminants. Carbonate-derived peaks in the oxygen edge typically appear very close to the binding energy of hydroxyl groups—approximately 532-533 eV for alcoholic oxygen species (C-O-H) and 531-532 eV for carbonyl groups (C=O). [47, 48]

In order to analyze the oxygen edge data in a quantitative manner, the removal of carbonate and carboxylic acid contributions to the oxygen spectra will be necessary before any further peak fitting, lineshape analysis or quantification of integrated areas can be conducted. As carbon edge spectra were collected periodically for the samples during data acquisition, the corresponding oxygen contributions of these contaminants can be estimated. While the correction for carbon-based contaminants has not yet been carried out for the oxygen edge data in Fig. 5.5, we describe the procedure that will be conducted in the near future. First, the carbon spectra are subjected to peak fitting analysis to discriminate the type(s) of carbon

contaminants present: aliphatic, alcoholic/carboxylic acid, and carbonate. Once the relative quantities of each carbon contaminant have been determined, the corresponding contribution to the oxygen edge is calculated. For example, the presence of a carbonate ($CO_3^{2-}$) species on the surface will contribute one carbon atom to the total carbon spectrum; in the oxygen edge, the carbonate contribution will be three times as much based on stoichiometry. In contrast, contributions from a carboxylic acid contaminant will contribute one carbon atom and two oxygen atoms to the respective edges. The accuracy of this estimate can be additionally calibrated through ambient pressure XPS measurements of carbon dioxide gas ($CO_2$) within the experimental chamber. Such calibration of the detector response could reveal that carbon dioxide, with an expected 2:1 ratio of oxygen-to-carbon, displays a 3:1 ratio instead. A carbon dioxide calibration measurement was conducted immediately following our ambient pressure measurements with water and will be incorporated into the final analysis. The removal of carbon-derived peaks from the oxygen spectra is carried out for each set of data—i.e., for all the temperatures (550 degrees Celsius $\rightarrow$ 5 degrees Celsius) recorded for each isobar (0.008, 0.03, 0.1, and 0.5 Torr).

Following the removal of carbon contaminants from the oxygen edge spectra, a wealth of information can be extracted. First and foremost, peak fitting will provide estimates for the relative quantity (integrated area) of hydroxyl groups and water on the $SrtiO_3$ surface for a given temperature and water vapor pressure. These can be converted to estimates of monolayer coverage by comparison of peak area for each species relative to the area for bulk lattice oxygens. [12, 15] The coverage is plotted for each isobar with respect to the experimental temperature, as illustrated for a similar study on titanium dioxide (110) in Fig. 5.7a. [12] The resulting graph will provide an estimate of onset temperature for both associative (hydration) and dissociative (hydroxylation) water adsorption. Alternatively, the coverage estimates can be graphed against relative humidity ($RH = p/p_v(T) \times 100\%$), as seen in Fig. 5.7c, which will enable us to compare across the different isobars and to determine the reproducibility of our data for a given sample. The energy of adsorption for the hydroxylation and hydration can also be extracted from temperature dependence plots of coverage, $ln\ p/p_v$ vs. 1/T, following the Clausius-Clapeyron equation. [12]

An additional metric that can be extracted from a quantitative analysis is the shift in the binding energy of the corresponding hydroxyl, liquid water or gaseous water peaks relative to the bulk lattice oxygen binding energy as a function of monolayer coverage. Changes in the energy difference between the two peaks will reveal the propensity of the surface to bind liquid water or hydroxyl species and whether the strength of that interaction changes with additional layers of solvent to passivate the surface. This is particularly relevant to the condensed phase aspect of water oxidation catalysis, where the interaction of the catalyst surface with water is not limited to a single monolayer but can extend out to and equilibrate with multiple layers of water. Several theoretical studies of binding interactions between water and metal oxide surfaces have shown variable ratios of dissociation and association depending upon the simulation conditions. [49–52] Indeed, preliminary molecular dynamics calculations reveal that dissociation makes up 50% of the adsorption interaction with $SrTiO_3$ (Fig. 5.8); when additional layers of water are included, the dissociated fraction drops down

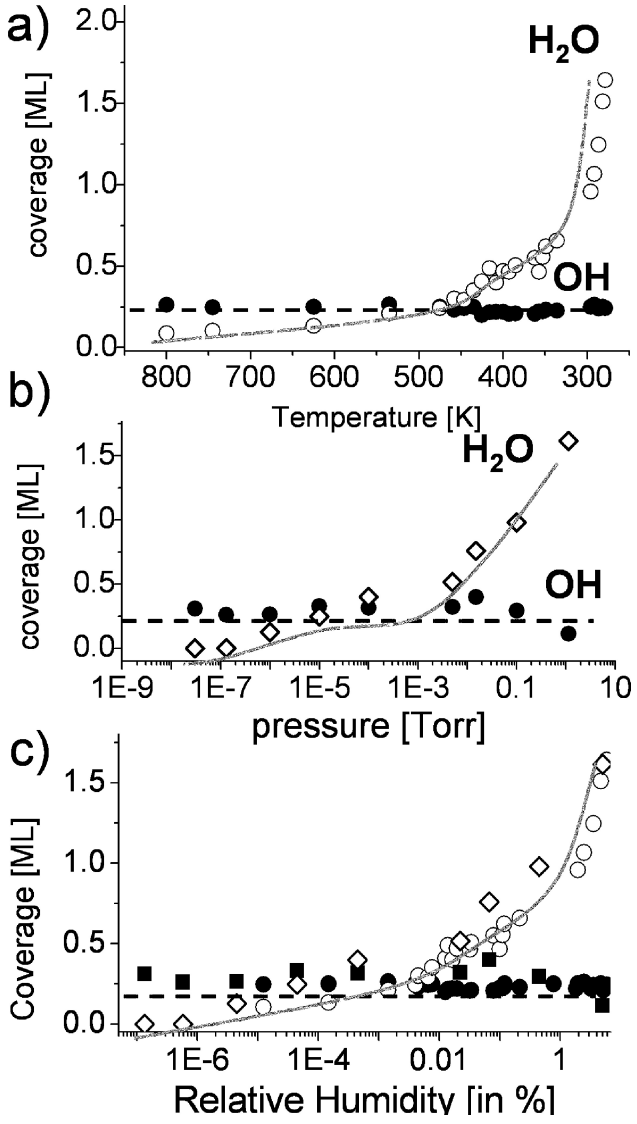


Figure 5.7: An example of monolayer coverage in a water adsorption ambient pressure x-ray photoelectron study of titanium dioxide (110). The adsorption of hydroxyl species and molecular water are plotted against (a) temperature (isotherms) and (b) ambient pressure (isobars). (c) The two sets of data converge towards the same trend in a plot of coverage versus relative humidity. Hydroxylation occurs at higher temperatures, lower pressures and lower relative humidities than hydration. After a certain threshold is achieved, the formation of a liquid water monolayer outpaces additional surface hydroxylation. Reprinted with permission from Ketteler *et al.* "The Nature of Water Nucleation Sites on $TiO_2$ (110) Surfaces Revealed by Ambient Pressure X-ray Photoelectron Spectroscopy", *J. Phys. Chem. C*, **2007**, *111* (23), 8278-8282. Copyright 2007 American Chemical Society. [12]

to 37.5%.

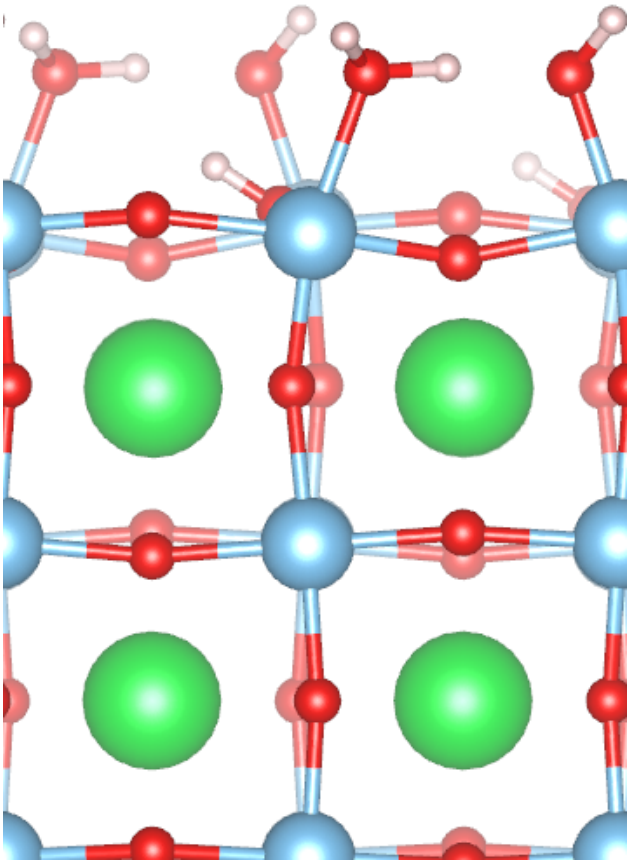

Figure 5.8: Molecular dynamics simulation of water adsorption on the $SrTiO_3$ (001) surface. The ratio of associative to dissociative adsorption shown in this image is 50:50. The calculated percentage of dissociated water (hydroxylation) was found to decrease (to 37.5%) when additional layers of molecular water were included beyond the surface.

## 5.5 Discussion

Having established approximate assignments of peaks (OH vs. $H_2O$; C-C vs. C-O vs. C=O) through static measurements, described the observed ambient pressure (Ti 2p, Sr 3d, and O 1s) spectra at 0.1 Torr, and further detailed the quantitative analysis that we intend to apply to our ambient pressure data, we now discuss some of the changes that might appear in the spectra between the different samples.

### 5.5.1 Influence of Surface Termination and Dopants on Wetting

Substantial differences in the amount of strontium oxide, titanium dioxide, and step edges at the surfaces of the as-received and $TiO_2$-terminated $SrTiO_3$ samples are anticipated. Whereas as-received samples are expected to present mixed $TiO_2$:SrO terminations at a 7:3 ratio, [19] the procedure to generate atomically flat $TiO_2$-terminated $SrTiO_3$ is widely considered to have no strontium oxide moieties on the surface. [26] It is important to note that we cannot exclude the possibility that SrO terminations may also be exposed at step edges, which are created during the etching process to generate surface $TiO_2$. [24, 53] In any case, previous studies have indicated a strong binding affinity of hydroxyls to strontium oxide on $SrTiO_3$ surfaces [43] and have attributed slight changes in the Sr 3d XPS spectrum to Sr-OH species. [42] Following a detailed peak fitting analysis, the preferential adsorption of hydroxyl species to exposed strontium on our mixed surface can manifest in our data two ways.

First, by directly comparing the strontium 3d edges of the $TiO_2$-terminated and as-received n-doped samples, a third peak corresponding to Sr-OH may be observed in our fitting analysis for the mixed $TiO_2$:SrO terminated sample but not in the $TiO_2$-terminated sample. Alternatively, Sr-OH peaks may appear in both Sr 3d spectra due to low concentrations of SrO on the etched sample; however, the 30% SrO termination on the as-received sample should result in a noticeably larger peak area. The second set of evidence for strong OH coordination to surface strontium may be extracted from our analysis of the oxygen edge. A higher occurrence of hydroxylation (OH) versus hydration ($H_2O$ ($\ell$)) in the as-received sample should be apparent in our plots of monolayer coverage against temperature or relative humidity. Furthermore, although it might not be substantial enough to distinguish, the adsorption energetics (enthalpy and entropy) of the mixed $TiO_2$:SrO surface should be slightly different from the atomically flat $TiO_2$-terminated surface, even though the majority of both surfaces comprise $TiO_2$ moieties. In the future, additional ambient pressure experiments examining SrO-terminated strontium titanate prepared by molecular beam epitaxy [54] or well-defined SrO terraces created by ultrahigh vacuum cleavage along the (001) face [4] may help to clarify the role of strontium oxide in the $SrTiO_3$ wetting behavior.

To the authors' knowledge, there are few ambient pressure XPS studies exploring the contributions of dopants to the wetting behavior of metal oxides. Niobium dopants, while too low in concentration to observed be directly at the niobium edge or as $Ti^{3+}$ in the titanium edge, may still contribute to changes in the wetting behavior of strontium titanate. Relative to the undoped ($TiO_2$-terminated) sample, the niobium atoms in the doped sample introduce significant concentrations of free carriers that can mediate the interaction of $SrTiO_3$ with surface water or hydroxyl species. The effect of these additional electrons is already evident in the inability of the undoped sample to dissipate charge at the surface and the resultant charging shifts in its x-ray photoelectron spectra under ultrahigh vacuum. The excess charge in the Nb-doped sample could affect the wetting behavior of $SrTiO_3$ in two ways. In one possible case, the extra charge could alter the fraction of dissociative binding occurring at the interface—resulting in a higher monolayer coverage of hydroxyl species relative to molecular

water, or vice versa. A second case in which the binding energy difference between the adsorbed (OH and $H_2O$) peaks with respect to the bulk lattice oxygen peak decreases for the undoped sample could be observed; this could be interpreted as evidence for a change in the local surface surroundings of the adsorbed species, with equilibration of free carriers at the interface providing an electron-rich environment. As an example, a static XPS study of pure and gadolinium-doped cerium oxide revealed a 0.5 eV shift in the molecular $H_2O$ ($\ell$) peak binding energy with respect to the lattice oxygen energy. [55]

### 5.5.2 Midgap States and Water Adsorption on a Roughened Surface

The static x-ray photoemission measurements provide substantial insight into the effect of photoelectrochemical roughening on the strontium titanate surface. While LEED patterns indicated the disappearance of periodic structure to create a reconstructed (potentially amorphous) phase on the surface of $SrTiO_3$ (Fig. 4.5), the static XPS measurements revealed that new electronic states significantly deep into the band gap evolved during the roughening process. The actual molecular structure of these in-gap states is not known. It was considered that these midgap states could be attributed to oxygen vacancies, as irradiation was previously demonstrated to produce those defects. [7] However, no $Ti^{3+}$ states were observed in the titanium edge measurements. Consequently, we could not conclusively determine the presence of any oxygen vacancies. Furthermore, oxygen vacancies are purported to act as very favorable hydroxylation sites but the roughened sample displayed a low propensity to dissociate water relative to the other samples until very low temperatures were achieved. It seems unlikely that the midgap states produced by roughening are oxygen vacancies.

As alluded to earlier, the ambient pressure measurements at the oxygen edge of the roughened sample appeared to show an overall decrease in water adsorption relative to the other three samples. Of course, a quantitative assessment of this statement is necessary to confirm that a reduction in wetting does occur and, if so, to establish the extent to which it occurs. From a detailed peak fitting analysis on the oxygen edge spectra, estimates of absolute and relative monolayer coverage can be extracted (to compare OH vs. $H_2O$ on the roughened sample and with other samples), potential shifts in peak binding energies can be identified, and the enthalpy and entropy of adsorption on this surface can be calculated. Although the postulated reduction in water adsorption has yet to be confirmed with a quantitative analysis, possible explanations to such a reduction are briefly considered. For example, it may be that the hydroxylation sites in the as-received samples are reduced in number through photoelectrochemical treatment. Alternatively, the adsorption sites may be blocked by carbon contaminants. The amount of carbon-derived contamination appeared to be greater on the roughened surface than on the undoped and two other n-doped $SrTiO_3$ surfaces. Quantification of the contaminant levels may provide insight into the fraction of available adsorption sites on the roughened surface, though we note that this may be less relevant under *in situ* conditions in 0.1 M NaOH solution. On the other hand, the energetics

of the hydroxylation sites may change substantially due to surface rearrangement. Further examination of the roughening process, in terms of both the resultant surface morphology and its electronic structure, is needed to accurately pinpoint the origins of the midgap states and the (as of yet, unconfirmed) reduced water adsorption.

### 5.5.3 Future Work

The ambient pressure x-ray photoelectron data for $SrTiO_3$ have not yet been analyzed quantitatively. Analysis of the titanium 2p and strontium 3d edges will isolate any spectral changes between the four samples that were not immediately apparent. As described above, an enormous amount of information can be extracted from peak fitting analysis of the oxygen edge alone, including estimates of contamination, onset temperatures for wetting behavior, ratios of hydroxylation and hydration surface coverage, or estimates of adsorption site energetics. The quantitative analysis—carbon contaminant extraction, peak fitting—of the complete data set is forthcoming. Confirmation of the qualitative observations made here will require fits to all isobaric data sets for a given sample to ensure reproducibility. Comparisons can then be made across different samples with high confidence.

Future experiments will include ambient pressure x-ray photoelectron spectroscopy on $SrTiO_3$ samples subjected to surface preparation techniques with known defect states (argon ion bombardment) or well-defined terminations (molecular beam epitaxy, UHV cleavage) for comparison with the experiments conducted here. For example, argon ion bombardment procedures are typical in surface cleaning prior to x-ray photoelectron experiments but have also been found to generate significant concentrations of oxygen vacancies in strontium titanate samples. [9, 10, 28, 29, 56] Such measurements would confirm that surface oxygen vacancies do not contribute to the observed adsorption behavior in the roughened $SrTiO_3$ sample.

## 5.6 Conclusion

This study presents the x-ray photoelectron measurements of four strontium titanate single crystals at the (001) plane under ambient pressure conditions. The effects of surface termination, dopants, and photoelectrochemical treatment on water adsorption behavior are examined at several x-ray edges, including titanium 2p, strontium 3d, and oxygen 1s. No conclusive statements regarding the roles of these variables in $SrTiO_3$ wetting behavior could be made on visual inspection alone due to very small (if any) changes in the Ti 2p and Sr 3d spectra and significant contributions from carbon contaminants in the oxygen 1s spectra. Consequently, quantitative analysis of the x-ray photoelectron data—including removal of contaminants from the spectra and detailed peak fitting—is forthcoming. The foundation for a quantitative comparison of these samples has been laid out—in describing both the information that can be derived from such analysis and expected changes in the data across the four samples.

# References


(1) Chen, Y.; Wang, J.; Xiong, C.; Dou, R.; Yang, J.; Nie, J. Scanning Tunneling Microscopy/Spectroscopy Studies of Resistive Switching in Nb-Doped $SrTiO_3$. *Journal of Applied Physics* **2012**, *112*, 023703.

(2) Di Capua, R.; Radovic, M.; De Luca, G.; Maggio-Aprile, I.; Granozio, F. M.; Plumb, N.; Ristic, Z.; di Uccio, U. S.; Vaglio, R.; Salluzzo, M. Observation of a Two-Dimensional Electron Gas at the Surface of Annealed $SrTiO_3$ Single Crystals by Scanning Tunneling Spectroscopy. *Physical Review B* **2012**, *86*, 155425.

(3) Chambers, S. A.; Droubay, T.; Kaspar, T. C.; Gutowski, M. Experimental Determination of Valence Band Maxima for $SrTiO_3$, $TiO_2$, and SrO and the Associated Valence Band Offsets with Si (001). *Journal of Vacuum Science & Technology B* **2004**, *22*, 2205–2215.

(4) Guisinger, N. P.; Santos, T. S.; Guest, J. R.; Chien, T.-Y.; Bhattacharya, A.; Freeland, J. W.; Bode, M. Nanometer-Scale Striped Surface Terminations on Fractured $SrTiO_3$ Surfaces. *ACS Nano* **2009**, *3*, 4132–4136.

(5) Erdman, N.; Marks, L. $SrTiO_3$ (001) Surface Structures Under Oxidizing Conditions. *Surface Science* **2003**, *526*, 107–114.

(6) Kubo, T.; Nozoye, H. Surface Structure of $SrTiO_3$ (100). *Surface Science* **2003**, *542*, 177–191.

(7) Zhang, S.; Guo, D.; Wang, M.; Javed, M. S.; Hu, C. Magnetism in $SrTiO_3$ Before and After UV Irradiation. *Applied Surface Science* **2015**, *335*, 115–120.

(8) Plaza, M.; Huang, X.; Ko, J.; Brock, J. D.; Shen, M.; Simpson, B. H.; Rodríguez-López, J.; Ritzert, N. L.; Abruña, H. D.; Letchworth-Weaver, K., et al. Structure of the Photo-Catalytically Active Surface of $SrTiO_3$. *arXiv preprint arXiv:1508.01220* **2015**.

(9) Raisch, C.; Chassé, T.; Langheinrich, C.; Chassé, A. Preparation and Investigation of the A-Site and B-Site Terminated $SrTiO_3$ (001) Surface: A Combined Experimental and Theoretical X-Ray Photoelectron Diffraction Study. *Journal of Applied Physics* **2012**, *112*, 073505.

(10) Hikita, T.; Hanada, T.; Kudo, M.; Kawai, M. Surface Structure of $SrTiO_3$ (001) with Various Surface Treatments. *Journal of Vacuum Science & Technology A* **1993**, *11*, 2649–2654.

(11) Baeumer, C.; Xu, C.; Gunkel, F.; Raab, N.; Heinen, R. A.; Koehl, A.; Dittmann, R. Surface Termination Conversion During $SrTiO_3$ Thin Film Growth Revealed by X-Ray Photoelectron Spectroscopy. *Scientific Reports* **2015**, *5*.

(12) Ketteler, G.; Yamamoto, S.; Bluhm, H.; Andersson, K.; Starr, D. E.; Ogletree, D. F.; Ogasawara, H.; Nilsson, A.; Salmeron, M. The Nature of Water Nucleation Sites on $TiO_2$ (110) Surfaces Revealed by Ambient Pressure X-Ray Photoelectron Spectroscopy. *Journal of Physical Chemistry C* **2007**, *111*, 8278–8282.

(13) Yamamoto, S.; Kendelewicz, T.; Newberg, J. T.; Ketteler, G.; Starr, D. E.; Mysak, E. R.; Andersson, K. J.; Ogasawara, H.; Bluhm, H.; Salmeron, M., et al. Water Adsorption on $\alpha$-$Fe_2O_3$ (0001) at near Ambient Conditions. *Journal of Physical Chemistry C* **2010**, *114*, 2256–2266.

(14) Newberg, J. T.; Starr, D. E.; Yamamoto, S.; Kaya, S.; Kendelewicz, T.; Mysak, E. R.; Porsgaard, S.; Salmeron, M. B.; Brown, G. E.; Nilsson, A., et al. Formation of Hydroxyl and Water Layers on MgO Films Studied with Ambient Pressure XPS. *Surface Science* **2011**, *605*, 89–94.

(15) Stoerzinger, K. A.; Hong, W. T.; Crumlin, E. J.; Bluhm, H.; Biegalski, M. D.; Shao-Horn, Y. Water Reactivity on the $LaCoO_3$ (001) Surface: An Ambient Pressure X-ray Photoelectron Spectroscopy Study. *Journal of Physical Chemistry C* **2014**, *118*, 19733–19741.

(16) Siegbahn, H. Electron Spectroscopy for Chemical Analysis of Liquids and Solutions. *Journal of Physical Chemistry* **1985**, *89*, 897–909.

(17) Bluhm, H. Preface to the Special Issue of Topics in Catalysis on Ambient Pressure X-ray Photoelectron Spectroscopy. *Topics in Catalysis* **2015**, 1–2.

(18) Stoerzinger, K. A.; Hong, W. T.; Crumlin, E. J.; Bluhm, H.; Shao-Horn, Y. Insights into Electrochemical Reactions from Ambient Pressure Photoelectron Spectroscopy. *Accounts of Chemical Research* **2015**, *48*, 2976–2983.

(19) Hussain, H.; Torrelles, X.; Rajput, P.; Nicotra, M.; Thornton, G.; Zegenhagen, J. A Quantitative Structural Investigation of the 0.1 wt% Nb-$SrTiO_3$ (001)/$H_2O$ Interface. *Journal of Physical Chemistry C* **2014**, *118*, 10980–10988.

(20) Kawasaki, M.; Takahashi, K.; Maeda, T.; Tsuchiya, R., et al. Atomic Control of the $SrTiO_3$ Crystal Surface. *Science* **1994**, *266*, 1540.

(21) Hatch, R. C.; Fredrickson, K. D.; Choi, M.; Lin, C.; Seo, H.; Posadas, A. B.; Demkov, A. A. Surface Electronic Structure for Various Surface Preparations of Nb-Doped $SrTiO_3$ (001). *Journal of Applied Physics* **2013**, *114*, 103710.

(22) Biswas, A.; Rossen, P.; Yang, C.; Siemons, W.; Jung, M.; Yang, I.; Ramesh, R.; Jeong, Y. Universal Ti-Rich Termination of Atomically Flat $SrTiO_3$ (001),(110), and (111) Surfaces. *Applied Physics Letters* **2011**, *98*, 051904.

(23) Koster, G.; Kropman, B. L.; Rijnders, G. J.; Blank, D. H.; Rogalla, H. Quasi-Ideal Strontium Titanate Crystal Surfaces Through Formation of Strontium Hydroxide. *Applied Physics Letters* **1998**, *73*, 2920–2922.

(24) Lippmaa, M.; Takahashi, K.; Ohashi, S.; Nakagawa, N.; Sato, T.; Iwatsuki, M.; Koinuma, H.; Kawasaki, M. Dynamics of $SrTiO_3$ Surface During Wet Etching and High-Tempera-ture Annealing. *Ferroelectrics* **1999**, *224*, 373–378.

(25) Ohnishi, T.; Shibuya, K.; Lippmaa, M.; Kobayashi, D.; Kumigashira, H.; Oshima, M.; Koinuma, H. Preparation of Thermally Stable $TiO_2$-Terminated $SrTiO_3$(100) Substrate Surfaces. *Applied Physics Letters* **2004**, *85*.

(26) Nishimura, T.; Ikeda, A.; Namba, H.; Morishita, T.; Kido, Y. Structure Change of $TiO_2$-Terminated $SrTiO_3$ (001) Surfaces by Annealing in $O_2$ Atmosphere and Ultra-high Vacuum. *Surface Science* **1999**, *421*, 273–278.

(27) Bhaskar, S.; Allgeyer, D.; Smythe III, J. A. Depth Profiling of Dielectric $SrTiO_3$ Thin Films by Angle-Resolved X-Ray Photoelectron Spectroscopy. *Applied Physics Letters* **2006**, *89*.

(28) Adachi, Y.; Kohiki, S.; Wagatsuma, K.; Oku, M. Intrinsic and Extrinsic Surface States of Single Crystalline $SrTiO_3$. *Journal of Applied Physics* **1998**.

(29) Brookes, N.; Quinn, F.; Thornton, G. The Involvement of Step and Terrace Sites in $H_2O$ Adsorption on $SrTiO_3$ (100). *Physica Scripta* **1987**, *36*, 711.

(30) Marshall, M. S.; Newell, D. T.; Payne, D. J.; Egdell, R. G.; Castell, M. R. Atomic and Electronic Surface Structures of Dopants in Oxides: STM and XPS of Nb-And La-Doped $SrTiO_3$ (001). *Physical Review B* **2011**, *83*, 035410.

(31) Dupin, J.-C.; Gonbeau, D.; Vinatier, P.; Levasseur, A. Systematic XPS Studies of Metal Oxides, Hydroxides and Peroxides. *Physical Chemistry Chemical Physics* **2000**, *2*, 1319–1324.

(32) Miyauchi, M.; Nakajima, A.; Watanabe, T.; Hashimoto, K. Photocatalysis and Photoinduced Hydrophilicity of Various Metal Oxide Thin Films. *Chemistry of Materials* **2002**, *14*, 2812–2816.

(33) Crumlin, E. J.; Mutoro, E.; Hong, W. T.; Biegalski, M. D.; Christen, H. M.; Liu, Z.; Bluhm, H.; Shao-Horn, Y. In Situ Ambient Pressure X-Ray Photoelectron Spectroscopy of Cobalt Perovskite Surfaces Under Cathodic Polarization at High Temperatures. *Journal of Physical Chemistry C* **2013**, *117*, 16087–16094.

(34) Thompson, A.; Vaughan, D.; Center for X-ray Optics; Advanced Light Source, *X-Ray Data Booklet*; Lawrence Berkeley National Laboratory: 2009.

(35) Van Benthem, K.; Elsässer, C.; French, R. Bulk Electronic Structure of $SrTiO_3$: Experiment and Theory. *Journal of Applied Physics* **2001**, *90*, 6156–6164.

(36) Guo, X.; Chen, X.; Lu, W. Optical Properties of Nb-Doped $SrTiO_3$ from First Principles Study. *Solid State Communications* **2003**, *126*, 441–446.

(37) Takizawa, M.; Maekawa, K.; Wadati, H.; Yoshida, T.; Fujimori, A.; Kumigashira, H.; Oshima, M. Angle-Resolved Photoemission Study of Nb-Doped $SrTiO_3$. *Physical Review B* **Mar. 2009**, *79*, 113103.

(38) Ricci, D.; Bano, G.; Pacchioni, G.; Illas, F. Electronic Structure of a Neutral Oxygen Vacancy in $SrTiO_3$. *Physical Review B* **2003**, *68*, 224105.

(39) Bäurer, M.; Zagonel, L.; Barrett, N.; Hoffmann, M. In *Journal of Physics: Conference Series*, 2008; Vol. 94, p 012015.

(40) Rodenbücher, C.; Wicklein, S.; Waser, R.; Szot, K. Insulator-to-Metal Transition of $SrTiO_3$:Nb Single Crystal Surfaces Induced by $Ar^+$ Bombardment. *Applied Physics Letters* **2013**, *102*, 101603.

(41) Wang, Z.; Hao, X.; Gerhold, S.; Novotny, Z.; Franchini, C.; McDermott, E.; Schulte, K.; Schmid, M.; Diebold, U. Water Adsorption at the Tetrahedral Titania Surface Layer of $SrTiO_3$ (110)-(4×1). *Journal of Physical Chemistry C* **2013**, *117*, 26060–26069.

(42) Iwahori, K.; Watanabe, S.; Kawai, M.; Kobayashi, K.; Yamada, H.; Matsushige, K. Effect of Water Adsorption on Microscopic Friction Force on $SrTiO_3$ (001). *Journal of Applied Physics* **2003**, *93*, 3223–3227.

(43) Kato, H. S.; Shiraki, S.; Nantoh, M.; Kawai, M. Water Reaction on $SrTiO_3$ (001): Promotion Effect Due to Condensation. *Surface Science* **2003**, *544*, L722–L728.

(44) Wang, L.-Q.; Baer, D. R.; Engelhard, M. H.; Shultz, A. N. The Adsorption of Liquid and Vapor Water on $TiO_2$ (110) Surfaces: The Role of Defects. *Surface Science* **1995**, *344*, 237–250.

(45) Sham, T.; Lazarus, M. X-Ray Photoelectron Spectroscopy (XPS) Studies of Clean and Hydrated $TiO_2$ (Rutile) Surfaces. *Chemical Physics Letters* **1979**, *68*, 426–432.

(46) Jribi, R.; Barthel, E.; Bluhm, H.; Grunze, M.; Koelsch, P.; Verreault, D.; Søndergård, E. Ultraviolet Irradiation Suppresses Adhesion on $TiO_2$. *Journal of Physical Chemistry C* **2009**, *113*, 8273–8277.

(47) Stoch, J.; Gablankowska-Kukucz, J. The Effect of Carbonate Contaminations on the XPS O 1s Band Structure in Metal Oxides. *Surface and Interface Analysis* **1991**, *17*, 165–167.

(48) Smith, G., *Surface Analysis by Electron Spectroscopy: Measurement and Interpretation*; Updates in Applied Physics and Electrical Technology; Springer US: 2013.

(49) Odelius, M. Mixed Molecular and Dissociative Water Adsorption on MgO [100]. *Physical Review Letters* **1999**, *82*, 3919.

(50) Vlček, L.; Cummings, P. T. Adsorption of Water on $TiO_2$ and $SnO_2$ Surfaces: Molecular Dynamics Study. *Collection of Czechoslovak Chemical Communications* **2008**, *73*, 575–589.

(51) Beck, T.; Klust, A.; Batzill, M.; Diebold, U.; Di Valentin, C.; Tilocca, A.; Selloni, A. Mixed Dissociated/Molecular Monolayer of Water on the $TiO_2$ (011)-(2×1) Surface. *Surface Science* **2005**, *591*, L267–L272.

(52) Raymand, D.; van Duin, A. C.; Spångberg, D.; Goddard, W. A.; Hermansson, K. Water Adsorption on Stepped ZnO Surfaces from MD Simulation. *Surface Science* **2010**, *604*, 741–752.

(53) Bachelet, R.; Sánchez, F.; Santiso, J.; Munuera, C.; Ocal, C.; Fontcuberta, J. Self-Assembly of $SrTiO_3$ (001) Chemical-Terminations: A Route for Oxide-Nanostructure Fabrication by Selective Growth. *Chemistry of Materials* **2009**, *21*, 2494–2498.

(54) Polli, A. D.; Wagner, T.; Gemming, T.; Rühle, M. Growth of Platinum on $TiO_2$- and SrO-Terminated $SrTiO_3$ (100). *Surface Science* **2000**, *448*, 279–289.

(55) Kossoy, A.; Cohen, H.; Bendikov, T.; Wachtel, E.; Lubomirsky, I. Water Adsorption at the Surface of Pure and Gd-Doped Ceria. *Solid State Ionics* **2011**, *194*, 1–4.

(56) Henrich, V. E.; Dresselhaus, G.; Zeiger, H. Surface Defects and the Electronic Structure of $SrTiO_3$ Surfaces. *Physical Review B* **1978**, *17*, 4908.

# Appendix A

# Understanding Multiwavelength Data

*The majority of singular value decomposition data analysis was accomplished in Igor Pro 6.3 with the Visualization and Analysis of Broadband Transient Absorption (v.4.7-1) procedure file scripted by Dr. Matthew Sfeir at Brookhaven National Laboratory for use with the Ultrafast Systems Helios transient absorption system.*

The ability not only to interrogate excited states with broadband pulses but to record the full spectrum instantaneously is advantageous over the traditional monochromatized measurement of light for transient absorption spectroscopy. As previously mentioned, collection of a broadband excited state spectrum can offer a unique handle on the energy landscape of a complex system, but the analysis of the resultant multiwavelength data can be time-consuming and complex. Particularly in the ultraviolet-visible region of the electromagnetic spectrum, an observed transition may encompass the entire bandwidth of the measurement window and/or several transitions may overlap at a given energy/wavelength. Historically, technological limitations of data acquisition required single energy detection as controlled by monochromation. With the use of a white light continuum, the massive quantity of data can result in a daunting, if not overwhelming, analysis for traditional methods applied to single wavelength data. In addition to describing the procedure for the removal of ultrafast artifacts and correction of chirp, this appendix details a comparison of global fit analyses of single wavelengths extracted from the broadband data to global analyses of singular value decomposition reduced data derived from the multiwavelength matrix data. Although the specific set of data considered within this Appendix is taken from that of the oxovanadium complex $VOL^F$ in Chapter 3, the same methodology was applied for correction and analysis of strontium titanate transient data in Chapter 4.

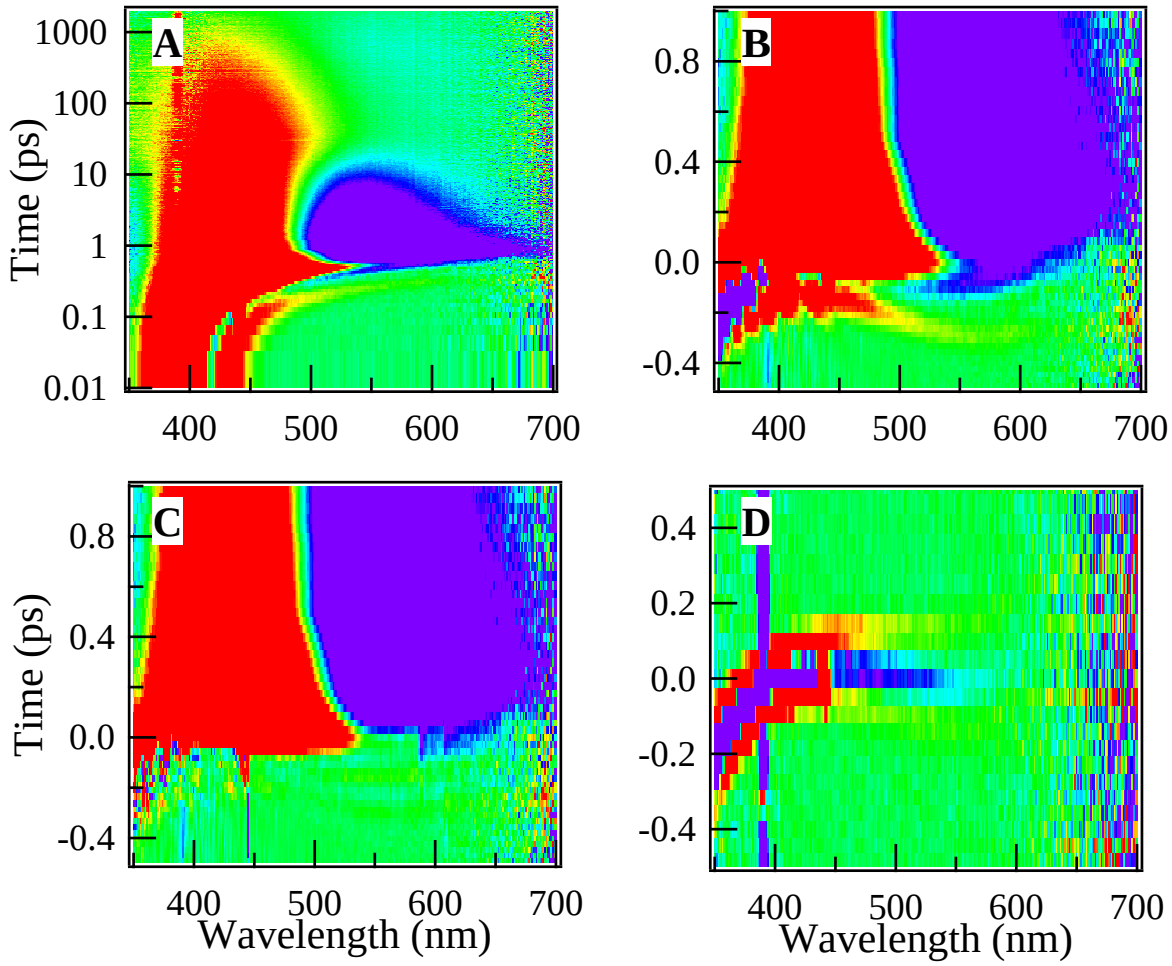


Figure A.1: Example of raw transient absorption matrix data (a), the same data following correction for group velocity dispersion modeled by a quadratic function (b), and removal of the cross-phase modulation signal at early times (c). The chirp-corrected cross-phase modulation signal derived solely from the solvent, here tetrahydrofuran, is shown as well (d).

## A.1 Group Velocity Dispersion Correction and Cross-Phase Modulation Signal Removal

In transition metal complexes, timescales on the order of tens to hundreds of femtoseconds can contain information regarding intramolecular vibrational relaxation (IVR), internal conversion (IC) and intersystem crossing (ISC) following the preparation of the excited system.

It is a critical task then to remove aberrant signals in the response to accurately identify the processes occurring the molecular system. Coherent artifacts in the early femto- to picosecond regime and to adjust the spectra for the dispersion introduced by the sample solvent, cuvette and other transmissive optics are the primary sources of convolution that are discussed here. Prior to analysis, data obtained on this system were corrected for the intrinsic dispersion in the supercontinuum probe following similar approaches used in the literature. [1, 2]

The chirp of the probe was determined with a fitting function of a second-, third-, or fourth-order polynomial. The extracted chirp correction was applied to the time points for each wavelength and the signal intensities at the original time points were extracted by applying a linear interpolation to the dispersion-corrected data (Fig. A.1b). The absolute time axis was also adjusted such that the occurrence of the half maximum of the LMCT bleach response at 425 nm was set to time zero for all wavelengths. (Fig. A.1c). Previous studies have used the nonresonant coherent response (coherent artifact) from the neat solvent and empty cuvette under the same experimental conditions to derive a fit equation to model the dispersion from these two contributions. [3, 4] This approach was complicated by the presence of significant cross-phase modulation component introduced by $VOL^F$ that deviated significantly from that observed in the solvent alone, particularly at excitation wavelengths of 425 nm and 480 nm. In the original published data on $VOL^F$, no subtraction of the cross-phase modulation was applied to the multivariate data prior to analysis by either spectrally resolved global fits or singular value decomposition and global analysis. Subsequent data sets were treated with solvent fits to remove the rapid oscillatory contributions from cross-phase modulation; following correction of the dispersion, early solvent responses were removed through manual fits with first and second derivatives of a Gaussian fit and subtracted from each wavelength trace. In instances where the early solvent response does not vary between the blank solvent and the sample, the fit of the cross-phase modulation can be automated across the entire collected spectrum rather than executed manually. The treatment resulted in a different set of time constants obtained originally, eliminating the need for a slow rise contribution of $\sim$1 ps that was included in the published analysis. The chirp-corrected, cross-phase modulation-removed data were subsequently treated with singular value decomposition (SVD) in order to reduce contributions from noise.

## A.2 Spectrally Resolved Global Fits

For the excited state evolution of $VOL^F$, we assumed a sequential kinetic scheme such that the system could be modeled with a sum of N single exponential functions, convolved with the Gaussian instrument response function (IRF) (Eq. A.1). The IRF is considered approximately equivalent to the cross-correlation function of our pump-probe system, where each pulse has a nominal FWHM length of 100 fs. To determine the time constants for the relaxation of excited state $VOL^F$ in THF, we further divided the transient spectrum in spectral regions corresponding to specific transitions: LMCT bleach recovery or stimulated

emission (GSB/SE) (400-460 nm)(Fig. A.2), excited state absorption (ESA) (540-590 nm) (Fig. A.2), the intermediate overlap region (470-530 nm) (Fig. A.2), as well as the 600-700 nm region (not shown). Our fitting functions were applied to multiple kinetic traces at 10 nm increments in each region, where time constants were fit globally but the amplitudes for each trace were determined locally (individually). The region corresponding to the main ESA (540-590 nm) was fit with a small rise component incorporated into the summation of the single exponential functions, following a previous example by Chergui [5] (Eq. A.2). Although the rise component was incorporated into the initial analysis submitted for publication, its inclusion was deemed unnecessary following the removal of the cross-phase modulation signal from the data.

$$\Delta\text{mOD} = \sum_{i=0}^{n} \text{A}_i e^{-t/\tau_i} \bigotimes \text{IRF} = \sum_{i=0}^{n} \text{A}_i e^{\left(\frac{\sigma^2}{2\tau_i^2} - \frac{t}{\tau_i}\right)} \left[1 + \text{erf}\left(\frac{t}{\sigma\sqrt{2}} - \frac{\sigma}{\tau_i\sqrt{2}}\right)\right] \tag{A.1}$$

$$\Delta\text{mOD} = \left[\text{A}_{rise} e^{-t/\tau_{rise}} + \sum_{i=0}^{n} \text{A}_i \left(e^{-t/\tau_i} - e^{-t/\tau_{rise}}\right)\right] \bigotimes \text{IRF} \tag{A.2}$$

## A.3 Singular Value Decomposition, Global Analysis and Decay-Associated Spectra

#### A.3.0.1 Singular Value Decomposition

Global analysis (GA) of the data was also executed to compare dynamics derived independent of spectral region with the preceding global fits. In order to carry out the global analysis of our system, we first employed Singular Value Decomposition (SVD). SVD is a common transformation of three-dimensional transient absorption data employed to reduce the total number of spectral and kinetic components down to the minimal needed to describe the complete evolution of the system. In practice, singular value decomposition is a factorization of an $m$ x $n$ matrix $M$ into

$$M = USV^T \tag{A.3}$$

where $U$ and $V$ are unitary matrices whose columns comprise two sets of orthogonal basis vectors and $S$ a diagonal matrix containing non-negative singular values, which modulate the relative amplitudes of the corresponding column vectors. For an initial matrix $M$ of raw transient absorption data, $U$ and $V$ represent the orthogonal time and wavelength matrices, containing vectors of so-called eigenspectra and eigenkinetics [6] (see Fig. A.3a and b) whose combined $S$-weighted contributions make up the real data.

Rank analysis of the $S$ matrix was carried out (Fig. A.3c) to assess the appropriate number of kinetic and spectral basis vectors necessary to recreate the original data faithfully

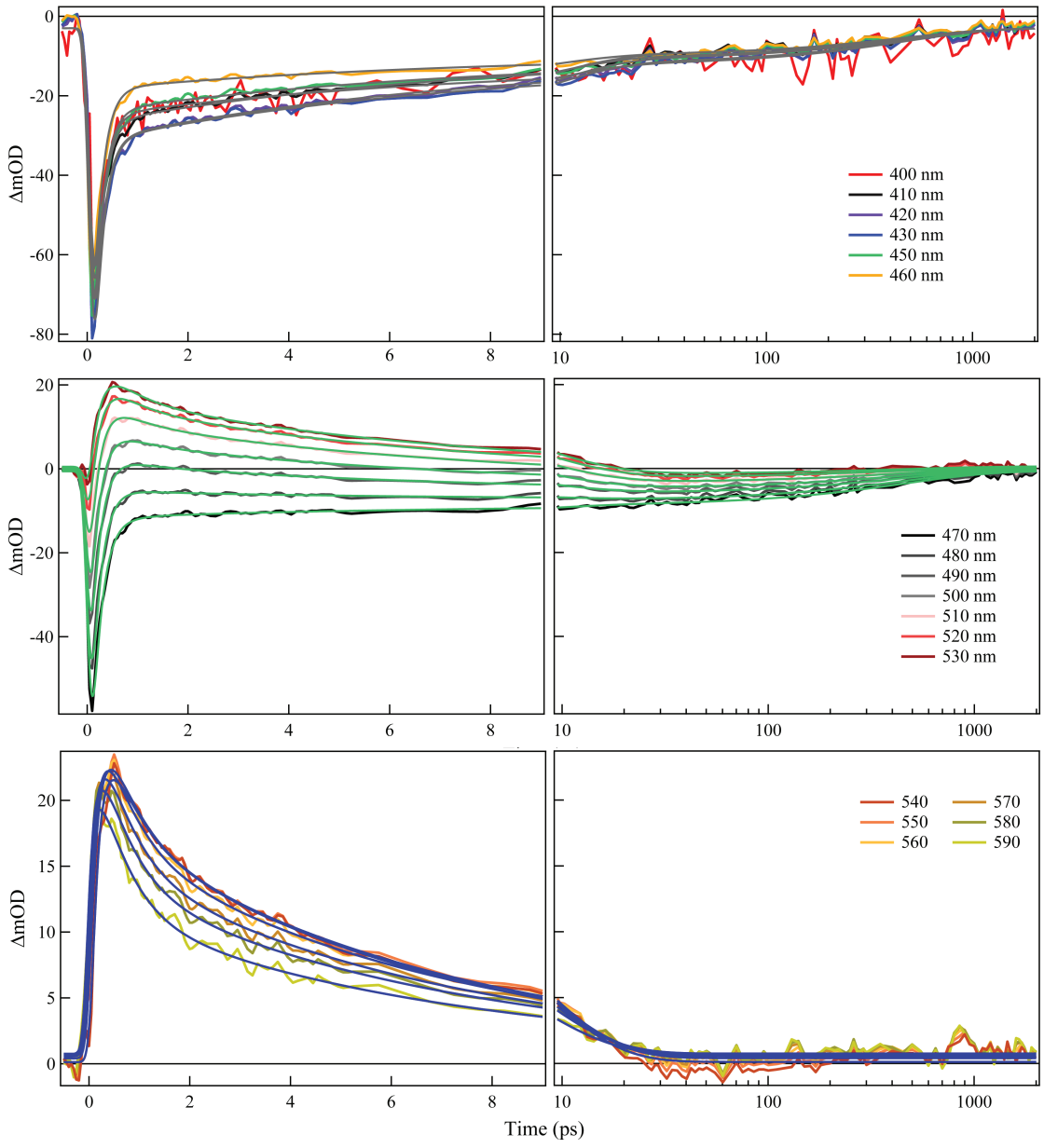


Figure A.2: Illustrated example of the spectrally resolved fits of $VOL^F$ data.

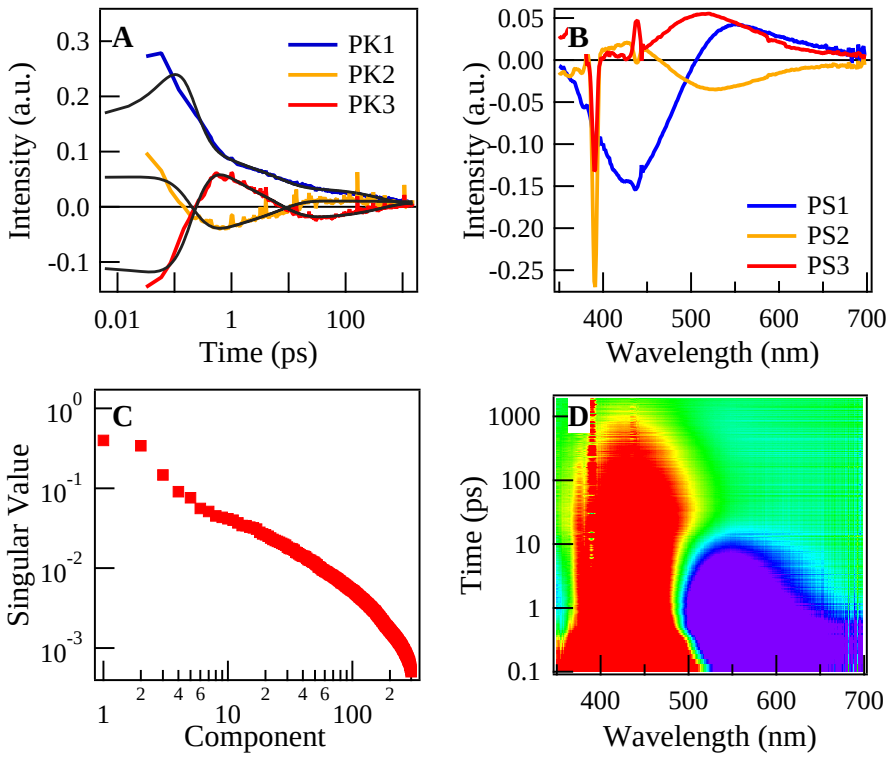


Figure A.3: The singular value decomposition of VOL$^F$ transient data matrix with pump excitation at 390 nm into the corresponding principal eigenkinetics (a), eigenspectra (b), and singular values (c). The first three vectors of the spectral matrix $U$ and kinetic matrix $V$ are included. The global analysis fits to the first three kinetic vectors are shown. All diagonal elements of matrix $S$ are included on a logarithmic scale, to illustrate the prominent weight carried by the first three vectors. The reconstruction of the noise-reduced transient data matrix from the first five components is shown in (d).

while also reducing noise. From the analysis, the first five singular values carried 64 % of the total amplitude in the raw data, with the first two singular values containing 55%; beyond the first vectors, each vector contributes $\leq 1$ % of the total weight. Consequently, the pump-probe spectrum was reconstructed from the first five column vectors of $U$ and $V$. All data and kinetic modeling shown in the main text have been extracted from and carried out on this reconstructed data.

### A.3.0.2 Global Analysis

Following the extraction of eigenkinetics from the raw data, For the analysis, we adhered to the method set forth in the literature. [6–10] For the global analysis, the first three

eigenkinetic traces $V_i^T$ (∼59 % combined amplitude) were utilized. We note the use of the first five significant components of the spectral and kinetic basis vectors to reconstruct the transient data for the spectrally-resolved global fits were applied. Here, the fourth and fifth vector components were discarded as their kinetic vectors showed very little spectral and kinetic structure. Fits of the general summation model using four time constants, $\tau_k$, to the first three kinetic basis vectors reveal similar time constants to those determined by the global fits above (141 fs, 777 fs, 6.82 ps, and 423 ps) (Fig. A.2).

#### A.3.0.3 Decay-Associated Spectra

From our extracted time constants and the associated kinetic amplitudes, decay associated spectra (DAS),contributions representative of the spectrum at the times dictated by the time constants, were reconstructed in Figs. 3.9 and 3.10 by the following equation:

$$DAS_k = \sum_{i=1}^{N} a_{i,k} \cdot s_i \cdot U_i \tag{A.4}$$

For this equation, the first three eigenspectra vectors $U_i$ are weighted by their singular values $s_i$ and the coefficients $a_{i,k}$ for each time constant $\tau_k$, obtained from the general exponential summation model global fits of the corresponding eigenkinetic vectors.

In sequential kinetic schemes without multiple overlapping transitions, the decay-associated spectra can be considered as species-associated spectra (SAS), representing the excited state spectrum of a specific (electronic) state at given points in time. Given the strongly overlapping transitions in the spectra, particularly the two overlapping excited state absorptions, we utilize the normalized DAS (Fig. 3.9 and Fig. 3.10) to aid the assignment of those absorptions in the main text.

# Appendix B

# Further Investigation of the Oxovanadium Motif

To elucidate the interplay of excited state lifetimes and structural distortion in vanadium-based oxidative photocatalysts, multiple molecular analogs of $VOL^F$ were prepared with different electron-withdrawing or -donating groups as well as altered coordination geometry. This appendix details UV-visible and x-ray absorption measurements of these VOL compounds that were carried out to determine whether they might be suitable candidates for further study by transient absorption spectroscopy. Based upon their strong transitions in the visible region of the electromagnetic spectrum and the predicted d-manifold electronic structure (from oxygen K-edge measurements) to support a similarly long-lived excited state, only one compound AJF-3-43 was identified as an appropriate candidate for transient optical spectroscopy. The results of additional transient optical absorption spectroscopic measurements on $VOL^{Me}$ and compound AJF-3-43 are discussed, as well as a failed attempt at transient x-ray absorption on $VOL^F$ to confirm the lifetime of the charge transfer state.

## B.1 UV-Visible Absorption and Chemical Structure

Figure B.1 displays the chemical structures of two oxovanadium chelate complexes, $VOL^F$ and $VOL^{Me}$. The corresponding UV-visible absorption spectra are nearly identical—with the absorption profile of $VOL^F$ reproduced in Fig. B.3a; the spectrum of $VOL^{Me}$ is not shown. Prior to conducting transient optical and static x-ray absorption measurements, it was unclear as to whether the electronegativity of the fluorine substituents relative to the neutral methyl substituents would result in different ground state and/or excited state electronic structures. A slight redshift is observed in the UV-visible absorption spectrum of $VOL^{Me}$ relative to $VOL^F$. However, this spectral shift is not indicative of electronic structure changes arising from the substituents alone; notably, identical syntheses of $VOL^F$ at differing times were observed to generate as much as a 10 nm shift in the peak absorption of the LMCT transition. The comparison of the electronic structure of $VOL^F$ and $VOL^{Me}$ is

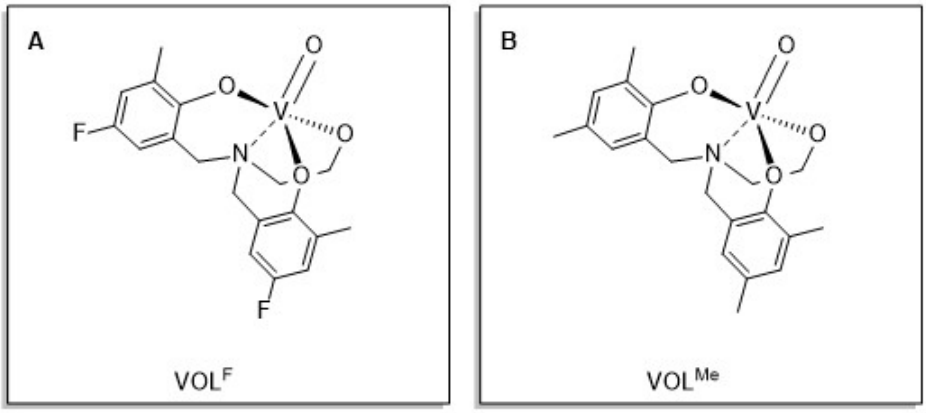


Figure B.1: Chemical structures of $VOL^F$ and $VOL^{Me}$.

continued below.

Employing the same motif of a chelated vanadyl complex, compounds AJF-3-43, AJF-3-112, AJF-4-35, and AJF-4-36, the structures of which are shown in Fig. B.2a, b, c, and d, were synthesized. Each analog was included in our list of candidates for further analysis with a particular aspect in mind. Compound AJF-3-43 was a notable addition to our list of candidates for its hexacoordinate ligand environment, made possible by the addition of an isopropyl group. Insofar as our initial analysis of $VOL^F$ approximated its geometry as nearly tetrahedral, AJF-3-43 was expected to serve as a close proxy for an octahedral oxovanadium complex. AJF-3-112, a *tert*-butylated VOL compound, was primarily altered with the inclusion of a boron triphenyl adduct. The adduct serves as a Lewis-acid, electron-withdrawing group, coordinated to the already strongly electron-deficient apical oxo group. AJF-4-35, an aryl $C_3$ symmetric vanadyl complex, posed an interesting contrast in structural rigidity to $VOL^F$ and the distortion-based argument for its observed lifetime. Conversely, AJF-4-36, a triethanolamine $C_{3v}$ oxovanadium, substituted the steric bulk of phenyl groups in the chelating ligand with a significantly more compact, flexible coordination sphere. Despite the similar coordination motif, however, the analogs show an unusual display of varied UV-visible absorption spectra, as seen in Fig. B.3b.

## B.2 Oxovanadium X-ray Absorption Vanadium L- and Oxygen K-Edges

In Fig. B.4, the partial fluorescence yield (PFY) x-ray absorption spectrum is shown for $VOL^F$ and $VOL^{Me}$. The two spectra show similar features in both the vanadium and oxygen edges, indicating that the substitution of the strongly electronegative fluorine atoms with relatively neutral methyl groups does not contribute substantially to the ground state elec-

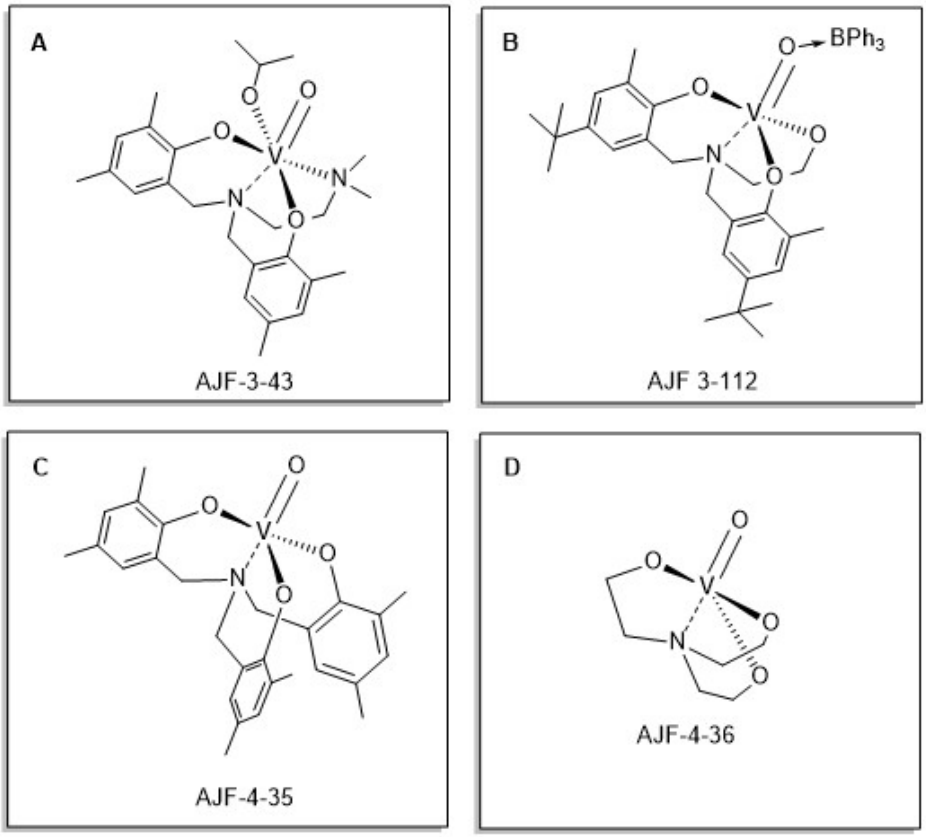


Figure B.2: Chemical structures, formulae and molecular weights VOL analogs (a) AJF-3-43, (b) AJF-3-112, (c) AJF-4-35, and (d) AJF-4-36 in powder form.

tronic structure of the molecule. The comparable x-ray absorption profiles between $VOL^{F}$ and $VOL^{Me}$ is in agreement with the identical behavior observed in transient absorption measurements of $VOL^{Me}$.

Interestingly, AJF-3-43 shows doublet structure in the $L_3$ edge that is observed in vanadium (V) complexes but is less common than the triplet structure observed in AJF-4-35 and AJF-4-36. AJF-3-112, with the Lewis acid boron adduct, has a significantly reduced signal at the vanadium L edges, that are on par with the reduced signal seen in solution phase $VOL^{F}$. It is unclear whether the adduct complex displays the triplet or doublet structure but its oxidation state is fairly certain to be 5+. The overall intensity decrease in the UV-visible and x-ray absorption spectra of AJF-3-112 may indicate a decrease in oxygen-vanadium hybridization.

The oxygen pre-edges of these compounds are particularly interesting for the diversity of profiles among the different complexes as well as the variation between the fluorescence and electron yields for the same compound. Electron yield is, as previously mentioned, much

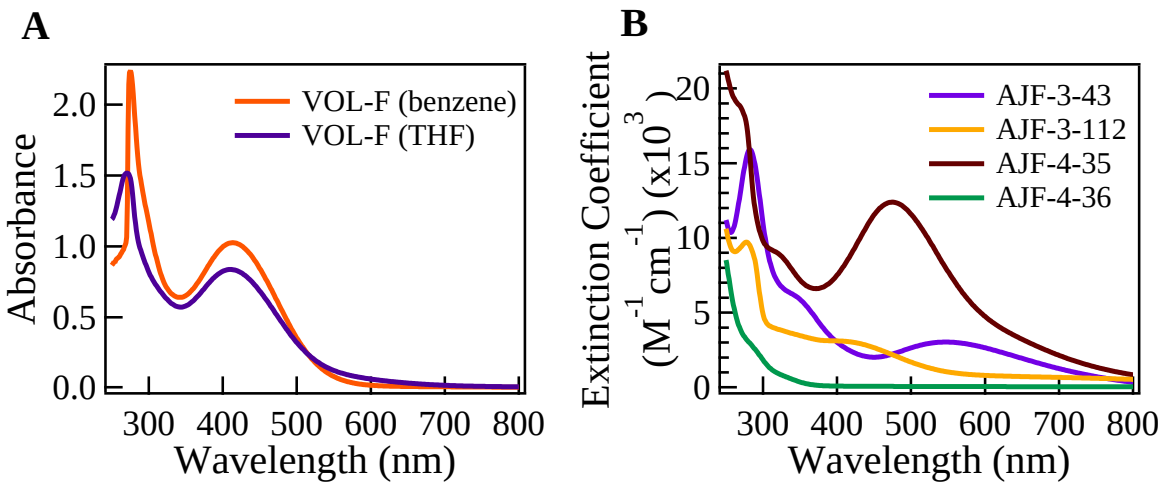


Figure B.3: UV-visible absorption spectra of (a) $VOL^{F}$ in tetrahydrofuran and benzene, and (b) UV-vis spectra of VOL analogs AJF-3-43, AJF-3-112, AJF-4-35, and AJF-4-36 in dry tetrahydrofuran solution.

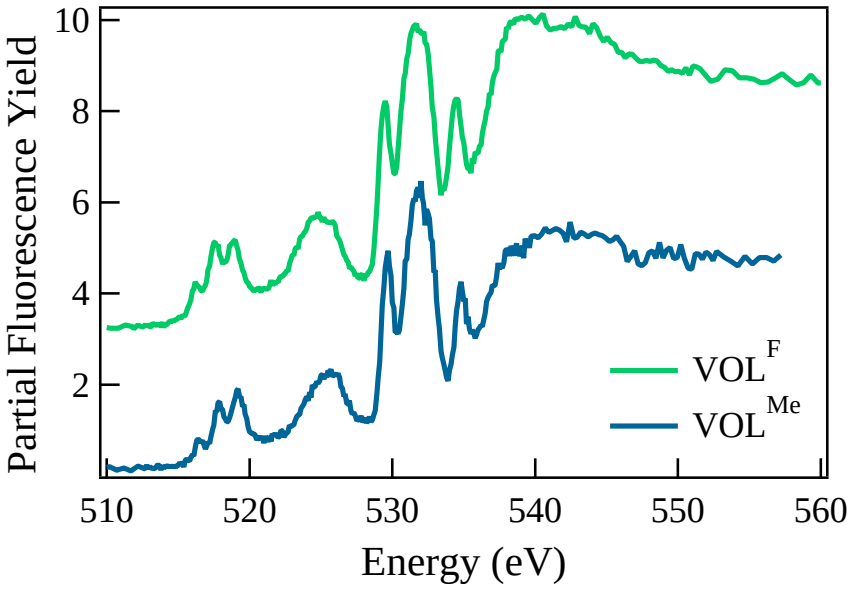


Figure B.4: X-ray absorption spectra of $VOL^{F/Me}$.

more surface sensitive than fluorescence yield due to the relative escape depths of secondary electrons versus photons. No visible damage or darkening of the powder samples was observed

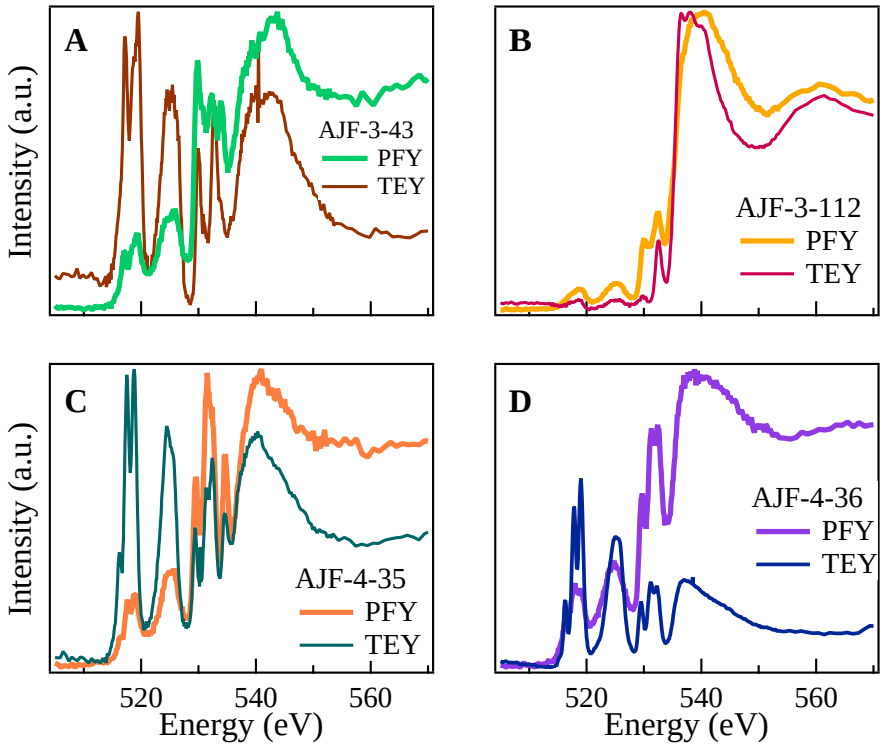


Figure B.5: X-ray absorption spectra at the vanadium $L_{3,2}$- and oxygen K-edges of (a) AJF-3-43, (b) AJF-3-112, (c) AJF-4-35, and (d) AJF-4-36 in powder form. The signal was detected in both partial fluorescence and total electron yields.

following the x-ray absorption measurements, which is suggestive of non-artifact or damage-induced differences between the oxygen edges. In the case of $VOL^F$, some reductive damage was observed in successive scans of the powder samples but only in the vanadium $L_3$ edge and only as a conversion from $V^{5+}$ to $V^{4+}$. This was not observed in the scans of analogous compounds collected at either partial fluorescence or total electron yield.

As previously mentioned, the oxygen pre-edge region has been correlated to observed ligand field splittings in transition metal complexes. Estimates of d-d transition energies can be determined, then, from peak-to-peak energy differences. Variation between the two detection methods are likely due to preference of relaxation channels or exposure to x-rays. Given that the powder samples $d^0$ are assumed to be non-conductive, therefore, the primary contribution to the TEY signal arises from the sample directly in contact with the metal conductive puck rather than the front of the sample which is directly exposed to the full x-ray beam. The only noticeable difference is in AJF-3-43 where the pre-edge shows two peaks in TEY but three peaks in PFY.

## B.3 Transient Optical Absorption Spectra

$VOL^{Me}$ in THF (1.25 mM) showed negligible difference in relaxation as compared to $VOL^{F}$. This is not entirely unexpected as theory calculations of hole and electron localization in the excited state of $VOL^{F}$ show minimal charge density near the fluorine atoms despite their electronegativity. (see Fig. 3.5)

Attempts were made to conduct time-resolved measurements on AJF-3-43, the octahedral complex for comparison of the effects of ligand geometry on relaxation. Unfortunately, at the high concentrations necessary to extract a signal (millimolar), the integrity of the sample was compromised as indicated by UV-visible spectrometry. Dimerization is a likely reaction pathway at these concentrations given the lability of the isopropoxide group. Solution-phase reactivity of oxovanadium (V) complexes is known in the literature. [11]

However, following the alleged dimerization of the sample, excitation of the principal visible transition led to an extremely long lived excited state species, with a lifetime extending well beyond the scope of our measurement (two nanoseconds). The visible transition of the monomer was identified as a ligand-to-metal charge transfer transition by theory (personal communication), though its agreement with experimental spectra was not as good as in $VOL^{F}$. In the dimerized sample, the nature of the visible transition is no longer known. Metal-to-metal charge transfer is a significant possibility and has several precedents for intravalence charge transfer, long-lifetimes, and catalysis. As the oxidation state(s) and structure of the dimerized sample are currently unknown, the transient has not yet been confirmed as an MMCT transition.

## B.4 Time-Resolved Soft X-Ray Absorption Spectroscopy

In an attempt to confirm the source of the transient absorption signal accompanying the long-lived ground state bleach and to confirm the transfer of an electron to the vanadium metal center, transient x-ray absorption in the oxygen K- and vanadium $L_{3,2}$ regime was attempted. Several calculations were made regarding the expected static edge and transient response, accounting for intrinsic experimental difficulty due to the strong absorption of x-ray intensity by the solvent. The transient response of the sample in solution was expected to show a concomitant decrease and increase in the absorption edges of the vanadium and oxygen edges, respectively, following charge transfer. Unfortunately, however, the low solubility of the compound in non-oxygen atom containing solvents was determined to reach a maximum of 3 mM; a concentration minimum of 50 mM would have been necessary to observe a transient signal approximately $\Delta OD = 0.0005$ at the oxygen edge. Previous examples of transient x-ray absorption of solubilized transition metal complexes in the soft x-ray region have included iron [12] and copper [13] where charged complexes and strongly ionic counterions have allowed researchers to achieve appreciable dissolution for conducting x-ray experiments with reasonable signal-to-noise. No results were obtained due to the low solubility of $VOL^{F}$.

# Appendical References


(1) Kovalenko, S. A.; Dobryakov, A. L.; Ruthmann, J.; Ernsting, N. P. Femtosecond Spectroscopy of Condensed Phases with Chirped Supercontinuum Probing. *Physical Review A* **1999**, *59*, 2369–2384.

(2) O'Connor, T.; Panov, M. S.; Mereshchenko, A.; Tarnovsky, A. N.; Lorek, R.; Perera, D.; Diederich, G.; Lambright, S.; Moroz, P.; Zamkov, M. The Effect of the Charge-Separating Interface on Exciton Dynamics in Photocatalytic Colloidal Heteronanocrystals. *ACS Nano* **2012**, *6*, 8156–8165.

(3) Ekvall, K.; Van der Meulen, P.; Dhollande, C.; Berg, L.-E.; Pommeret, S.; Naskrecki, R.; Mialocq, J.-C. Cross-Phase Modulation Artifact in Liquid Phase Transient Absorption Spectroscopy. *Journal of Applied Physics* **2000**, *87*, 2340–2352.

(4) Ruckebusch, C.; Sliwa, M.; Pernot, P.; De Juan, A.; Tauler, R. Comprehensive Data Analysis of Femtosecond Transient Absorption Spectra: A Review. *Journal of Photochemistry and Photobiology C: Photochemistry Reviews* **2012**, *13*, 1–27.

(5) Van der Veen, R. M.; Cannizzo, A.; van Mourik, F.; Viček, A.; Chergui, M. Vibrational Relaxation and Intersystem Crossing of Binuclear Metal Complexes in Solution. *Journal of the American Chemical Society* **2011**, *133*, 305–315.

(6) Steinel, T.; Asbury, J. B.; Zheng, J.; Fayer, M. Watching Hydrogen Bonds Break: A Transient Absorption Study of Water. *Journal of Physical Chemistry A* **2004**, *108*, 10957–10964.

(7) Gawelda, W.; Cannizzo, A.; Pham, V.-T.; Van Mourik, F.; Bressler, C.; Chergui, M. Ultrafast Nonadiabatic Dynamics of $[Fe^{II}(bpy)_3]^{2+}$ in Solution. *Journal of the American Chemical Society* **2007**, *129*, 8199–8206.

(8) Van Stokkum, I. H.; Larsen, D. S.; van Grondelle, R. Global and Target Analysis of Time-Resolved Spectra. *Biochimica Biophysica Acta* **2004**, *1657*, 82–104.

(9) Hofrichter, J.; Sommer, J. H.; Henry, E. R.; Eaton, W. A. Nanosecond Absorption Spectroscopy of Hemoglobin: Elementary Processes in Kinetic Cooperativity. *Proceedings of the National Academy of Sciences* **1983**, *80*, 2235–2239.

(10) Ruckebusch, C.; Sliwa, M.; Réhault, J.; Naumov, P.; Huvenne, J.; Buntinx, G. Hybrid Hard- and Soft-Modelling Applied to Analyze Ultrafast Processes by Femtosecond Transient Absorption Spectroscopy: Study of the Photochromism of Salicylidene Anilines. *Analytica Chimica Acta* **2009**, *642*, Papers presented at the 11th International Conference on Chemometrics in Analytical Chemistry {CAC} 2008, 228–234.

(11) Dash, S. P.; Majumder, S.; Banerjee, A.; Carvalho, M. F. N.; Adão, P.; Pessoa, J. C.; Brzezinski, K.; Garribba, E.; Reuter, H.; Dinda, R. Chemistry of Monomeric and Dinuclear Non-Oxido Vanadium (IV) and Oxidovanadium (V) Aroylazine Complexes: Exploring Solution Behavior. *Inorganic Chemistry* **2016**.

(12) Van Kuiken, B. E.; Cho, H.; Hong, K.; Khalil, M.; Schoenlein, R. W.; Kim, T. K.; Huse, N. Time-Resolved X-ray Spectroscopy in the Water Window: Elucidating Transient Valence Charge Distributions in an Aqueous Fe (II) Complex. *Journal of Physical Chemistry Letters* **2016**.

(13) Chen, L. X.; Shaw, G. B.; Novozhilova, I.; Liu, T.; Jennings, G.; Attenkofer, K.; Meyer, G. J.; Coppens, P. MLCT State Structure and Dynamics of a Copper(I) Diimine Complex Characterized by Pump-Probe X-ray and Laser Spectroscopies and DFT Calculations. *Journal of the American Chemical Society* **2003**, *125*, 7022–7034.